UNIVERSITY OF
Southampton
School of Engineering Sciences

Thesis for degree of Master of Philosophy

October 2011

Efficient Prediction Method for Broadband Acoustic Mode Radiation from Engine Bypass Ducts

Aeronautics, Astronautics and Computational Engineering

Jun Wu

UNIVERSITY OF SOUTHAMPTON

ABSTRACT

FALCULTY OF ENGINEERING, SCIENCE & MATHMATICS

Master of Philosophy Thesis

EFFCIENT PREDICTION METHOD FOR BROADBAND ACOUSTIC MODE RADIATION FROM ENGINE BYPASS DUCTS

by Jun Wu

High levels of broadband noise produced by modern high-bypass turbine engines have a significant impact on the environment. High performance computational numerical methods are now taking an active role in this research area. The research presented in this thesis explores a method for efficient prediction of broadband aeroacoustic radiation from a turbofan engine bypass duct and the effect of the multi-mode propagation in the near-field of an engine bypass duct with bifurcations installed on.

An accurate and high-order Computational Aeroacoustics (CAA) numerical scheme is used in two-and-half and three dimensional linearised Euler equations to determine the results. For far-field predictions, the Ffowcs Williams- Hawkings (FW-H) method and the Acoustic Intensity Based Method (AIBM) could be used to solve the single mode problem. However, the current FW-H method can not be used for multi-mode problems due to its required demand for computational resources. AIBM is an efficient tool to predict the pressure in far-field based on the near-field solution calculated by CAA, and has a potential for multi-mode prediction in the far-field.

The performances of the prediction of the radiation of bypass duct acoustics with mean flow have been analysed, with particular attention to the ducts with bifurcations. For the single mode case of the duct acoustics, the AIBM has been implemented and compared against CAA results in the near-field. Comparison between AIBM and FW-H directivity pattern in the far-field region show good agreement. The clean duct cases for multi-mode are solved with the linearised Euler equations (LEE) in two-and-half dimensions and the results are analysed. For multi-frequency cases, the SPL directivity contour almost matches the pattern obtained by summing the results computed by single frequencies. Lower radial modes contribute more to the overall SPL value than higher ones. For the circumferential modes, lower ones are more likely to cut-on to more discrete frequencies. Finally, the three dimensional solver is used to determine the near-field multi-mode radiation from a generic engine bypass with bifurcations. The bifurcations can cause the acoustic pressure waves to be redirected. Interference between the diffracted modes increased the acoustic pressures. Results show that lower radial modes are smaller in amplitude, and are more likely to cut-on when the radial modes are higher. More complex patterns have formed, because of the bifurcation interference, compared to single mode cases. For different circumferential mode cases, the radiation peak angle increases as the circumferential mode increases.

DECLARATION OF AUTHORSSHIP

I, JUN WU, declare that the thesis entitled,

Efficient Prediction Method for Broadband Acoustic Mode Radiation from Engine Bypass Ducts

and the work presented in the thesis are both my own, and have been generated by me as the result of my own original research. I confirm that:

- this work was done wholly or mainly while in candidature for a research degree at this University;
- where any part of this thesis has previously been submitted for a degree or any other qualification at this University or any other institution, this has been clearly stated;
- where I have consulted the published work of others, this is always clearly attributed;
- where I have quoted from the work of others, the source is always given. With the exception of such quotations, this thesis is entirely my own work;
- I have acknowledged all main sources of help;
- where the thesis is based on work done by myself jointly with others, I have made clear exactly what was done by others and what I have contributed myself;
- none of this work has been published before submission, or [delete as appropriate] parts of this work have been published as: [please list references]

Signed:

Date:

Contents

List of Figures

List of Tables

Acknowledgements

I am very grateful to my supervisor, Professor Xin Zhang, for his invaluable guidance, encouragement, support and enthusiasm throughout the duration of my MPhil studies.

I would like to thank Dr. Xiaoxian Chen for his technical advice, helpful discussions, for introducing the fundamental problems in the area of computational aeroacoustics, and supplying the SotonCAA code referenced in this work.

Thanks to my parents, Baoming Wu and Gailan Hou, for their constant support throughout my time at university.

Thanks to my friends, including Antoni Alomar, Ryu Fattah, Edward Benyon, Wen Liu and Xin Wang, for both providing precious suggestions for my research and sharing living experiences in the University of Southampton.

Nomenclature

Alphanumeric Symbols

a_0	Sound speed
c_∞	Free stream sound speed
e_t	Total energy
E, F, G, Q	Inviscid fluxes of Navier-Stokes equations
$\hat{E}, \hat{F}, \hat{G}, \hat{Q}$	Generalized inviscid fluxes
f	Frequency
$H( )$	Heaviside function
$G( )$	Hankel function
I	Identity matrix
J	Coordinates transformation Jacobian
M	Mach number
P	Static pressure
P_{ij}	Compressible stress tensor
$q_c, q_m q_e$	Source Terms in Acoustic Perturbation Equations
Re	Reynolds number
s	Entropy
t	Time
T	Temperature
T_{ij}	Lighthill stress tensor
u_i, u, v, w	Cartesian velocity components $(u_1, u_2, u_3) = (u, v, w)$
x_i, x, y, z	Cartesian velocity components $(x_1, x_2, x_3) = (x, y, z)$
$\mathbf{x}$	Observer position Vector
$\mathbf{y}$	Source position vector

Greek Symbols

γ	Ratio of specific heat coefficients
$\delta( )$	Dirac delta function
μ	Molecular viscosity
ρ	Fluid density
τ_{ij}	Viscous stress tensor
$\sigma_{i,j}$	Reynolds stress tensor
τ	Pseudo-time

ξ, η, ζ	Generalized coordinates
v	Kinematic viscosity
$\tilde{v}$	Working variable for turbulent viscosity
ω	Angular frequency

Subscripts

$( )_\infty$	Freestream value
$( )^a$	Acoustic perturbation
$( )_V$	Viscous value
$( )_t$	Turbulent value
$( )'$	Perturbation value
$\bar{( )}$	Time-averaged value

Abbreviations

2D	Two-dimensional
3D	Three-dimensional
AIBM	Acoustic intensity based method
APE	Acoustic perturbation equations
BEM	Boundary element method
CAA	Computational aeroacoustics
CFD	Computational fluid dynamics
CFL	Courant-Friedrichs-Levy
DES	Detached eddy simulation
DNS	Direct numerical simulation
DRP	Dispersion-relation-preserving
FFT	Fast Fourier transform
FW-H	Ffowcs Williams and Hawkings
KH	Kevin-Helmholtz
LDDRK	Low-dissipation and low-dispersion Runge-Kutta
LEE	Linearized Euler equations
LES	Large eddy simulation
NS	Navier-Stokes
RANS	Reynolds-averaged Navier-Stokes
RK	Runge-Kutta
S-A	Spalart-Allmaras
SGS	Sub-grid scale
SPL	Sound pressure level, with a reference pressure of 20 μPa

1 Introduction

Increase in air traffic around expanding urban areas over recent years has led to strict noise-emission constraints being imposed on civil aircrafts. Pressure from public and political groups to maintain or reduce current noise levels conflicts, with the ever-growing demand for more air transport, has given rise to a more stringent certification criteria. The target set by the Advisory Council for Aeroacoustics Research in Europe (ACARE) [1] aims for a 10 dB reduction in perceived aircraft noise between 2000 and 2020. Furthermore, extreme acoustic environments can lead to significant design alterations, to cope with large acoustic loads. This usually results in additional weight, and increases cost. These factors have thus prompted numerous studies into methods for accurate measurement and numerical simulations for reduction of aircraft generated noise.

In the early 1960s when turbojet engines were introduced, the main contributor to aircraft noise was jet noise. Since then, advances in low noise high-bypass ratio turbofans have greatly reduced engine noise.

Both theoretical and experimental studies have been conducted in order to understand and predict the noise generation and radiation, to identify noise reduction and control techniques. However, the cost of the experiments in the wind tunnel is high and the variable conditions required are limited. Therefore, numerical methods are becoming more appealing since the computing technology is developing quickly.

A number of numerical investigations into broadband noise propagation have been conducted, as described in later chapters. The main aim of this work is to study the development of computational method for accurate and efficient prediction of acoustic broadband noise as well as individual modal propagation of engine bypass duct geometries. This is to be achieved using high-order Computational Aeroacoustics (CAA) numerical schemes. The Acoustic Intensity Based Method (AIBM) [2-4] is also studied for the far-field acoustic prediction. Computational issues will be discussed during the development of the method. The newly developed CAA methods are capable of single and multi-frequency model simulations for an axisymmetric geometry with an axisymmetric mean flow.

The structure of the thesis is as follows.

In Chapter 2, literatures are reviewed and summarised. Fundamental acoustic analogy developments are discussed, followed by a brief introduction to computational fluid dynamic (CFD) models, which are aimed at computing the mean flow field. Then the progress in CAA is outlined, including the governing equations to solve the turbofan noise propagation and radiation in both near-field and far-field. A set of efficient 2.5D linear Euler equations is introduced to predict the 3D duct mode propagation in the 2D plane for symmetrical mean flow while a set of 3D linearised Euler equations in a cylindrical coordinate system is used for the asymmetric mean flow. The solvers are validated using a linear CAA scattering test case.

In Chapter 3, a numerical method named Acoustic Intensity Based Method (AIBM) is studied for the reconstruction and prediction of radiated fields. This study uses test case specific to duct propagation problems for far-field propagation in multi-mode problems. The prediction method requires the near-field results of a CAA simulation.

Chapter 4 presents results of a 3D model of the sound propagation and radiation from a bypass duct with bifurcations, as well as the linear 2.5D model in axisymmetric clean duct cases in a range of modes.

In Chapter 5, the main conclusions are summarised and suggestions for future work are proposed.

2 Literature Review

2.1 Acoustic Analogy

2.1.1 Sound Fields Radiated by Simple Sources

Aeroacoustics is concerned with sound generation and propagation of sound waves in flow. Aerodynamic sound is the sound generated by unsteady flow motions (and its interaction with solid bodies), rather than vibrating or pulsating objects. Aerodynamic sound fields can be classified into three types depending on how the kinetic energy of the flow is converted to acoustic energy.

A monopole field, also called a point source, is formed by forcing the mass in a fixed region of space to fluctuate. The acoustic waves generated by a monopole propagated equally in all directions. The directivity pattern for a monopole source is circular, as shown in Fig. 2.1(a).

A dipole field is generated by forcing the momentum in a fixed region of space to fluctuate, and it consists of two monopole sources of equal strength but opposite in phase. A dipole source does not radiate sound equally in all directions due to some sound cancellation. The directivity pattern is shown in Fig. 2.1(b).

A quadrupole field is formed by forcing the rate of momentum flux in a fixed region of space to fluctuate. Two types of quadrupole fields can be formed: lateral and longitudinal quadrupole. The former consists of two opposite dipoles as shown in Fig. 2.1(c), and the latter consists of two opposite phase dipoles aligned along a line, as shown in Fig. 2.1(d). The lateral quadruple is associated with the shear stress and is common within all turbulent flows. A lateral quadrupole radiates well only in front of each monopole source, as the sound is cancelled at points equidistant from adjacent opposite monopoles.

The radiation pattern from a longitudinal quadrupole is similar to that from a lateral quadrupole in the near-field. In the far-field, the sound radiation directivity from a longitudinal source is focused towards the line along which the dipoles lie.

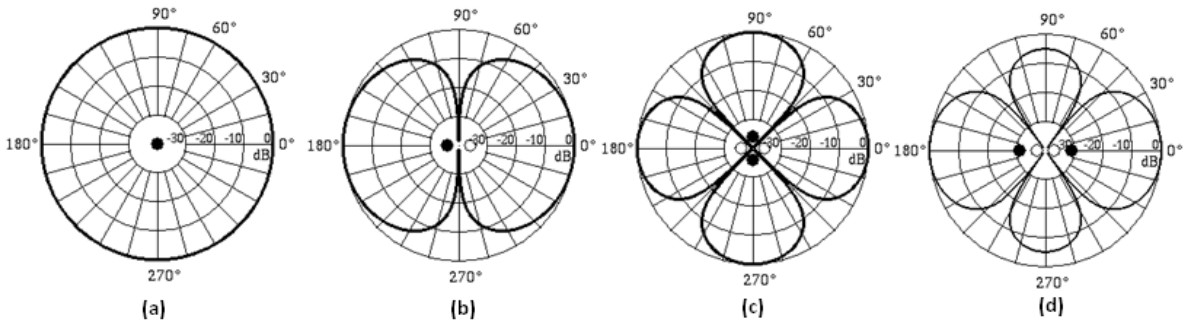

Figure 2.1: Directivity patterns for acoustic sources; (a) monopole, (b) dipole, (c) lateral quadrupole, (d) longitudinal quadrupole [2]

2.1.2 Acoustic Analogy

The main theories of acoustic analogy were first developed in the 1950s. In the early years of the jet engine development, excessive noise from the high-speed exhausts of turbojet engines was a cause of considerable concern. This stimulated a great deal of effort to mathematically represent the process of noise generation and propagation. Although there were a number of attempts to describe this phenomenon, the representation was pioneered by James Lighthill [7] in the early 1950s, who accounted for the influence of turbulence as a source of sound. Later Curle extended Lighthill's theory by considering the influence of solid boundaries [8]. Further, to include the effect of solid bodies in arbitrary motion, Ffowcs Williams and Hawkings developed a form of the Lighthill acoustic analogy to include moving surfaces [9]. In 1975, Farassat revised and analysed the theory of noise generation from moving bodies with an application to helicopter rotors [10].

2.1.2.1 Lighthill's Acoustic Analogy

In the 1950s, Lighthill transformed the Navier-Stokes and continuity equations to form an exact, inhomogeneous wave equation in which the source terms are important only within the region of turbulence. He argued that the acoustic perturbations were a extremely small component of the whole turbulent motion and therefore its feedback on the main flow could be ignored. The properties of the unsteady flow in the source region may then be determined by neglecting the production and propagation of the sound, which is a reasonable approximation if the Mach number is small. This approximation is valid for many important types of flows and this theory leads to unambiguous predictions of the sound.

The propagation of sound in a uniform medium is governed by the mass conservation and Navier-Stokes momentum equations

$$\frac{\partial \rho}{\partial t} + \frac{\partial}{\partial x_i}(\rho u_i) = 0, \tag{2.1}$$

$$\frac{\partial \rho u_i}{\partial t} + \frac{\partial}{\partial x_j}\left(\rho u_i u_j + P_{ij}\right) = 0 \tag{2.2}$$

where ρ is density, u_i and u_j are the velocity components, P_{ij} is the stress tensor, representing the force in the x_i direction acting on a portion of fluid per unit surface area with inward normal in the x_j direction.

Eliminating the term ρu_i from Eqs (2.1) and (2.2), Lighthill's equation can be easily shown by rearranging the sound propagation equation as follows,

$$\frac{\partial^2 \rho}{\partial t^2} - a_o^2 \nabla^2 \rho = \frac{\partial^2 T_{ij}}{\partial x_i \partial x_j} \tag{2.3}$$

where,

$$T_{ij} = \rho u_i u_j + P_{ij} - a_o^2 \rho \delta_{ij} \tag{2.4}$$

$$P_{ij} = p\delta_{ij} - \mu\left(\frac{\partial u_j}{\partial x_i} + \frac{\partial u_i}{\partial x_j} - \frac{2}{3}\frac{\partial u_k}{\partial x_k}\delta_{ij}\right). \tag{2.5}$$

and T_{ij} is known as the Lighthill tensor. It represents the difference between the effective stresses in the real flow and the stresses in the uniform acoustics medium at rest, which is comparative to external fluctuating forces acting on a uniform medium.

It is assumed that for an airflow embedded in a uniform atmosphere at rest, the stress system could be neglected outside of the flow itself. Also, P_{ij} and the conduction of heat are both very small, and viscous stresses in T_{ij} can also be ignored. Hence,

$$T_{ij} \approx \rho u_i u_j. \tag{2.6}$$

If T_{ij} is known exactly, then the density perturbation $\rho' = \rho - \rho_0$ (ambient density) can be obtained, using Green's Functions [7]:

$$\rho' = \frac{1}{4\pi a_0^2} \frac{\partial^2}{\partial x_i \partial x_j} \int T_{ij} \left(\boldsymbol{y}, t - \frac{|\boldsymbol{x} - \boldsymbol{y}|}{a_0} \right) \frac{d\boldsymbol{y}}{|\boldsymbol{x} - \boldsymbol{y}|} . \tag{2.7}$$

The differentiation may be applied as:

$$\rho' \sim \frac{1}{4\pi a_0^2} \int \frac{(x_i - y_i)(x_j - y_j)}{|\boldsymbol{x} - \boldsymbol{y}|^3} \frac{1}{a_0^2} \frac{\partial^2}{\partial t^2} T_{ij} \left(\boldsymbol{y}, t - \frac{|\boldsymbol{x} - \boldsymbol{y}|}{a_0} \right) \frac{d\boldsymbol{y}}{|\boldsymbol{x} - \boldsymbol{y}|} . \tag{2.8}$$

In the far-field, one may approximate $x_i - y_i$ by x_i, which gives the simpler form:

$$\rho' \sim \frac{1}{4\pi a_0^2} \frac{x_i x_j}{|\boldsymbol{x}|^3} \int \frac{1}{a_0^2} \frac{\partial^2}{\partial t^2} T_{ij} \left(\boldsymbol{y}, t - \frac{|\boldsymbol{x} - \boldsymbol{y}|}{a_0} \right) \frac{d\boldsymbol{y}}{|\boldsymbol{x} - \boldsymbol{y}|}. \tag{2.9}$$

A useful and practical deduction with dimensional analysis can be obtained given the volume integral above. For low Mach numbers, in unbounded flow the stress tensor can be estimated by $\rho u_i u_j$ (Lighthill reasoned that under certain circumstances it would be the dominant factor [7]), which has a scale of ρU^2. Since the Strouhal number fl/U has been found to vary far less with changing conditions (like the Reynolds number), one may take frequency as proportional to U/l. Now, it can be determined that the density variation is dimensionally proportional to the product as:

$$\rho - \rho_0 \sim \frac{1}{a_0^4} \frac{1}{x} (\frac{U}{l})^2 \rho U^2 l^3 = \rho \left(\frac{U}{a_0} \right)^4 \frac{l}{x} . \tag{2.10}$$

The radiated sound power is given by $P \sim \rho_0 U^3 l^2 M^5$, which is an extremely small proportion of the flow power.

2.1.2.2 Curle's Extension

One of the restrictions of Lighthill's theory is that the estimated sound wave is only for an unbounded medium. Thus it neglects the effects of reflection, diffraction, absorption and scattering by solid boundaries.

In 1955 Curle [8] extended Lighthill's theory to take into account the presence of solid boundaries. From classical acoustics the sound generated by a volume of quadrupole sources from Lighthill's theory will be reflected and diffracted by solid boundaries. Under certain conditions the solid boundaries will give rise to distributions of dipole or even monopole noise sources, which arise from

the forces and motions imparted to the surface by the unsteady flow. Incorporating these effects into the theory results in the following equation for the density fluctuations,

$$\rho' = \frac{1}{4\pi a_0^2}\int_V \frac{\partial^2 T_{ij}}{\partial x_i \partial x_j}\frac{d\boldsymbol{y}}{|\boldsymbol{x}-\boldsymbol{y}|} + \frac{1}{4\pi}\int_S \left(\frac{1}{r}\frac{\partial \rho}{\partial n} + \frac{1}{r^2}\frac{\partial r}{\partial n}\rho + \frac{1}{a_0 r}\frac{\partial r}{\partial n}\frac{\partial \rho}{\partial t}\right) dS(\boldsymbol{y}) \tag{2.11}$$

$$\rho' = \frac{1}{4\pi a_0{}^2}\left[\frac{\partial^2}{\partial x_i \partial x_j}\int_V \frac{T_{ij}\left(\boldsymbol{y}, t - \frac{|\boldsymbol{x}-\boldsymbol{y}|}{a_0}\right)}{|\boldsymbol{x}-\boldsymbol{y}|} d\boldsymbol{y} + \frac{\partial}{\partial x_i}\int_S l_i \frac{1}{|\boldsymbol{x}-\boldsymbol{y}|}\frac{\partial}{\partial y_i}\left(\rho u_i u_j + P_{ij}\right) dS(\boldsymbol{y})\right.$$

$$\left. + \frac{\partial}{\partial x_i}\int_S l_j \frac{1}{|\boldsymbol{x}-\boldsymbol{y}|}\left(\rho u_i u_j + P_{ij}\right) dS(\boldsymbol{y})\right] \tag{2.12}$$

where l_i is the i th component of the outward-pointing vector, normal to the fluid. The first surface integral in Eq. (2.12) describes the distribution of dipoles on the surface, and the second surface integral describes the distribution of monopoles on the surface, due to the mass addition at the boundary.

There is zero normal velocity at the solid boundaries; that is, if each surface is fixed or is vibrating in its own plane then:

$$l_i u_i \equiv 0.$$

Hence, Eq. (2.12) reduces simply to:

$$\rho' = \frac{1}{4\pi a_0^2}\left[\frac{\partial^2}{\partial x_i \partial x_j}\int_V \frac{T_{ij}\left(\boldsymbol{y}, t - \frac{|\boldsymbol{x}-\boldsymbol{y}|}{a_0}\right)}{|\boldsymbol{x}-\boldsymbol{y}|} d\boldsymbol{y} + \frac{\partial}{\partial x_i}\int_S l_i \frac{1}{|\boldsymbol{x}-\boldsymbol{y}|}\frac{\partial}{\partial y_i}\left(\rho u_i u_j + P_{ij}\right) dS(\boldsymbol{y})\right]. \tag{2.13}$$

Therefore the sound field generated in a hypothetical, unbounded and uniform medium at rest will consist of a distribution of quadruples $\partial^2 T_{ij}(y,\tau)/\partial x_i \partial x_j$ (τ is the retarded time $\tau = t - |\boldsymbol{x}-\boldsymbol{y}|/a_0$). The region external to the solid bodies will consist of a surface distribution of dipoles $P_{ij}(y,\tau)/\partial x_i$. In much the similar way as suggested by Lighthill, the dipole sources can be also simplified as:

$$\rho'(x,t)_{dipole} = \frac{1}{4\pi a_0^2}\frac{x_i}{a_0|\boldsymbol{x}|}\frac{\partial}{\partial t}\int_S l_i P_{ij}(\boldsymbol{y}, t) dS(\boldsymbol{y}). \tag{2.14}$$

Thus a dimensional analysis yields:

$$\rho'(x,t)_{dipole} \sim \frac{1}{a_0^3}\frac{U}{l}\rho U^2 l^2. \tag{2.15}$$

Comparing dipole and quadruple source dimensionally, it can be shown that:

$$\frac{\rho'(x,t)_{quadrupole}}{\rho'(x,t)_{dipole}} = \frac{U}{a_0} = M. \tag{2.16}$$

Therefore, it follows that at sufficiently low Mach numbers, the contribution from dipole sources should be greater than that from quadrupoles.

2.1.2.3 Ffowcs Williams-Hawkings Equation

In 1969 Ffowcs Williams and Hawkings [9] extended the Lighthill-Curle theory to include the effect of arbitrary motion of the source. They replaced the physical surfaces presented in the Lighthill-Curle theory by mathematical surfaces which correspond identically to the motion of the real fluid on and outside the surfaces, but can be specified arbitrarily inside the surfaces. The interior motion does not match the external flow at the boundaries. As a result, mass and momentum sources have to be added to the flow to maintain these discontinuities. These sources act as sound sources, and are analogous to the sound generated by the real flow.

Let the surface of the moving body be given by the function $f(\boldsymbol{y}, \boldsymbol{c}) = 0$, which is defined to be positive outside and negative inside the body. The frame of reference $\boldsymbol{y}$ is fixed with respect to the undisturbed medium.

The continuity equation valid in the entire unbounded space is:

$$\frac{\partial}{\partial t}[\,\rho' H(f)] + \frac{\partial}{\partial x_i}[\rho u_i H(f)]$$

$$= H(f)\left[\frac{\partial \rho'}{\partial t} + \frac{\partial}{\partial x_i}(\rho u_i)\right] + \rho'\left(\frac{\partial H}{\partial t} + u_i \frac{\partial H}{\partial x_i}\right) + \rho_0 u_i \frac{\partial H}{\partial x_i} = \rho'\left(\frac{\partial H}{\partial t} + u_i \frac{\partial H}{\partial x_i}\right) + \rho_0 u_i \frac{\partial H}{\partial x_i}. \quad (2.17)$$

Note that the time derivative of the Heaviside function is given by:

$$\frac{\partial H}{\partial t} + u_i \frac{\partial H}{\partial x_i} = 0. \quad (2.18)$$

So Eq. (2.17) could be written as:

$$\frac{\partial}{\partial t}[\,\rho' H(f)] + \frac{\partial}{\partial x_i}[\rho u_i H(f)] = \rho_0 u_i \frac{\partial H}{\partial x_i} = \rho_0 u_i \delta(f) \frac{\partial f}{\partial x_i} = \rho_0 \mathbf{v}_n |\nabla f| \delta(f). \quad (2.19)$$

Similarly by multiplying the momentum equation and using the same relationship it can be shown that:

$$\frac{\partial}{\partial t}[\,\rho' u_i H(f)] + \frac{\partial}{\partial x_j}\left[(P_{ij} + \rho u_i u_j) H(f)\right] = P_{ij} \frac{\partial H}{\partial x_i} = P_{ij} \frac{\partial f}{\partial x_i} \delta(f). \quad (2.20)$$

Taking the time derivative of both sides of Eq. (2.19) and the space derivative with respect to x_i of both sides of Eq. (2.20), and subtracting the Eq. (2.19) from Eq. (2.20), one can obtain:

$$\frac{\partial^2}{\partial t^2}[\,\rho' H(f)] + \frac{\partial^2}{\partial x_i \partial x_j}\left[(P_{ij} + \rho u_i u_j) H(f)\right] = \frac{\partial}{\partial t}[\rho_0 \mathbf{v}_n |\nabla f| \delta(f)] - \frac{\partial}{\partial x_i}\left[P_{ij} \frac{\partial f}{\partial x_i} \delta(f)\right]. \quad (2.21)$$

Now by adding and subtracting $a_0^2 \frac{\partial^2[\,\rho' H(f)]}{\partial x_i^2}$ on the left side of Eq. (2.21) and rearranging the term involving P_{ij}, Eq. (2.21) becomes:

$$\frac{\partial^2}{\partial t^2}[\,\rho' H(f)] + \frac{\partial^2}{\partial x_i^2}[\,\rho' H(f)]$$

$$= \frac{\partial}{\partial t}[\rho_0 \mathbf{v}_n |\nabla f| \delta(f)] - \frac{\partial}{\partial x_i}\left[P_{ij}\frac{\partial f}{\partial x_i}\delta(f)\right] + \frac{\partial^2}{\partial x_i \partial x_j}\left[(P_{ij} + \rho u_i u_j - a_0^2 \rho \delta_{ij}) H(f)\right]. \quad (2.22)$$

Here a_0 is the speed of sound in the undistributed medium.

Then we obtain the Ffowcs Williams and Hawking equation:

$$\left(\frac{1}{a_0^2}\frac{\partial^2}{\partial t^2} - \nabla^2\right)[\rho' H(f)] = \frac{\partial^2 [T_{ij} H(f)]}{\partial x_i \partial x_j} + \frac{\partial [F_i\, \delta(f)]}{\partial x_i} + \frac{\partial [Q\delta(f)]}{\partial t} \quad (2.23)$$

where $T_{ij} = P_{ij} + \rho u_i u_j - a_0^2 \rho \delta_{ij}$,

$F_i = -[P_{ij} + \rho u_i (u_j - u_j)]\frac{\partial f}{\partial x_j}$,

$Q = [\rho_0 v_i + \rho((u_i - u_j)]\frac{\partial f}{\partial x_i}$.

The first term on the right hand side of Eq. (2.23) represents the quadrupole term. The second and last terms are respectively the dipole term involving unsteady forces and the monopole source. The three source terms on the right hand side of Eq. (2.23) are known as the quadrupole, loading and thickness sources respectively.

2.1.2.4 Farassat Formulation

For several years, the Kirchhoff formulations have been used as an alternative to compute the volume term in FW-H equation in prediction of high-speed rotor noise. Di Francescantonio[6] showed a new boundary integral formulation, which can be extended to a penetrable control surface and the calculation of the surface pressure normal derivative is not required. In 1975, Farassat [7] proposed another form of the solution for the problems that exist in solving the FW-H equation in the case of complex bodies and when the velocity of the body with respect to the undisturbed medium was high, avoiding likely numerical difficulties in the singularities and spatial derivatives.

The Green's function of the wave equation in the unbounded domain is $\delta(g)/4\pi r$, where $g = \tau - t + \frac{r}{a_0}, r = |\boldsymbol{x} - \boldsymbol{y}|$, τ and t are source and observer times respectively. $\boldsymbol{y}$ and $\boldsymbol{x}$ are the observer positions respectively.

For a fixed observer position and time $(\boldsymbol{x}, t)$, $g = 0$ describes a sphere with centre at $\boldsymbol{x}$ and a radius of $a_0(t - \tau)$.

The formal solution of the wave equation

$$\left(\frac{1}{a_0^2}\frac{\partial^2}{\partial t^2} - \nabla^2\right)\Phi = Q(\boldsymbol{x}, t)|\nabla f|\delta(f) \quad (2.24)$$

is

$$4\pi\Phi(\boldsymbol{x}, t) = \int \frac{Q(\boldsymbol{x}, t)}{r}|\nabla f|\delta(f)\delta(g)d\boldsymbol{y}dt. \quad (2.25)$$

For loading noise, we could convert the space derivative into a time derivative for numerical differentiation.

It is shown that the solution of the wave equation

$$\left(\frac{1}{a_0^2}\frac{\partial^2}{\partial t^2} - \nabla^2\right)\Phi = \frac{\partial}{\partial x_i}[Q|\nabla f|\delta(f)] \tag{2.26}$$

is

$$\begin{aligned} 4\pi\Phi(\boldsymbol{x},t) &= \frac{\partial}{\partial x_i}\int \frac{Q_i}{r}|\nabla f|\delta(f)\delta(g)d\boldsymbol{y}dt \\ &= -\frac{1}{a_0}\frac{\partial}{\partial t}\int \frac{Q_i\hat{r_i}}{r}|\nabla f|\delta(f)\delta(g)d\boldsymbol{y}dt - \int \frac{Q_i\hat{r_i}}{r^2}|\nabla f|\delta(f)\delta(g)d\boldsymbol{y}dt \end{aligned} \tag{2.27}$$

where $\hat{r_i} = (x_i - y_i)/r$ is the unit radiation vector.

The integrals in Eq.(2.25) and Eq.(2.27) are all of the form:

$$I = \int \frac{Q}{r}|\nabla f|\delta(f)\delta(g)d\boldsymbol{y}dt. \tag{2.28}$$

Note that the $\boldsymbol{y}$-frame is fixed to the undisturbed medium. Let a blade fixed coordinate system called $\boldsymbol{\eta}$-frame be defined. The $\boldsymbol{y}$ and $\boldsymbol{\eta}$-frame are related by:

$$\boldsymbol{y} = \boldsymbol{y_0}(\tau) + A(\tau)\boldsymbol{\eta}. \tag{2.29}$$

where $\boldsymbol{y_0}(\tau)$ is the position of the origin of the $\boldsymbol{\eta}$-frame and $A(\tau)$ is the matrix of transformation whose coefficients are the function of time τ.

Hence:

$$I = \int \frac{Q}{r}|\nabla f|\delta(f)\delta(g)d\boldsymbol{\eta}d\tau. \tag{2.30}$$

Now changing the variable τ to g, keeping $\boldsymbol{\eta}$ fixed, the Jacobian of the transformation is $1/(1 - M_r)$, where $M_r = v_i\hat{\boldsymbol{r}}_{\boldsymbol{\iota}}/c$ is the Mach number in the radiation direction of the volume element located in the $\boldsymbol{\eta}$-frame. Since $g = \tau - t + |\boldsymbol{x} - \boldsymbol{y}(\boldsymbol{\eta},\tau)|/a_0$, hence:

$$\frac{\partial g}{\partial \tau} = 1 + \frac{1}{a_0}\frac{\partial r}{\partial y_i}\frac{\partial y_i}{\partial \tau} = 1 - \frac{v_i\hat{\boldsymbol{r}}_{\boldsymbol{\iota}}}{a_0} = 1 - M_r \tag{2.31}$$

$$I = \int [\frac{Q}{r(1 - M_r)}]_{ret}|\nabla f|\delta(f)d\boldsymbol{\eta} \tag{2.32}$$

where the subscript *ret* stands for retarded time and $d\boldsymbol{\eta} = dfdS/|\nabla f|$ where dS is the element of surface area of $f = const$,

$$I = \int_{f=0}\left[\frac{Q}{r(1 - M_r)}\right]_{ret} dS\,. \tag{2.33}$$

From the FW-H equation and above, the noise due to thickness and loading terms can be written as:

$$4\pi p'(\boldsymbol{x},t)=\frac{1}{a_0}\frac{\partial}{\partial t}\int_{f=0}\left[\frac{\rho_0 a_0 v_n+l_r}{r(1-M_r)}\right]_{ret}dS+\int_{f=0}\left[\frac{l_r}{r^2(1-M_r)}\right]_{ret}dS \tag{2.34}$$

where $l_r=l_i\hat{r}$ is the force on the fluid per unit area in the radiation direction.

In conclusion, considering the retarded time $\tau_l=t-|\mathbf{x}-\mathbf{y}(\xi,\tau_l)|$, the full formulation (Eq. 1A in [7]) could be written as in Lagrangian coordinates $\xi(\mathbf{y},\tau)$

$$\begin{aligned}4\pi p'(\boldsymbol{x},t)=&\frac{\partial^2}{\partial x_i\partial x_j}\iiint_V\left[\frac{T_{ij}}{r|1-M_r|}\right]_{\tau_l}dV_\xi+\iint_S\left[\frac{\dot{U}_n+U_{\dot{n}}}{r(1-M_r)^2}\right]_{\tau_l}dS(\xi)\\&+\frac{1}{a_0}\iint_S\left[\frac{\dot{L}_r}{r(1-M_r)^2}\right]_{\tau_l}dS(\xi)+\frac{1}{a_0}\iint_S\left[\frac{L_r-L_M}{r^2(1-M_r)^2}\right]_{\tau_l}dS(\xi)\\&+\frac{1}{a_0}\iint_S\left[\frac{L_r(r\dot{M}_r+c_0M_r-c_0M^2)}{r^2(1-M_r)^2}\right]_{\tau_l}dS(\xi)\\&+\frac{1}{a_0}\iint_S\left[\frac{U_n\left(r\dot{M}_r+c_0M_r-c_0M^2\right)}{r^2(1-M_r)^2}\right]_{\tau_l}dS(\xi)\end{aligned} \tag{2.35}$$

where the dot above the letters indicates differentiation with respect to τ.

The FW-H equation solver can solve far-field problems in both single and multiple frequencies. However due to the large memory requirement in multi-frequency cases, the current FW-H solver can only be applied to cases with frequency numbers less than three.

2.2 Computational Fluid Dynamics Models

Generally, all the aeroacoustic phenomena can be expressed by the equations of mass, momentum and energy combined with the initial states, which are the basic compressible Navier-Stokes equations. However it is not possible to simply use Computational Fluid Dynmaics (CFD) codes and solve the compressible Navier-Stokes equations from the location of sound generation up to the observer because the characters, natures, and objectives of aeroacoustic problems are distinctly different from those commonly encountered in CFD [11].

The numerical modelling of aeroacoustic phenomena is demanding several specific reasons. Foremost is the fact that aeroacoustic problems are time dependent by definition. They must be treated time-accurately with appropriate consideration of all relevant time scales. Since the human ear is sensitive to a wide range of frequencies, simulations dealing with such problems must consider resolving a broad range in the frequency spectrum.

The disparity between the energy levels of unsteady flow fluctuations and the acoustic waves is another important consideration. Lighthill [7] showed that the radiated sound power (as shown previously$P\sim\rho_0U^3l^2M^5$) is significantly lower than the mechanical flow power around $10^{-4}\,M^5$. This means that a numerical procedure needed to solve the coupled flow and acoustic field at

$M = 0.1$ requires accuracy of at least 10^{-9}, otherwise all inaccuracies will be observed as numerical noise. This large disparity presents a severe challenge to direct numerical simulations.

For the problems at low Mach number, the disparity in magnitude between the length scales associated with the acoustic and hydrodynamic fields also demands careful consideration. The problem must be solved in both the source region and the far-field in a numerical simulation.

The radiation of energy to the far-field is a defining feature of many aeroacoustic problems. Flow disturbances generally decay fast away from the source of generation. On the other hand, the acoustic waves decay very slowly and reach the boundaries of a finite computation domain. The numerical modelling of such phenomena requires the introduction of artificial boundaries to avoid the reflections of outgoing sound waves back into the computation domain which could otherwise contaminate the solution.

There are two well known approaches used to model acoustic problems. These are the direct approach and the hybrid approach [11]. The direct approach for aerodynamically generated noise solves the flow and acoustic field problem simultaneously. However direct computation of the noise radiated by subsonic three-dimensional flow is difficult because of the large computing resources that are required. The hybrid approach is widely used to simplify the complexity of aeroacoustic problems. In this approach, the flow field is artificially divided into a near-field and far-field.

For the near-field source computation, various numerical methods for solving the unsteady flow field can be used, such as direct numerical method (DNS), large eddy simulation (LES), detached-eddy simulation (DES) and unsteady Reynolds-Averaged Navier-Stokes (RANS).

Acoustic sources obtained are then put into the second solver which solves the propagation and radiation problems in near- or far-field, based on one of the following methods: FW-H equations, Kirchhoff method, linear Euler equations (LEE) or acoustic perturbation equations (APE) [12]. A summary of the different models follows.

2.2.1 Direct Numerical Simulation

In the direct numerical simulation (DNS) method the full compressible Navier-Stokes equations describing the flow field are solved directly without coupling with any other models. This method requires a very high numerical resolution due to the wide range of length and time scales presented between the acoustic variables and the flow variables. Therefore, it is computationally expensive and currently unsuitable for engineering applications and complicated geometries [13].

2.2.2 Large Eddy Simulation

Large-eddy simulation (LES) is another method capable of modelling small unsteady flow characteristics, and is based on Kolmogorov's theory of self similarity. In that theory, large eddies of the flow are dependent on the flow geometry, while smaller eddies have a universal behaviour. For this reason, it becomes practical to solve only for the large eddies explicitly, and model the effect of the smaller and more universal eddies on the larger ones using a sub-grid-scale (SGS) model [14]. It is a cheaper method compared with DNS but is more expensive compared to a solution method based on the Reynolds-averaged Navier-Stokes equations (RANS).

In practice high Reynolds numbers cases with thin boundary layers require too much computational resources. Therefore RANS or other empirical models are implemented in the near wall region to reduce the large computational costs when LES is used throughout the domain [15].

It should be noted that LES is more precise than the unsteady RANS (URANS) if the flow involves separations or acoustic prediction is required [16].

2.2.3 Detached Eddy Simulation

Detached eddy simulation (DES) is a modification of a RANS model in which the model switches to a sub-grid scale formulation in regions fine enough for LES calculations [17]. In the vicinity of solid boundaries, where the turbulent length scale is less than the maximum grid spacing, the RANS mode of solution is assigned. DES is a combination of RANS and LES, and attempts to treat near-wall regions in a RANS-like manner, and treat the rest of the flow in an LES-like manner. The cost of calculation is determined by how much the LES model is involved. DES is a feasible computationally feasible approach for the unsteady flows around complex geometries at high Reynolds numbers. Hedges et al. [17] compared DES and URANS and suggested that with the Spalart-Allmaras (S-A) turbulence model [18], the DES performed consistently better than the URANS calculation in the time-averaged sense.

2.2.4 RANS and URANS

The Reynolds-averaged Navier-Stokes (RANS) equations are emsemble-averaged equations of motion for fluid flow. These equations can be used with approximations, based on knowledge of the properties of turbulence, to obtain approximate averaged solutions to the Navier-Stokes equations. In an unsteady RANS (URANS) approach, flow variables are only averaged over small time scales while they are still time dependent over large time intervals. In other words, the time derivative term would be kept in the RANS equation in mathematics.

2.3 Computational Aeroacoustics Progress

Computational aeroacoustics(CAA) is a new branch of CFD that has made significant progress and the concept of CAA has significantly broadened over the past decades. CAA is concerned with the accurate numerical prediction of aerodynamically generated noise as well as its propagation and far-field characteristics. With the fast growth in computer resources and development of optimized computational schemes, CAA has played important roles in predicting, modelling and reducing airframe noise and its role will be more prominent in the future.

2.3.1 Finite Difference Schemes for CAA

As a development of the CFD method, the CAA technique is becoming more mature. CAA is related to CFD in the sense that it is used to analyse the noise generated by fluid flow and concerned with the simulation of unsteady flow physics. However CAA is different from CFD in the aspect that it involves using high-order schemes to discretize the spatial and temporal derivatives so as to preserve the physics of wave propagation.

CAA techniques are used to solve problems with less computational cost when wave propagates to far-field. For example, using traditional CFD methods [19], it requires at least 20 point-per-wavelength (PPW) to reduce the dispersion and dissipation for sound wave propagation problems.

The computational cost is mainly due to a large number of cells required for the whole computational domain. CAA resolves the waves accurately with fewer PPW using high-order numerical schemes, which use wave space optimization.

There are two main types of high-order approximation finite-difference schemes: explicit schemes and implicit / compact schemes. Explicit schemes directly compute the numeric derivative by employing a large number of computational stencil points for accuracy [20], while compact schemes use smaller stencils by solving a matrix for the numerical derivatives along a grid line, where the numerical derivative at each point depends on the value of the derivative at neighbouring points. The advantage of compact schemes is their higher accuracy compared with explicit schemes, based on limited grid points, while the disadvantages are: firstly, a matrix must be inverted to obtain the spatial derivative at a point and secondly, the boundary stencil has a large effect on the stability and accuracy of the scheme.

The propagation of the wave characters including acoustic, entropy and vortical modes and their speeds are involved in the governing equations in the so-called dispersion relations. Tam and Webb [21] recognized that if a particular numerical scheme has the same dispersion relations as the original governing equations, then it will preserve the wave propagation characteristics, and is suitable for resolving the acoustic waves. Such a scheme is called Dispersion-Relation-Preserving (DRP). One of the explicit schemes employs a seven-point central-difference stencil:

$$\left(\frac{\partial f}{\partial x}\right)_l \approx \frac{1}{\Delta x}\sum_{j=1}^{3} a_j\left(f_{l+j} - f_{l-j}\right), \tag{2.36}$$

in which two of the coefficients a_j are chosen so that Eq. (2.36) is accurate to the fourth order while the remaining coefficient is used as an optimization parameter to minimize the integrated error. This results in an approximation with better resolution of high wave number or short waves as compared to the formally high order but unoptimized scheme.

Lele [22] developed the optimized "spectral-like" compact scheme which provides an improved representation of a range of scales in the evaluation of the first, second and higher order derivatives compared with other schemes. Using Fourier analysis he was able to derive compact finite difference schemes with good resolution characteristics. The resolution characteristics were to be further improved using a special optimisation procedure. One of the schemes is a pentadiagonal scheme with a seven-point stencil given by

$$\beta D_{l-2} + \eta D_{l-1} + D_l + \eta D_{l+1} + \beta D_{l+2} \approx c\frac{f_{l+3} - f_{l-3}}{6\Delta x} + b\frac{f_{l+2} - f_{l-2}}{4\Delta x} + a\frac{f_{l+1} - f_{l-1}}{2\Delta x} \tag{2.37}$$

where D_l denotes the spatial derivative $\left(\frac{\partial f}{\partial x}\right)_l$ at the mesh node l.

Hixon [22, 23] developed a new class of compact schemes that use three-point stencils and can be extended up to eight-order accuracy. In Hixon's approach, the derivative operator is split into forward and backward operators. Only three points are needed to obtain the biased derivatives and only two independent bidiagonal matrices are needed to be reversed instead of solving a tridiagonal linear system of equations. In Hixon's approach the derivative operator D_l was split into forward,

${D_l}^F$, and backward, ${D_l}^B$,operators as $D_l = ({D_l}^F + {D_l}^B)/2$, and the discretized equations were written in the compact form:

$$aD_{l+1}^F + (1-a-c)D_l^F + cD_{l-1}^F \approx (bf_{l+1} - (2b-1)f_l - (1-b)f_{l-1})/\Delta x$$

$$cD_{l+1}^B + (1-a-c)D_l^B + aD_{l-1}^B \approx \big((1-b)f_{l+1} - (2b-1)f_l - bf_{l-1}\big)/\Delta x. \qquad (2.38)$$

For Hixon's six order scheme, the coefficients are $a = \frac{1}{2} - \frac{1}{2\sqrt{5}}, b = \frac{1}{6a} + a, c = 0$. The stencil is reduced to three points and the tridiagonal matrix is replaced by two bidiagonal matrices.

Ashcroft and Zhang [25] optimized the compact schemes using a Taylor series expansion, which improved the resolution characteristics of Hixon's scheme. The new schemes require very small stencils, fewer boundary stencils and offer more accuracy for high resolution numerical calculations in aeroacoustics. The general stencils for the forward and backward derivative operators are defined as:

$$\alpha_F D_{i+1}^F + \beta_F D_i^F = \frac{1}{\Delta x}[a_F f_{i+2} + b_F f_{i+1} + c_F f_i + d_F f_{i-1} + e_F f_{i-2}]$$

$$\beta_B D_i^B + \gamma_B D_{i-1}^B = \frac{1}{\Delta x}[a_B f_{i+2} + b_B f_{i+1} + c_B f_i + d_B f_{i-1} + e_B f_{i-2}]\,. \qquad (2.39)$$

Using Fourier analysis, the coefficients of the biased operators are selected such that their dispersion characteristics match those of the original central compact scheme and the numerical wave numbers have equal and opposite imaginary components. The scheme accuracy was good and was independent of direction.

2.3.2 Governing Equations

The Euler Equations can solve all three kinds of waves for fluid flow, namely the vortical, entropy and acoustic waves. Sound propagation is hardly affected by viscosity for typical aeroacoustic flows outside a critical layer which is not considered here, and sound perturbations are usually ignored in the convection velocity because they are too small. These two facts mean that the Euler equations can be put forward to simulate the propagation of sound waves and are described as linearized Euler equations (LEE), which provides accurate numerical solutions by only considering perturbations.

The governing equations based on the inviscid flow equations, for 3D flow in flux vector form can be written as Eq. (2.40) in conservative form:

$$\frac{\partial \rho}{\partial t} + \nabla \cdot (\rho \mathbf{v}) + \alpha \frac{\rho v}{y} = 0$$

$$\frac{\partial (\rho u)}{\partial t} + \nabla \cdot (\rho u \mathbf{v}) + \frac{\partial p}{\partial x} + \alpha \frac{\rho u v}{y} = 0$$

$$\frac{\partial (\rho v)}{\partial t} + \nabla \cdot (\rho v \mathbf{v}) + \frac{\partial p}{\partial y} + \alpha \rho \frac{(v^2 - w^2)}{y} = 0 \qquad (2.40)$$

$$\frac{\partial (\rho w)}{\partial t} + \nabla \cdot (\rho w \mathbf{v}) + \frac{\partial p}{y \partial \theta} + \alpha \frac{2\rho v w}{y} = 0$$

$$\frac{\partial(\rho e)}{\partial t} + \nabla \cdot (\rho e + p)\mathbf{v} + \alpha \frac{(\rho e + p)v}{y} = 0$$

where in the Cartesian system $\alpha = 0$, $\frac{\partial}{y\partial\theta} \rightarrow \frac{\partial}{\partial z}$, and the differential operator is given by:

$$\nabla = \frac{\partial}{\partial x}\mathbf{i} + \frac{\partial}{\partial y}\mathbf{j} + \frac{\partial}{\partial z}\mathbf{k} \tag{2.41}$$

while in cylindrical coordinate system $\alpha = 1$, and the differential operator is:

$$\nabla = \frac{\partial}{\partial x}\mathbf{e_x} + \frac{\partial}{\partial y}\mathbf{e_r} + \frac{\partial}{\partial z}\mathbf{e_\theta} \tag{2.42}$$

For the ideal gas, the equations in Eq. (2.40) can be changed using a relation below:

$$\rho e = \frac{p}{\gamma - 1} + \frac{1}{2}\rho(u^2 + v^2 + w^2). \tag{2.43}$$

Compared with the background mean flow, if the acoustic amplitudes are small enough, the propagation can be modelled by linearising the governing equations about the mean flow. By ignoring second order perturbation terms, the Euler equation can be reduced to LEE equations:

$$\frac{\partial \rho'}{\partial t} + \mathbf{V}_0 \cdot \nabla\rho' + \mathbf{v}' \cdot \nabla\rho_0 + \rho_0 \nabla \cdot \mathbf{v}' + \rho' \nabla \cdot \mathbf{V}_0 + \alpha \frac{\rho' V_0 + \rho_0 v'}{y} = 0$$

$$\frac{\partial u'}{\partial t} + (\mathbf{V_0} \cdot \nabla)u' + (\mathbf{v}' \cdot \nabla)U_\mathbf{0} + \frac{1}{\rho_0}\frac{\partial p'}{\partial x} = 0$$

$$\frac{\partial v'}{\partial t} + (\mathbf{V_0} \cdot \nabla)v' + (\mathbf{v}' \cdot \nabla)V_\mathbf{0} + \frac{1}{\rho_0}\frac{\partial \rho'}{\partial y} - \alpha \frac{2w'W_0}{y} = 0 \tag{2.44}$$

$$\frac{\partial w'}{\partial t} + (\mathbf{V_0} \cdot \nabla)w' + (\mathbf{v}' \cdot \nabla)W_\mathbf{0} + \frac{1}{\rho_0}\frac{\partial p'}{y\partial\theta} + \alpha \frac{w'V_0 + v'W_0}{y} = 0$$

$$\frac{\partial p'}{\partial t} + (\mathbf{V_0} \cdot \nabla)p' + (\mathbf{v}' \cdot \nabla)p_\mathbf{0} + \gamma p_0 \nabla \cdot \mathbf{v}' + \gamma p' \nabla \cdot \mathbf{V_0} + \alpha\gamma \frac{p'V_0 + p_0 v'}{y} = 0.$$

For aero-engine duct applications, we can assume that the acoustic disturbances are restricted to the blade passing frequency and its harmonics, and propagate through an axisymmetric mean flow without swirl. It is possible to write the disturbances at each frequency in term of a Fourier series of circumferential modes:

$$f'(x, y, \theta, t) = f'_m(x, y)e^{i(\omega t - m\theta)} \tag{2.45}$$

where f' can represents any flow variable, m the circumferential mode, θ the circumferential angle and ω the angular frequency. Hence following relationships can be derived:

$$\frac{\partial}{\partial t}\left(\frac{\partial f'}{\partial \theta}\right) = m\omega f'; \qquad \frac{\partial f'}{\partial \theta} = -\frac{m}{\omega}\frac{\partial f'}{\partial t}. \tag{2.46}$$

This leads to the development of a so-called 2.5D form of the LEE which represents the 3D acoustic wave solved by a 2D computational plane for axisymmetric flow [26].

$$\frac{\partial \rho'}{\partial t} + \mathbf{V}_0 \cdot \overline{\nabla}\rho' + \mathbf{v}' \cdot \overline{\nabla}\rho_0 + \rho_0 \overline{\nabla} \cdot \mathbf{v}' + \rho' \overline{\nabla} \cdot \mathbf{V}_0 - \frac{m\rho_0}{\omega y} w'_t + \frac{\rho' V_0 + \rho_0 v'}{y} = 0$$

$$\frac{\partial u'}{\partial t} + (\mathbf{V_0} \cdot \overline{\nabla})u' + (\mathbf{v}' \cdot \overline{\nabla})u_0 + \frac{1}{\rho_0}\frac{\partial p'}{\partial x} = 0$$

$$\frac{\partial v'}{\partial t} + (\mathbf{V_0} \cdot \overline{\nabla})v' + (\mathbf{v}' \cdot \overline{\nabla})v_0 + \frac{1}{\rho_0}\frac{\partial \rho'}{\partial y} = 0 \qquad (2.47)$$

$$\frac{\partial w'_t}{\partial t} + (\mathbf{V_0} \cdot \overline{\nabla})w'_t + \frac{m\omega}{\rho_0 y} p' + V_0 \frac{w'_t}{y} = 0$$

$$\frac{\partial p'}{\partial t} + (\mathbf{V_0} \cdot \overline{\nabla})p' + (\mathbf{v}' \cdot \overline{\nabla})p_0 + \gamma p_0 \overline{\nabla} \cdot \mathbf{v}' + \gamma p' \overline{\nabla} \cdot \mathbf{V_0} - \frac{m\gamma p_0}{\omega y} w'_t + \gamma \frac{p' V_0 + p_0 v'}{y} = 0$$

where w'_t is the time derivative of the circumferential velocity, which is different from w' in Eq.(2.44) for circumferential velocity. $\overline{\nabla}$ is the reduced differential operator:

$$\overline{\nabla} = \frac{\partial}{\partial x}\mathbf{e_x} + \frac{\partial}{\partial y}\mathbf{e_r} \qquad (2.48)$$

Eq. (2.47) is defined only for single frequency and single circumferential modes. For multi-frequency cases a new form of LEE [27] could be derived and written in complex form. The disturbances in terms of Fourier series in the circumferential direction could be written as:

$$f'(x, y, \theta, t) = e^{-im\theta} \sum_{\omega=-\infty}^{\infty} f'_m(x, y) e^{i\omega t} \qquad (2.49)$$

The complex form of the multi-mode LEE could then be written as:

$$\frac{\partial \rho'}{\partial t} + \mathbf{V}_0 \cdot \overline{\nabla}\rho' + \mathbf{v}' \cdot \overline{\nabla}\rho_0 + \rho_0 \overline{\nabla} \cdot \mathbf{v}' + \rho' \overline{\nabla} \cdot \mathbf{V}_0 - \frac{im\rho_0}{y} w' - \frac{im\rho'}{y} w_0 + \frac{\rho' v_0 + \rho_0 v'}{y} = 0$$

$$\frac{\partial u'}{\partial t} + (\mathbf{V_0} \cdot \overline{\nabla})u' + (\mathbf{v}' \cdot \overline{\nabla})u_\mathbf{0} + \frac{1}{\rho_0}\frac{\partial p'}{\partial x} - \frac{imw_0}{y} u' = 0$$

$$\frac{\partial v'}{\partial t} + (\mathbf{V_0} \cdot \overline{\nabla})v' + (\mathbf{v}' \cdot \overline{\nabla})v_\mathbf{0} + \frac{1}{\rho_0}\frac{\partial p'}{\partial y} - \frac{imw_0}{y} v' = 0 \qquad (2.50)$$

$$\frac{\partial w'}{\partial t} + (\mathbf{V_0} \cdot \overline{\nabla})w' + (\mathbf{v}' \cdot \overline{\nabla})w_\mathbf{0} - \frac{imw_0}{y} w' - \frac{im}{y\rho_0} p' = 0$$

$$\frac{\partial p'}{\partial t} + (\mathbf{V_0} \cdot \overline{\nabla})p' + (\mathbf{v}' \cdot \overline{\nabla})p_\mathbf{0} + \gamma p_0 \overline{\nabla} \cdot \mathbf{v}' + \gamma p'^{\overline{\nabla}} \cdot \mathbf{V_0} + \gamma \frac{p' V_0 + p_0 v'}{y} - \frac{im\gamma p_0}{y} w' - \frac{imw_0}{y} p' = 0$$

where $i = \sqrt{-1}$. The above equations can be used in calculating multi-frequency duct acoustic problems because the equations do not contain any frequency content. They could be used in the time domain for multi-mode contributions. In addition, the equations allow a constant swirl background flow ($w_0 \neq 0$). Hence they can be applied to a wider range of flow fields [27].

The acoustic wave can be introduced into the computational domain through a wave admission region. The broadband acoustic modal inputs can be expressed in harmonic forms in an inflow buffer zone as the noise sources. Considering the background temperature as constant in the inflow buffer zone, the non-dimensional acoustic pressure and density inputs are same as $p' = \rho'$. The real part of the general form for an acoustic model for each (m, n) mode is:

$$p' = \rho' = \sum_{k=\mathrm{K_1}}^{\mathrm{K_N}} p'_k = \sum_{k=\mathrm{K_1}}^{\mathrm{K_N}} A[\cos(\tau_{mn})]\,[J_m(k_r y) + c_1 Y_m(k_r y)] Re\{e^{i(\omega t - k_a x - m\theta)}\}$$

$$u' = \sum_{k=\mathrm{K_1}}^{\mathrm{K_N}} \frac{k_a}{(k - k_a u_0)} p'_k$$

$$v' = \sum_{k=\mathrm{K_1}}^{\mathrm{K_N}} \frac{A[\cos(\tau_{mn})]}{(k - k_a u_0)} \frac{d[J_m(k_r y) + c_1 Y_m(k_r y)]}{dy} Re\left\{e^{i\left(\omega t - k_a x - m\theta + \frac{\pi}{2}\right)}\right\} \tag{2.51}$$

$$w'_t = \sum_{k=\mathrm{K_1}}^{\mathrm{K_N}} \frac{m p'_k}{(k - k_a u_0)}$$

where wave numbers $\mathrm{K_1}$ and $\mathrm{K_N}$ refer to the range of frequency. The weighting constants c_1 and τ_{mn} are given by

$$c_1 = \tan(\tau_{mn}) = -\frac{\frac{\partial}{\partial y} J_m(k_r y_{inner})}{\frac{\partial}{\partial y} Y_m(k_r y_{inner})} \tag{2.52}$$

where J_m and Y_m are Bessel functions of the first and second kind in m th order respectively. A, y_{inner}, k_r , k_a, ω are specified as the wave amplitude, the radius at the duct inner surface, radial wave number, axial wave number and non-dimensional frequency respectively.

The n th radial mode wave number k_r is given in following relation, determined by the hard-wall boundary conditions of the duct in the admission zone at nth order:

$$\frac{\partial}{\partial y} J_m(k_r y_{outer}) \frac{\partial}{\partial y} Y_m(k_r y_{inner}) - \frac{\partial}{\partial y} J_m(k_r y_{inner}) \frac{\partial}{\partial y} Y_m(k_r y_{outer}) = 0. \tag{2.53}$$

The axial wave number k_a and mode cut-on ratio ξ are given by:

$$k_a = \frac{k}{\alpha^2}\left(-u_0 + \sqrt{1 - \xi^{-2}}\right); \qquad \xi = \frac{\omega}{k_r \alpha} \tag{2.54}$$

where $\alpha = \sqrt{1-u_0^2}$.

The test and validation using LEE are shown in later chapters.

2.3.3 Overview of SotonCAA

SotonCAA is a proprietary CFD/CAA program, based on FORTRAN 95, which has been developed and used by the University of Southampton in the past few years. Depending on the formulation of the governing equations, such as linearised Navier-Stokes or Euler equations, SotonCAA features different numerical schemes and consists of a number of subroutines which solve different schemes. The advantage of this modular structure is that the new schemes are convenient to implement to the rest of the code, which can evolve over time. The disadvantage is that the code has grown rather complex with interrelated subroutines.

The main parts of SotonCAA are the compact finite-difference scheme (6^{th}-order) of Hixon [23,24] and the 4^{th}-order optimized compact scheme of Ashcraft and Zhang [25]. The time integration uses a low storage, low dispersion and dissipation Runge-Kutta (LDDRK) [28] scheme which is a fourth-order accurate 4-6 stage scheme. Other low-order (2^{nd}-3^{rd}) schemes have also been included to allow rapid problem set up, i.e. running to an approximate solution before starting the main calculation. A high-order implicit scheme, ESDIRK4 (Explicit first stage, singly diagonally implicit Runge-Kutta) [29], is implemented but is not fully tested. As for boundary conditions, a number of non-reflecting methods have been implemented in SotonCAA with LEE and APE solvers to perform acoustic calculations. Buffer zone schemes are implemented and used to perform non-linear flow calculations with accurate results. Other boundary conditions, such as standard, adiabatic solid wall and symmetry boundary conditions, are also implemented.

The FW-H solver is independent of the CFD/CAA flow solvers, so supporting programs called 'CFD to FWH' and 'FW-H' in the SotonCAA package are employed. The 'CFD to FWH' code is a link between two solvers. The raw data outputs from CFD calculation are calculated and their values on a three-dimensional integration surface are treated before being stored for the aeroacoustic solver. The far-field observer positions from of the integration surface are also determined.

Data is read into the main program through 'input file', 'grid file' and 'parameter file'. The 'input file' lists the schemes to be used, the numerical parameters for the simulation, the block information, the boundary conditions, and other necessary parameters. The 'grid file' only contains the grid-point information generated by separate software such as GRIDGEN [30]. The 'parameter file' contains user defined parameters. The code is portable across all platforms with FORTRAN 95 and MPI installed. This includes Windows and UNIX machines. Using unformatted output files could maximise disk storage efficiency. There are utilities for converting from one format to another. This file conversion capability should be included in the general GUI interface on Windows platforms.

2.3.3.1 Spatial Discretization

In order to ease the formal extension to a higher-order accuracy, low operation count and for general flexibility, a finite-difference approach is employed to discretize the governing equation. The flux derivatives in the transformed conservation equations are evaluated with a prefactored 6^{th}-order Hixon's scheme in the research, as is shown by Eqs. (2.38) and (2.39).

2.3.3.2 Time Matching Scheme

In SotonCAA, a low dispersion and dissipation Runge-Kutta (LDDRK) is 4th order accurate in time for linear problems and gives 2nd order temporal accuracy for non-linear problems. A two-storage level marching cycle (4-6 LDDRK) [28] is employed.

Giving the following differential equation:

$$\frac{dU}{dt} + \frac{dF}{dx} = 0 \tag{2.55}$$

Step One (Low Storage)

$$h^{(1)} = -\Delta t \frac{d}{dx}[F(U^n)]$$

$$h^{(2)} = -\Delta t \frac{d}{dx}\left[F\left(U^n + \frac{1}{4}h^{(1)}\right)\right]$$

$$h^{(3)} = -\Delta t \frac{d}{dx}\left(F\left(U^n + \frac{1}{3}h^{(2)}\right)\right)$$

$$h^{(4)} = -\Delta t \frac{d}{dx}\left(F\left(U^n + \frac{1}{2}h^{(3)}\right)\right)$$

$$U^{n+1} = U^n + h^{(4)} \tag{2.56}$$

Step Two (High Storage)

$$h^{(1)} = -\Delta t \frac{d}{dx}(F(U^n))$$

$$h^{(2)} = -\Delta t \frac{d}{dx}\left(F\left(U^n + 0.17667h^{(1)}\right)\right)$$

$$h^{(3)} = -\Delta t \frac{d}{dx}\left(F\left(U^n + 0.38904h^{(2)}\right)\right)$$

$$h^{(4)} = -\Delta t \frac{d}{dx}\left(F\left(U^n + \frac{1}{4}h^{(3)}\right)\right)$$

$$h^{(5)} = -\Delta t \frac{d}{dx}\left(F\left(U^n + \frac{1}{3}h^{(4)}\right)\right)$$

$$h^{(6)} = -\Delta t \frac{d}{dx}\left(F\left(U^n + \frac{1}{2}h^{(5)}\right)\right)$$

$$U^{n+1} = U^n + h^{(6)}\,. \tag{2.57}$$

Using these two numerical schemes long time accurate solutions can be obtained for computational aeroacoustic problems. These are also adequate for general CFD applications.

2.3.3.3 Filtering Scheme

The prefactored compact schemes are centered schemes, and therefore contain no inherent dissipation. Unexpected errors can be generated from mesh non-uniformity, boundary conditions, non-linear flow features, or poorly specified initial conditions. A filtering scheme has been incorporated to overcome these difficulties and assure numerical stability while retaining the accuracy of spatial compact scheme [29].

If a component of the solution vector is denoted by φ, filtered values $\hat{\varphi}$ are obtained by solving the tridiagonal system

$$\alpha_f \hat{\varphi}_{i-1} + \hat{\varphi}_i + \alpha_f \hat{\varphi}_{i+1} = \sum_{n=0}^{N} \frac{a_n}{2} (\varphi_{i+n} + \varphi_{i-n}) \tag{2.58}$$

where the coefficients $\alpha_f, \alpha_0, \alpha_1, \ldots \alpha_N$ determine the order and spectral response of the filter. With a proper choice of these coefficients, Eq. (2.58) provides a $2N^{th}$-order formula on a 2N+1 point stencil.

Table 2.1 gives a group of coefficients of a 6^{th}-order central difference filtering scheme with 7 points stencil, which is used in the work.

Table.2.1: Coefficients of a 6^{th}-order central difference filtering scheme.

α_{-3}	0.015625
α_{-2}	-0.09375
α_{-1}	0.234375
α_0	0.6875
α_1	0.234375
α_2	-0.09375
α_3	0.015625

The 6^{th} order formula requires a seven point stencil; it is therefore not suitable for use at and near boundary points. In these regions, the order of accuracy of the filter is reduced to a biased filtering scheme. Values along the boundary points are left unfiltered. The filter is applied sequentially in each coordinate direction to the conserved variable at every time step.

2.3.3.4 Turbulence Model

In SotonCAA, the Spalart-Allmaras (S-A) turbulence model [18] is implemented by solving a single partial differential transport equation for a working variable related to the turbulence viscosity. The Detached Eddy Simulation (DES) [17] model in SotonCAA solves exactly the same transport equation as the S-A model which includes a modified length scale in the destruction term.

2.3.3.5 Boundary Conditions

The acoustic wave propagation is based on an assumed acoustic source which is introduced into the domain. An inflow boundary condition could be used to introduce a pre-defined acoustic source in the form of a duct mode at a location inside the duct region of the computational domain, while

disturbances can be emitted from the domain through outflow boundary conditions. The requirements for the boundary conditions allow the disturbance of an acoustic wave to pass through and out of the computational domain without reflections.

In SotonCAA code, a number of non-reflecting boundary conditions are employed. The main three methods are presented below: slip-wall boundary, impedance boundary and buffer zone boundary conditions.

Slip-Wall Boundary Condition

The slip-wall condition is used for the flow interaction with a rigid wall by setting the normal velocity component to zero. i.e.:

$$\mathbf{v} \cdot \mathbf{n} = 0. \tag{2.59}$$

For high-order discretisation schemes, it is generally not sufficient to set only the normal velocity at the wall boundary to zero, for the reason that the order of the discretisation scheme is higher than the order of the governing partial differential equations.

Taking the momentum equation in LEE with the unit normal vector $\mathbf{n}$, Eq. (2.60) gives the normal pressure derivative at the wall as zero:

$$\frac{\partial p}{\partial n} = 0\,. \tag{2.60}$$

Time Domain Impedance Wall Boundary Condition

Impedance boundary conditions are used to define wall boundaries that are non-rigid and they are generally associated with acoustic liners. The difference between impedance boundary conditions and slip-wall boundary conditions is that the normal acoustic velocity perturbation is non-zero:

$$\mathbf{v} \cdot \mathbf{n} \neq 0. \tag{2.61}$$

Acoustic liners in aircraft engine ducts are used to attenuate the propagating sound and they will be presented in later sections. The liners are specified in terms of a complex normal impedance $Z(\omega)$ defined in the frequency domain. Without the flow, the relationship between the complex pressure and the complex velocity amplitude normal to the surface is:

$$Z(\omega) = \frac{p}{\mathbf{v}.\mathbf{n}}\,. \tag{2.62}$$

A frequency-domain impedance boundary condition is defined with the effect impedance Z by:

$$Z = R_0 + i\omega X_1 - \frac{X_{-1}}{i\omega}\,. \tag{2.63}$$

The requirement for a passive impedance and analysis of stability require the limits for the three parameters as $R_0 > 0, X_1 > 0$ and $X_{-1} < 0$ [30].

When a grazing flow is present, it is commonly assumed that pressure and particle velocity are continuous across a thin boundary layer, giving [31]:

$$\mathbf{v}.\mathbf{n} = \frac{p}{Z(i\omega)} + \mathbf{v_0}.\boldsymbol{\nabla}\left(\frac{p}{i\omega Z(i\omega)}\right) - \frac{p}{i\omega Z(i\omega)}\mathbf{n}.(\mathbf{n}.\boldsymbol{\nabla}\mathbf{v_0}). \tag{2.64}$$

The second term on the right hand side represents the convective effect of the grazing flow; the third term is associated with the curvature of the surface.

The formulation of Myers' impedance boundary condition given by Eq. (2.64) has been successfully implemented in the frequency domain simulations [31].

In the time domain, Eq. (2.64) could be transformed as:

$$p'(\mathbf{x},t) = \frac{1}{2\pi}\int_{-\infty}^{\infty} Z'(\mathbf{x},t-\tau)v'_n(\mathbf{x},t)\,d\tau \tag{2.65}$$

where $z'(t)$ is the inverse Fourier transform of $z(\omega)$. However $z(\omega)$is generally defined over a limited frequency range on the real axis, and must therefore be extrapolated over the complex plane in such a way that the problem remains causal, the variables real and the wall passive [38]. Moreover, the complete time history of the normal velocity, $v'_n(\mathbf{x},t)$, must be stored if the convolution integral is to be evaluated in full.

Fung and Ju [35] proposed a model for the reflection coefficient, relating incoming and outgoing velocities, which is called time domain impedance boundary condition (TDIBC). One of the advantages of this method is that it could be applied in both single frequency and broadband noise prediction.

At the frequency domain the reflection wave $\hat{u}^- = \hat{u} - \hat{p} = (1-Z)\hat{u}$ is related to the incident wave $\hat{u}^+ = \hat{u} - \hat{p} = (1+Z)\hat{u}$ by:

$$\hat{u}^- = \widehat{W}(\omega)\hat{u}^+ \tag{2.66}$$

where

$$\widehat{W}(\omega) = (1-Z)/(1+Z). \tag{2.67}$$

The complex function $\widehat{W}$ is indeed a direct measure of the magnitude of the reflection and its relative phase with the incident wave.

The Eq. (2.65) is equivalent to the convolution process of:

$$u^-(t) = \int_{-\infty}^{t} W(t-\tau)\,u^+ d\tau\,. \tag{2.68}$$

This method enables space-time continuation that allows for a non-causal model.

The derivation of single frequency and broadband prediction is shown in Appendix A. New methods proposed recently by Rienstra [36] and Bin and Hussaini [37] are shown in Appendix B.

Centreline Axis Boundary Condition

In a cylindrical coordinate system, the centreline axis for duct cases forms a computational boundary. The radial derivative on the centreline axis is solved using a symmetric computational stencil. This requires mirrored flow quantities on the opposite side of the centre line. On the centreline, the radial velocity v and circumferential velocity w are set to zero. The cylindrical formulations of governing equations contain terms with an inverse dependence on the radial coordinate r. Hence, the singularity of $1/r$ is treated by $\partial/\partial r$ at the singularity.

Buffer Zone Boundary Condition

In the SotonCAA code, a buffer zone boundary condition is employed for boundary initialization and updating. A schematic of a buffer zone set-up is shown as Fig. 2.2.

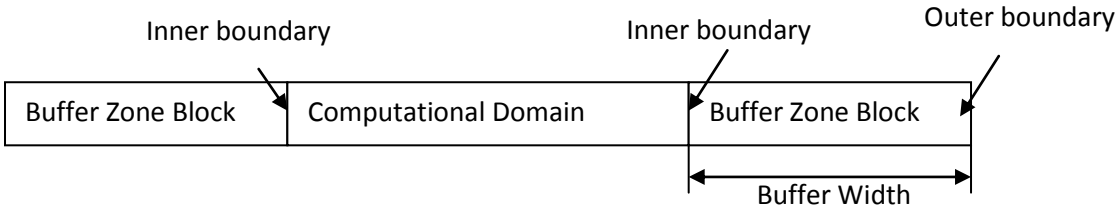

Figure 2.2: Sketch of buffer zone.

The computational domain is extended to be enclosed by a buffer zone. After each time step, the solution is explicitly damped, using:

$$Q^{n+1} = \bar{Q}^{n+1} - \sigma(\bar{Q}^{n+1} - Q_{aim}) \tag{2.69}$$

where $\bar{Q}^{n+1}$ is the solution vector after each time step and Q_{aim} is the expected value in the buffer zone. The damping coefficient σ is defined in Eq. (2.70) and it follows a continuous function:

$$\sigma(x_b) = \sigma_{max} \left|1 + \frac{x_b - L}{L}\right|^{\beta} \tag{2.70}$$

where L is the buffer width, x_b is the distance along the buffer zone and σ_{max} and β are coefficients which determine the shape of the damping function.

2.4 Application of CAA

2.4.1 CAA for Duct Acoustic Propagation and Radiation

The majority of research applying theoretical analysis to acoustic propagation and radiation from turbofan engine intakes has modelled the engine intake as a straight duct. The duct propagation has been usually considered independently of the radiation. This is usually achieved by neglecting the reflection of the duct termination conditions. Radiation models are set by considering an independent system or using the termination conditions. Due to the fact that an engine duct

geometry is generally non-uniform, the theoretical analysis of duct acoustic propagation and radiation is complex. Adding acoustic liners in regions of the engine duct could attenuate the propagation noise efficiently.

2.4.1.1 The Euler Equation

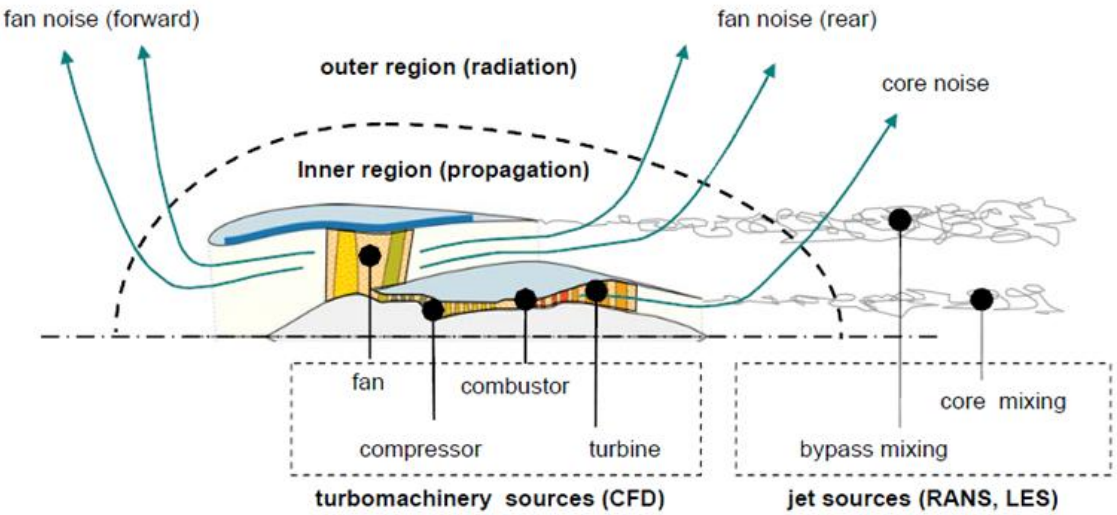

Figure 2.3: Noise sources and transmission paths in a turbofan engine [40].

Fig. 2.3 shows the noise sources and propagation paths in a turbofan engine. The fan is enclosed in a duct. Noise from the fan and the compressor passes through the intake duct into the forward arc. Fan noise also propagates to the rear arc through the bypass duct, radiating through the bypass shear layer. Core noise propagates through the hot and cold exhaust streams and radiates into the rear arc [40].

The typical fan duct, as shown in Fig. 2.3, consists of a cylindrical inlet duct and an annular exhaust duct. The aerodynamic flow through the ducts contains a wide range of subsonic velocities, based on the conditions of the engine. The duct source model is recognised to be independent of propagation and radiation [33]. The acoustic propagation modelling is based on the linearization of the equations governing the isentropic motion for an inviscid, non-heat-conducting perfect gas. The linearised Euler Equations (LEE) are outlined earlier as Eqs. (2.40) and (2.50).

The LEE can be obtained either in the time or the frequency domain.

In the acoustic radiation model the mean flow and the acoustic perturbations are taken as irrotational. Hence, the perturbed velocity can be written in terms of an acoustic velocity potential $\Phi'(\boldsymbol{x}, t)$. The continuity and momentum equations are reduced as follows:

$$\frac{D}{Dt}\left(\frac{\rho_0}{c_0^2}\frac{D\phi'}{Dt}\right) - \nabla.(\rho_0 \nabla\phi') = 0 \tag{2.71}$$

$$p' = c_0^2\rho' = -\rho_0\left(\frac{\partial}{\partial t} + \mathbf{v_0}\nabla\right)\phi' \tag{2.72}$$

Rewriting each dependent variable,$q'(\boldsymbol{x},t)$ in the time-harmonic version of the continuity equation in terms of a complex amplitude $\tilde{q}(\boldsymbol{x})$ at radian frequency ω yields the convected Helmholtz equation:

$$(i\omega + \mathbf{v_0}\nabla)\left[\frac{\rho_0}{c_0^2}(i\omega + \mathbf{v_0}\nabla)\tilde{\phi}\right] - \nabla.\left(\rho_0\nabla\tilde{\phi}\right) = 0 \tag{2.73}$$

This reduces to the standard Helmholtz equation when the mean flow is zero.

2.4.1.2 The Far-field Boundary Condition

The CAA solution must be terminated at the outer boundary of a near-field computational domain without generating spurious numerical reflections. Substituting predicted pressure history on a near-field surface within the computational domain into an integral formulation, the far-field results could be obtained. The Kirchoff integral formation [7] or Farassat's formulation [41] are commonly used tools for acoustic wave radiation prediction.

In SotonCAA, the far-field solutions are given in Lagrangian coordinates $\xi(\mathbf{y},\tau)$, and considering the retarded time $T_l = t - |\mathbf{x} - \mathbf{y}(\xi,\tau_l)|$, the formulation (1A) of Farassat [7] is used as Eq. (2.35).It is also assumed that the contributions from quadrupole terms outside the integration surface are negligible.

2.4.1.3 Broadband Noise

The fan noise consists of both tonal components generated by the rotor-stator interaction and broadband characteristics generated by the turbulent flow over fans and outlet guide vanes, etc., [27]. The pressure fluctuations associated with turbulent flows near the surface of the blades leads to the broadband noise, which contains energy across a wide range of frequencies [42]. Significant sources of broadband noise due to the presence of turbulence in the fan system are from the boundary layer formation on the outer wall of the inlet duct, the wake shed from each rotor blade trailing edge, and from the wake interaction between the rotor wakes impinging on downstream stators when there is a discontinuity between gaseous flows. Due to the system complexity, isolation of each aeroacoustic source is. Furthermore, the turbulence in the inflow can contribute to the overall broadband noise, but its influence is not of great importance.

In the first stage of the compressor of the fan in a turbofan engine, broadband noise is generated in the interaction between the tip of the rotating blade and the turbulent boundary layer formed along the wall of the inlet duct. Here turbulence levels are high and the local blade speed is at a maximum. Turbulence in the wakes shed by the fan blades are also an important source of random noise particularly for fan blades with large surface areas, and it plays an important role in the generation of broadband noise generated in the downstream stages. The broadband noise levels from a multistage core compressor will be higher due as the number of stages increases, due to the increased interaction between rotor and stators.

The challenge in reducing fan broadband noise is to change the airfoil profile on the fan exit guide vanes to reduce the broadband noise at critical noise conditions (approach, cutback and sideline power) without impacting the aerodynamic performance required by design[43] .

2.4.1.4 Current CAA propagation methods

(1) Boundary Element methods(BEM)

The BEM uses the given boundary conditions to fit boundary values into linear differential equations. The BEM uses a defined Greens function, and it is only suited for uniform flow, and is less suited for flow acoustics [44, 45]. If its required computational cost is acceptable, then it could be applied for fully 3D intake problems.

(2) The parabolic equation method

The parabolic equation method splits the wave equation into incoming and outgoing components. When one component of the wave dominates, the factored equation can be solved more efficiently than the full elliptic wave equation. The scheme marches “forward” from the source to the receiver and is inherently fast [46, 47].

(3) Finite element Helmholtz methods

The finite element method is a widely used approach which was first applied to the solution of Helmholtz equation for intake problems and coupled to an infinite element mesh in the far-field [48, 49]. The main advantage its good dispersion characteristics with quadratic elements on unstructured meshes [50]. However, it is restricted to irrotational flows, which restricts it from straightforward use to exhaust propagation problems. Additionally, the solution time scales poorly with problem size [51]. FE schemes based on higher order spectral element and higher order Lagrangian elements have been developed.

(4) LEE, structured methods

Time domain finite difference schemes are widely used to solve the LEE for rotational base flows. Tam and Webb [20] are most well known for these methods with a DRP scheme. Optimised, prefactored compact schemes are also used for a number of structured, time domains LEE problems. They could give more stable stencils near boundaries with less stencil size [49-53].

(5) LEE, unstructured methods

The most promising high order unstructured approach for the LEE is the Discontinuous Galerkin Method which allows variable order of approximation with irregularly shaped elements [52-56].

(6) Solution of the full Euler equations

The advantage of using full Euler equations is that Kelvin Helmholtz instabilities are controlled by nonlinear terms [57], which benefit the nonlinear propagation in the vicinity of the fan.

2.4.2 CAA For liner Optimisation

Based on arrays of Helmholtz resonators, conventional acoustic liners are generally used on the inside surface of commercial aircraft jet engines for fan noise reduction. A Helmholtz resonator (Fig. 2.4) has a short neck which widens into a large volume chamber [56]. Resonance of a Helmholtz resonator is established when the mass of air at air in the neck oscillates against the large volume of air in the chamber. At resonance, small pressure perturbations give rise to large oscillating mass fluxes in the neck. These in turn induce large viscous losses, and narrow band sound absorption is achieved for frequencies close to resonance. In the absence of a mean flow, the absorption coefficient, defined as the proportion of incident energy absorbed, is a non-linear function of the acoustic pressure. High incident acoustic pressures are required before the absorption becomes

significant. In the presence of a mean flow, the absorption is linear and the absorption coefficient is independent of the magnitude of the acoustic pressure. In this instance, absorption is obtained over a wider range of frequencies [57].

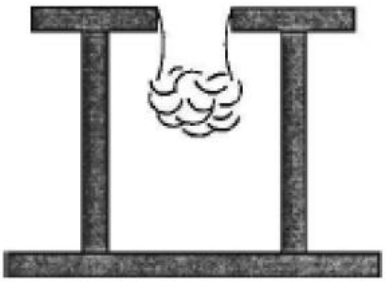

Figure 2.4: Helmholtz resonator [33].

Conventional acoustic liners are normally composed of a perforated plate and a honeycomb core (Fig. 2.5). The honeycomb core is composed of cells which, when bonded to the face sheet, create cavities behind the face sheet. The attachment of an impervious sheet to the honeycomb core seals it thereby isolating each cavity from its neighbors. The main geometric parameters for single layer liner configurations are the porosity, thickness and hole diameter on the pereforated surface, and the depth of the cavities.

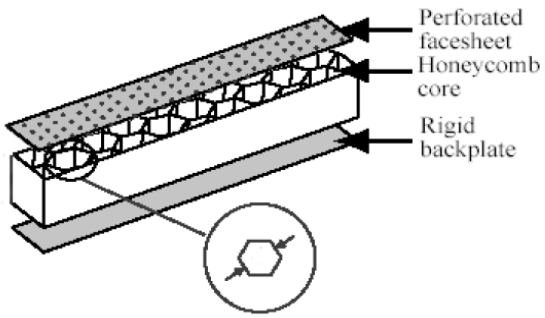

Figure 2.5: Single-layer acoustic liner [33].

Tam and Kurbatskii [61] investigated the mechanisms by which the acoustic energy is dissipated in acoustic liners, using direct numerical simulation of the flow field around and inside a liner resonator under the excitation of plane acoustic waves. A 2D model without outside flow was considered for this investigation. Results gave a better understanding of the flow field and the physics around the opening of a liner resonator when excited by incident acoustic waves. At low sound intensity, a strong oscillatory boundary layer, with a jet-like velocity profile around the opening of the liner, was observed. Most of the dissipation was contributed by the shear gradients of the unsteady boundary layer flows. At high sound intensity, the shedding of micro-vortices from the mouth of the resonator was observed. These micro-vortices carried with them a significant amount of kinetic energy that was eventually dissipated into heat. The shedding of micro-vortices is a very efficient energy dissipation mechanism.

2.4.3 Scattering Case Validation

The aim of this section is to validate the parallel code using the scattering benchmark case. A 2D Gaussian pulse propagation in a uniform flow field case is employed to check the effectiveness of the high order scheme in solving the acoustic problem, by comparing the analytical solution to SotonLEE.

2.4.3.1 Problem Description

Idealizing the fuselage as a circular cylinder and the noise (propeller) as a line source the computational problem from the Second Computational Aeroacoustics (CAA) Workshop is two-dimensional [62] shown in Fig. 2.6.

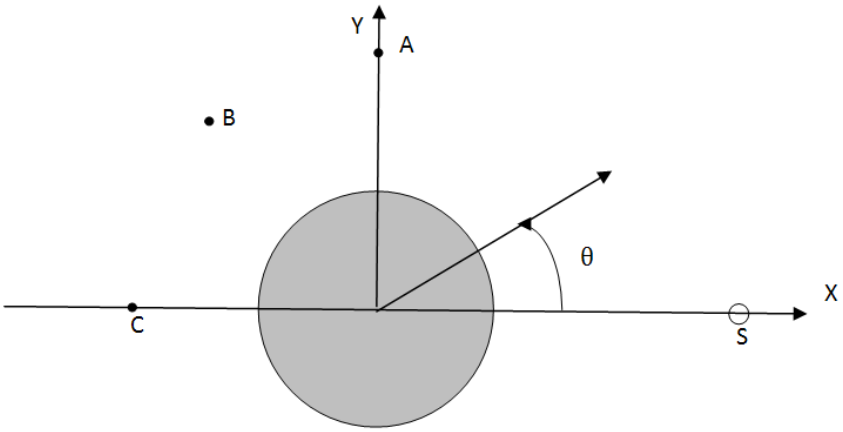

Figure 2.6: 2D Gaussian pulse problem

A 2D cylinder of non-dimensional radius r = 0.5 is located at the origin of a cylindrical coordinate system. An acoustic pulse with initial conditions:

$$u(x,y,0) = 0$$

$$v(x,y,0) = 0$$

$$p(x,y,0) = \exp\left[-ln2\left(\frac{(x-4)^2+y^2}{(0.2)^2}\right)\right] \tag{2.74}$$

is scattered by the cylinder. The computation is performed on a circular domain with the cylinder comprising the inner bound at r = 0.5 metres and the outer bound located at r =10 metres. Three points $A(r=5,\theta=90°), B(r=5,\theta=135°), C(r=5,\theta=180°)$ are chosen as observation points.

2.4.3.2 SotonCAA Simulation

The computational setup for the CAA solution is shown in Table 2.2.

Table 2.2: Computation setup for 2D Gaussian pulse propagation.

Time step	0.002
Total time setup	6000(total time=0.002×6000=12 units)
Main grid (highlighted in green)	401(r) ×381(θ)

Buffer zone grid (highlighted in red)	20(r) ×381(θ)
Temporal scheme	4th-order explicit LDDRK
Spatial scheme	Hixon 6th-order compact scheme
Explicit filtering scheme	10th-order, every time step

Using Gridgen, a computational grid is constructed and is shown below:

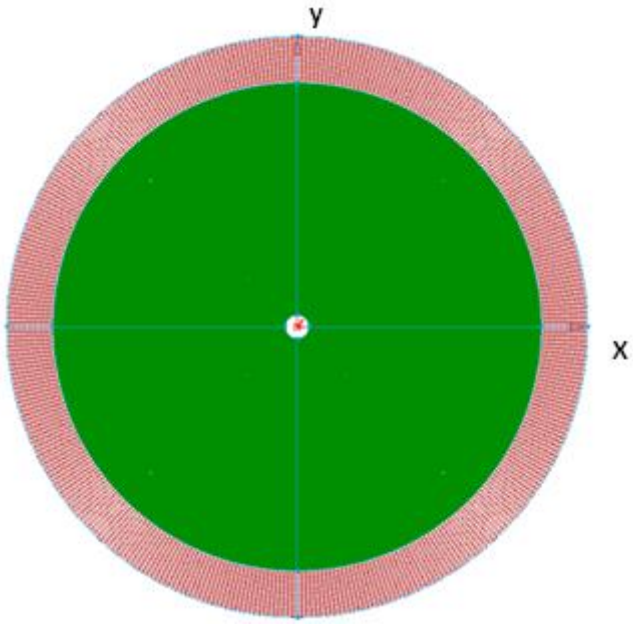

Figure 2.7: Uniform grid produced by Gridgen.

2.4.3.3 FW-H Prediction

The FW-H solver is employed to predict the Gaussian pulse propagation in the far-field. Using the 'CFDtoFWH' code the flow information generated by SotonCAA is transformed into acoustic information and is stored for the aeroacoustics solver. The far-field pressure was predicted by applying an elliptical integration surface which enclosed the source region.

The integration surface is constructed as an ellipse centered at (1.0, 0) with 3 units as the semi-major axis, 2.5 units as the semi-minor axis in a Cartesian coordinate system. Since the FW-H code solves 3D problems, a third dimension was set to span 20 units.

Results predicted by the LEE and the FW-H solver will be compared with the analytical solution presented later (See Appendix C).

2.4.3.4 Results and Discussion

Figs. 2.8 and 2.9 show the contours of pressure at non-dimensional time of t=6 and t=10 using analytical and LEE solutions respectively. The radius of the acoustic pulse has expanded from the source centre, and reflected after the acoustic pressure reached the cylinder. At time t = 6 the large wave front reaches the cylinder surface and a small reflected wave can be seen near the cylinder. At t =10 the initial pulse has already reached the outer boundary and a smooth transition through the

domain edge is observed as expected.

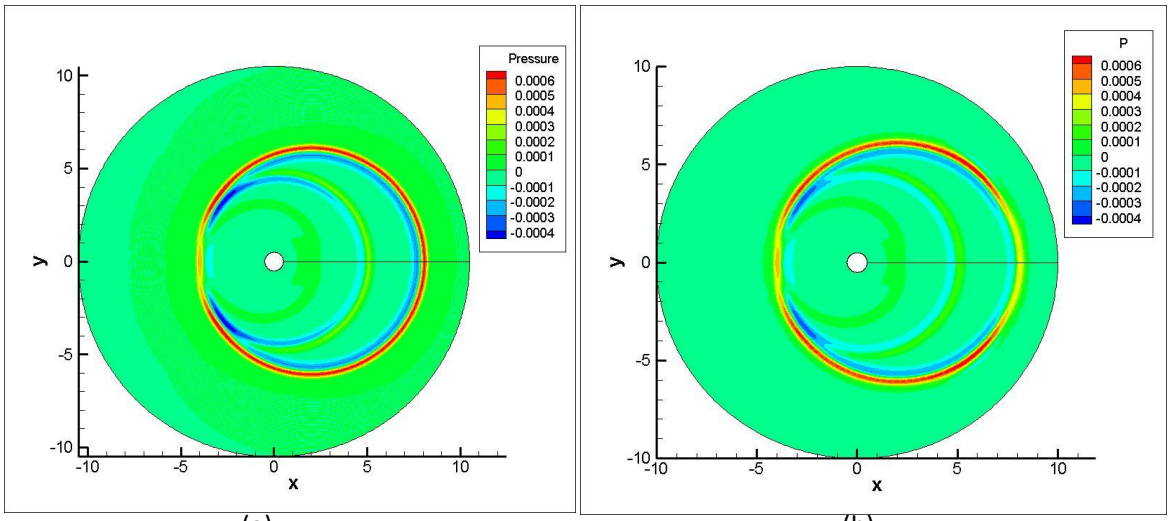

(a) (b)

Figure 2.8: Contours of pressure at non-dimensional time t=6 (a) LEE, (b) analytical solution.

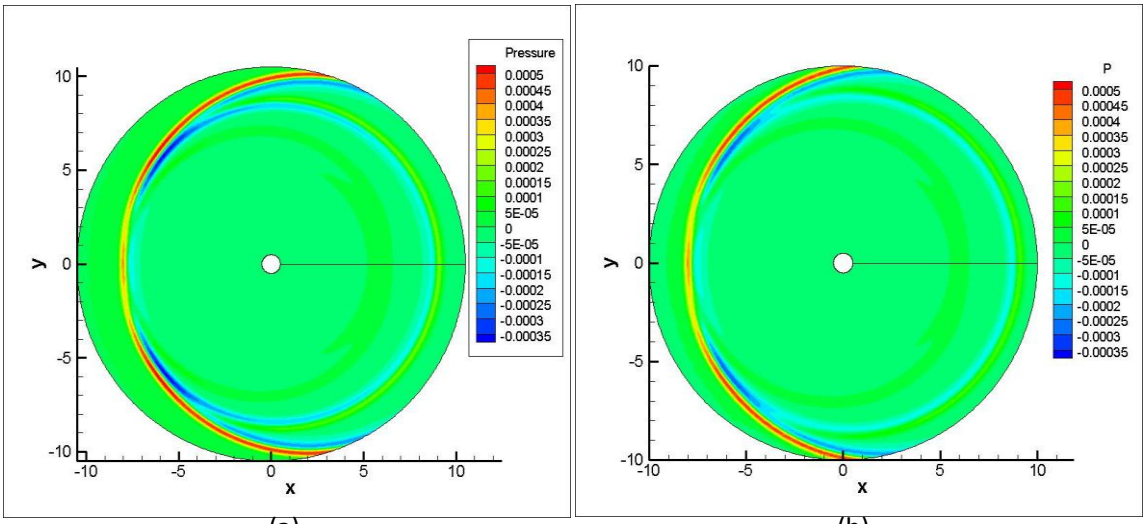

(a) (b)

Figure 2.9: Contours of pressure at non-dimensional time t=10 (a) LEE, (b) analytical solution.

It can be seen that the LEE results are almost identical to the analytical solutions at corresponding time steps. Fig. 2.10 shows computed pressure histories in comparison with the analytic solution given above. These results show satisfactory agreement between the LEE and analytical solutions. Using the FW-H solver, similar solutions for the computed pressure time histories to those predicted by SotonCAA were obtained and are shown in Fig. 2.11.

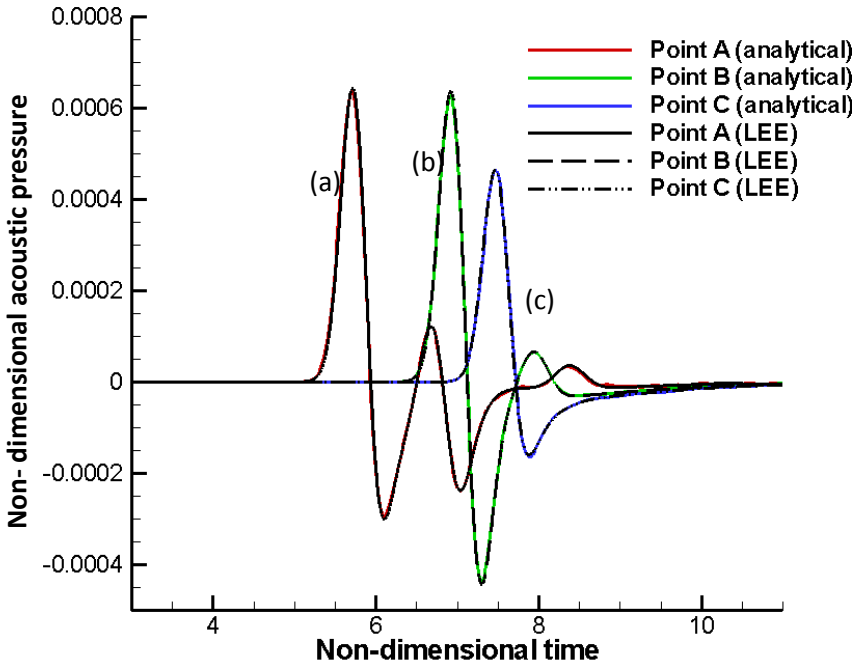

Figure 2.10: Comparison between analytic and computed solutions of 2D scattering problem. (a) Pressure history at $A(r = 5, \theta = 90^{\circ})$. (b) Pressure history at , $B(r = 5, \theta = 135^{\circ})$ (c) Pressure history at $C(r = 5, \theta = 180^{\circ})$.

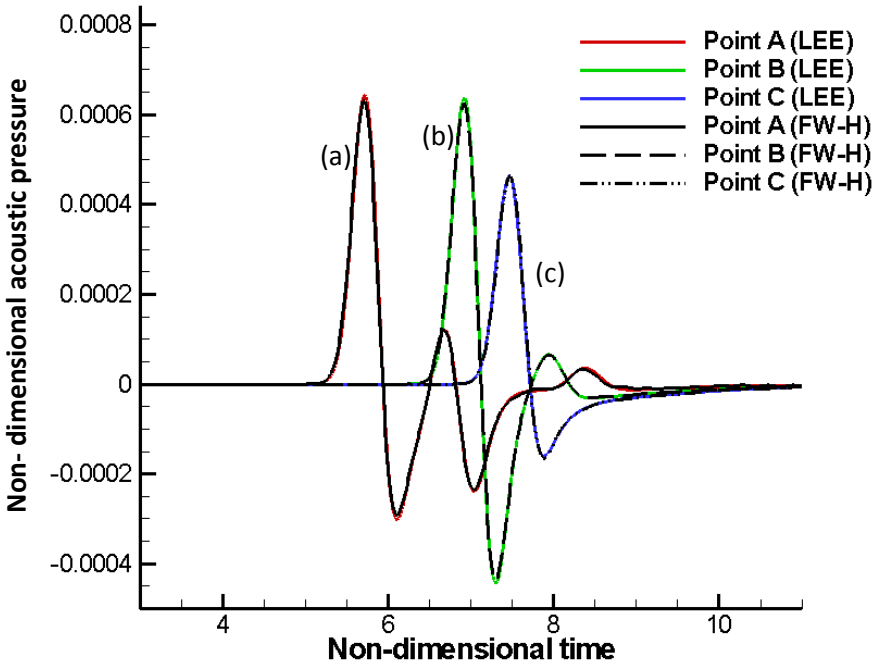

Figure 2.11: Comparison between SotonLEE and computed solutions of 2D scattering problem. (a) Pressure history at $A(r = 5, \theta = 90^{\circ})$. (b) Pressure history at , $B(r = 5, \theta = 135^{\circ})$ (c) Pressure history at $C(r = 5, \theta = 180^{\circ})$.

The pressure history at the monitor points calculated by various methods has been compared. It is shown that the results computed by the LEE and the FW-H solver match well with those obtained by the analytical solution. Good agreement of the pressure amplitude can be observed between computational results with a fine mesh and analytical results. In general, the research code performs

well in solving this 2D acoustic problem compared to the exact solutions, and it is extendable to 3D in a straight-forward manner.

3 Acoustic Intensity-Based Method

A hybrid approach separates the acoustic field into an aerodynamic source, and acoustic propagation region, and is commonly used for predicting aerodynamic noise. Conventional CFD solvers are generally employed to evaluate the flow field in the near-field to provide the aerodynamic sound source information. The extension of the near-field CFD solution to the mid-field acoustic radiation can be achieved using the LEE method, but its use may be limited due to an excessive demand in computer storage. As for far-field radiation, the FW-H prediction requires a closed control surface containing the entire aerodynamic source region. As stated previously, the current FW-H solver has difficulty evaluating results for multi-frequency cases due to large memory requirement, and it can only be applied to cases with frequency numbers less than three. This provides the motivation to explore an alternative far-field prediction method.

Motivated by the need for an accurate and efficient prediction of far-field acoustic radiation, an acoustic intensity-based method (AIBM) [2-4] has been developed by Chao Yu et al. The AIBM assumes that the sound propagation is governed by the simple wave equation on and outside a control surface that encloses all the nonlinear effects and noise sources. The prediction of the acoustic radiation field is however carried out by the inverse method by using the acoustic pressure derivative and its simultaneous, co-located acoustic pressure over an open control surface. The reconstructed acoustic radiation field using the AIBM is unique due to the unique continuation theory of elliptic equations. Hence the method is more stable and the reconstructed acoustic pressure is less dependent on the locations of the input acoustic data. The AIBM is based on an equal acoustic power assumption so that for a combination of multi-acoustic sources each acoustic source has the same acoustic intensity level. Therefore the AIBM is capable of multi-source prediction.

3.1 AIBM Mathematical Formulations

In 3D, assuming that the mean flow is unvaried in the z direction, the solution of the Helmholtz equation can be shown as:

$$f(x,y,z) = \exp(ikM\tilde{z}\alpha^{-2}) \sum_{n=0}^{\infty} \sum_{m=0}^{n} \left(a_n \cos m\tilde{\theta} + b_n \sin m\tilde{\theta}\right) P_n^m\left(\cos\tilde{\phi}\right) G_n(k\tilde{r}\alpha^{-2}) \qquad (3.1)$$

where parameters $(\tilde{r},\tilde{\theta},\tilde{\phi})$ are defined for the modified spherical coordinates from Cartesian coordinates (x,y,z) in the physical domain, and $\alpha = \sqrt{1-M^2}$. P_n^m is the associated Legendre polynomial and G_n represents the generalized Hankel function or spherical Hankel function.

Let $(\tilde{x},\tilde{y},\tilde{z})$=$(\alpha x, \alpha y, z)$, then:

$$\tilde{x} = \tilde{r}\sin\tilde{\phi}\cos\tilde{\theta}, \qquad \tilde{y} = \tilde{r}\sin\tilde{\phi}\sin\tilde{\theta}, \qquad \tilde{z} = \tilde{r}\cos\tilde{\phi}, \qquad \tilde{r} = \sqrt{\tilde{x}^2+\tilde{y}^2+\tilde{z}^2}. \qquad (3.2)$$

Differentiating both sides of Eq. (3.1) with respect to the unit normal vector $\hat{n} = \left(n_x, n_y, n_z\right)$ and using the chain rule, we have the formula for normal derivative of f:

$$g(r,\theta,\phi)=\frac{\partial f}{\partial \hat{n}}=\frac{\partial f}{\partial \tilde{r}}\frac{\partial \tilde{r}}{\partial \hat{n}}+\frac{\partial f}{\partial \tilde{\theta}}\frac{\partial \tilde{\theta}}{\partial \hat{n}}+\frac{\partial f}{\partial \tilde{\phi}}\frac{\partial \tilde{\phi}}{\partial \hat{n}} \tag{3.3}$$

Note that:

$$\frac{\partial \tilde{\theta}}{\partial \hat{n}}=\frac{1}{\tilde{r}}\left(\alpha n_y-\tilde{r}\cos\tilde{\phi}\sin\tilde{\theta}\frac{\partial \tilde{\phi}}{\partial \hat{n}}-\sin\tilde{\phi}\sin\tilde{\theta}\frac{\partial \tilde{r}}{\partial \hat{n}}\right), \tag{3.4}$$

$$\frac{\partial \tilde{\phi}}{\partial \hat{n}}=\frac{1}{\tilde{r}\sin\tilde{\phi}}\left(\cos\tilde{\phi}\frac{\partial \tilde{r}}{\partial \hat{n}}-n_z\right). \tag{3.5}$$

There are singularities at $\phi=0$ and π, which will present computational difficulties.

To remove these singularities, $\cos m\tilde{\theta}$ and $\sin m\tilde{\theta}$ can be expressed as:

$$\begin{cases}\cos m\tilde{\theta}=\dfrac{1}{2}\left(e^{im\tilde{\theta}}+e^{-im\tilde{\theta}}\right)=\dfrac{1}{2\tilde{r}^m\sin^{\mathrm{m}}\tilde{\phi}}[(\tilde{x}+i\tilde{y})^m+(\tilde{x}-i\tilde{y})^m]\\ \sin m\tilde{\theta}=\dfrac{1}{2i}\left(e^{im\tilde{\theta}}-e^{-im\tilde{\theta}}\right)=\dfrac{1}{2\tilde{r}^m\sin^{\mathrm{m}}\tilde{\phi}}[(\tilde{x}+i\tilde{y})^m-(\tilde{x}-i\tilde{y})^m]\end{cases} \tag{3.6}$$

Substituting above equation back to Eq. (3.1), we have:

$$f(x,y,z)=\exp(ikM\tilde{z}\alpha^{-2})\sum_{n=0}^{\infty}\sum_{m=0}^{n}(a_n\xi_m-ib_n\eta_m)Q_n^m\left(\cos\tilde{\phi}\right)G_n(k\tilde{r}\alpha^{-2})/(2\tilde{r}^m) \tag{3.7}$$

where

$$\xi_m=(\tilde{x}+i\tilde{y})^m+(\tilde{x}-i\tilde{y})^m,\ \eta_m=(\tilde{x}+i\tilde{y})^m-(\tilde{x}-i\tilde{y})^m \tag{3.8}$$

and $Q_n^m=P_n^m/\sin^{\mathrm{m}}\tilde{\phi}$. From the expression for P_n^m, we see that

$$Q_n^m\left(\cos\tilde{\phi}\right)=\frac{(-1)^{m+n}}{2^n n!}\frac{d^{n+m}}{d\omega^{n+m}}(1-\omega^2)^n|_{\omega=\frac{\tilde{z}}{\tilde{r}}} \tag{3.9}$$

which has no singularity. This could improve the general solution of the Helmholtz equation. The normal derivative can be derived easily from

$$g(x,y,z)=\frac{\partial f}{\partial \hat{n}}=\frac{\partial f}{\partial \hat{x}}\alpha n_x+\frac{\partial f}{\partial \hat{y}}\alpha n_y+\frac{\partial f}{\partial \hat{z}}n_z \tag{3.10}$$

In order to find details of the solution of Eq. (3.1), it is necessary to determine the coefficients a_n and b_n. Both coefficients are determined by matching the assumed form of the solution to the measured acoustic pressure and its normal derivative over the input surface segments. Once these coefficients are determined, the solution can be quickly evaluated at any field points on or outside the control sphere. In the AIBM, both the acoustic pressure and its simultaneous, co-located derivative (in out normal direction) on the boundary Γ_1 are given as the inputs for the reconstruction of the acoustic field in the domain Ω (see in Fig. 3.1). With the pressure derivative boundary condition as an additional input for the inverse problem, the uniqueness of the reconstructed solution is guaranteed from the unique continuation theory of elliptical equations. The method also

yields a consistent and accurate solution on and outside of the control sphere. In using the AIBM, it is assumed that the control sphere is known, although the exact locations of sound sources may not be available.

In the AIBM, the partial boundary value problem is defined as:

$$\begin{cases} \nabla^2 P - M^2 P_{xx} - 2ikMP_x + k^2 P = 0, \ \ in\ \Omega = R^2 \backslash \Omega_{\text{in}} \\ P|_{\Gamma_1} = g_1, \partial_\gamma P|_{\Gamma_1} = g_2 \end{cases} \tag{3.11}$$

where γ is the outward normal to Γ_1.

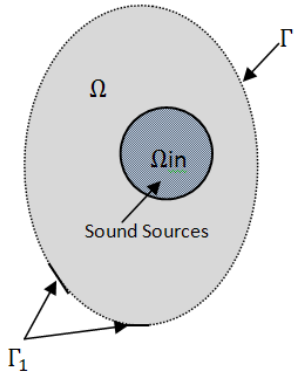

Figure 3.1: Schematic diagram of sound propagation field and locations of acoustic measurements [4].

The numerical solutions for Eq. (3.1) or (3.7) are obtained from the following steps

(a) The solutions are approximated by a finite summation instead of an infinite summation. Therefore Eq. (3.7) becomes:

$$f(x,y,z) = \exp(ikM\tilde{z}\alpha^{-2}) \sum_{n=0}^{N} \sum_{m=0}^{n} (a_n \xi_m - ib_n \eta_m) Q_n^m\left(\cos\tilde{\phi}\right) G_n(k\tilde{r}\alpha^{-2}) \,/ (2\tilde{r}^m) \tag{3.12}$$

The upper limit N must be chosen large enough to satisfy the accuracy requirement, and small enough to include the characteristics of input acoustic data into consideration, and save the computer source.

(b) The coefficients a_n and b_n are determined by matching the assumed form of solution to the input data $f(x,y,z)$. The most popular method is least square method for this linear system.

For axisymmetric problems, considered in 2.5D, the 3D formulations can be simplified into a 2.5D formulation. Once $\tilde{\theta}$ is specified in Eq. (3.1), e.g. $\tilde{\theta} = 0$ ($\xi_m = 2\tilde{x}^m, \eta_m = 0$), the equation can be transformed to:

$$f(x,0,z) = \exp(ikM\tilde{z}\alpha^{-2}) \sum_{n=0}^{N} \sum_{m=0}^{n} a_{nm} Q_n^m\left(\frac{\tilde{z}}{\tilde{r}}\right) G_n(k\tilde{r}\alpha^{-2}) \,/ (\tilde{r}^m) \tag{3.13}$$

The normal derivative can be derived easily from

$$g(x,0,z) = \frac{\partial f}{\partial \hat{n}} = \frac{\partial f}{\partial \hat{x}} \alpha n_x + \frac{\partial f}{\partial \hat{z}} n_z \tag{3.14}$$

3.2 Validation

Following the equation of AIBM described previously, two 2D test cases that combine CAA and AIBM were conducted in order to validate the AIBM for physical problems and are shown below.

3.2.1 Case one: multiple sources in a uniform flow

A combination of one monopole, one dipole and two quadrupoles in a 2D domain is used for the acoustic radiation. The pressure generated by a dipole and quadrupole can be written as a summation of a monopole generation. i.e.$P(r,\theta) = \sum_{i=1}^{L} (A_0)_i \, H_0(kR_i)$, where A_0 is the strength of the monopole and R_i is the distance between a field point and the monopole source. The strength and locations of these sources in this case is same in reference [4], shown as Table 3.1.

Table 3.1: The strength and distribution of the acoustic sources.

	$A_0(\mathrm{W/m^2})$	$x(m)$	$y(m)$
Quadrupole I	1.00	0.30	0.60
	-1.00	-0.10	0.60
	1.00	-0.10	0.20
	-0.10	0.30	0.20
Quadrupole II	-1.20	0.49	-0.12
	1.20	0.20	-0.20
	-1.20	0.28	-0.49
	1.20	0.57	-0.41
Dipole	-0.80	-0.54	-0.16
	0.80	-0.78	-0.45
Monopole	0.90	-0.58	0.58

All the acoustic sources are located within the circle of radius $r = 1m$. The wave number of the sources is considered as $k = 2m^{-1}$ and the control sphere is then defined by the circle of radius $r_m = 3m$. The reconstruction of acoustic radiation pressure is worked out on and out of the control sphere. The input data are given at a continuous arc between $(\mathrm{r}_1 = 6m, \theta_1 = 63\pi/128)$ and $(\mathrm{r}_1 = 6m, \theta_2 = 65\pi/128)$ in the polar coordinates, as shown in Fig. 3.2. Dividing the arc into even 20 segments, the acoustic pressures and their derivatives normal to the segments are used as the input data. It should be noted that it uses an open surface for the reason that in some cases there may not be enough data for the whole surface.

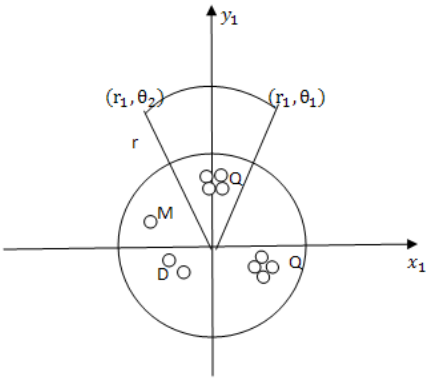

Figure 3.2: Schematic diagram of acoustic sources and input locations

A further study is carried out to verify if the gradient pressure in the input data could improve the accuracy and consistency of the results (AIBM solution without gradient pressure named as AIBM_without).The predicted radiation with and without a pressure gradient, at $r = 50m$ is compared with the analytical solution shown in Fig. 3.3. It is shown that the reconstructed acoustic pressures agree reasonably well with the analytical solution for cases with and without a pressure gradient. However, the result without a derivative pressure input is less dependable than one with a pressure derivative. All the results are similar, according to reference [60].

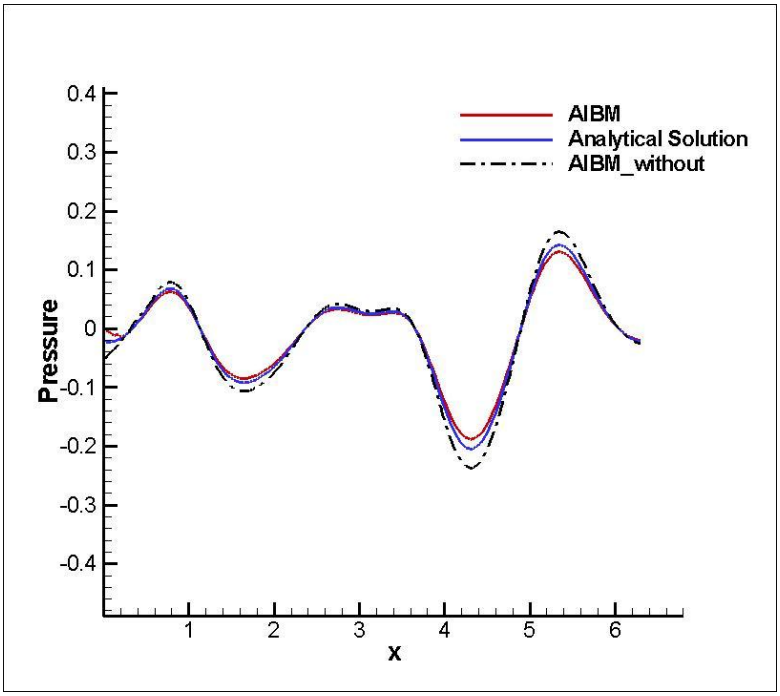

Figure 3.3: Comparisons of acoustic pressure with analytical solution at r=50m.

3.3.2 Case two: Acoustic Propagation and Radiation from an Axisymmetric Duct

An axisymmetric geometric model of a duct bypass with a mean flow is tested. Acoustic perturbations are propagating downstream through the axisymmetric duct and radiating to far-field. The schematic of the duct configuration is shown in Fig. 3.4. For the near-field, the LEE method could predict the pressures and other characters. For the far-field radiation, a FW-H method coupled with

the LEE could be used for prediction. Calculations are conducted for a uniform flow with a mean axial velocity. The mean flow values are given in table 3.2 and are used to non-dimensionalise all variables shown in the results presented in this section. The free stream speed of sound is calculated from the free stream temperature by the relation $c_\infty = \sqrt{\gamma R T_\infty}$, where $\gamma = 1.4, R = 287 J/kgK$. The characteristic length scale L, is the duct radius $r = 1$.

Table 3.2: Bypass duct case background mean flow value

Mean Flow	
Temperature (K)	299.2
Density (kg/m^3)	1.25
Pressure(Pa)	112058

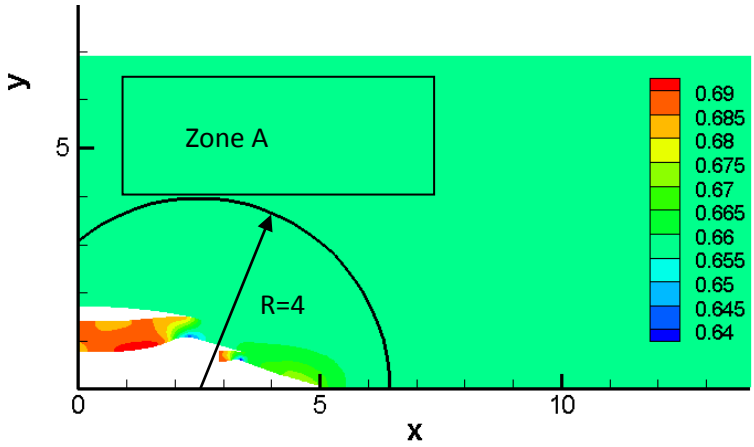

Figure 3.4: Schematic of the mean flow pressure distribution for the duct.

The computational grid is shown in Fig. 3.5. This is done following the results of Zhang et al [27].The grid contains 0.49×10^6 cells with 10 PPW minimum for resolution in both x and y directions. The acoustic wave is admitted into the duct through a wave admission region. Buffer zone condition with explicit damping (Eq. 2.68) is applied so that it can introduce the acoustic wave into the domain whilst allowing any acoustic waves from the duct opening to propagate out of the domain with minimal reflections.

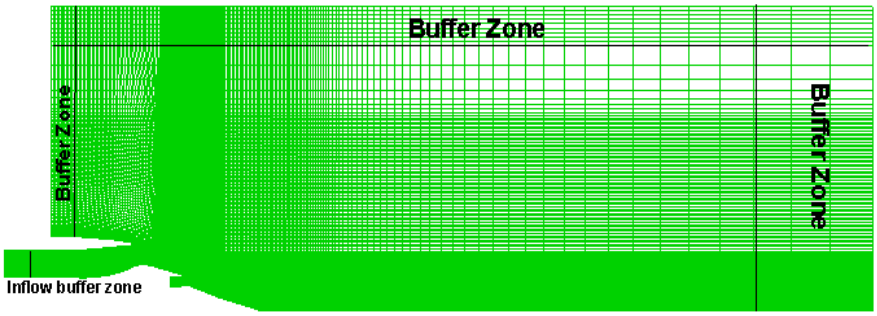

Figure 3.5: The grid of computational domain

For the FW-H method, it is based on using as an input of the unsteady perturbation pressure and velocity over a closed FW-H surface that encloses the acoustic sources to predict the far-field

pressure radiation, whereas AIBM can be coupled with the LEE method with an open integration surface, with less computational storage requirement.

Since AIBM is based on the frequency domain, while the current LEE solver is based on time domain, the near-field acoustic pressure comparison could be selected at several points. The input acoustic pressure and pressure gradient are chosen as shown in Fig. 3.4, along the arc of r=4, the arc is between $(4, \pi/3)$ and $(4, 2\pi/3)$. 20 points with an interval of $\pi/30$ along the arc in different time step are chosen (shown as **N** in Fig 3.6) for comparison with the CAA solution.

With a defined duct acoustic mode of $m = 2, n = 1$ the radiation of acoustic pressure at $r = 5$ in the near-field is predicted using the 2.5D AIBM equation (Eq.3.13) and the results are shown as Fig. 3.6. By comparing with the LEE solution, it can be observed that the agreements of the pressures (shown as **P** in non-dimensional form) are satisfactory. The results demonstrate that the AIBM solution is compatible with the LEE solution.

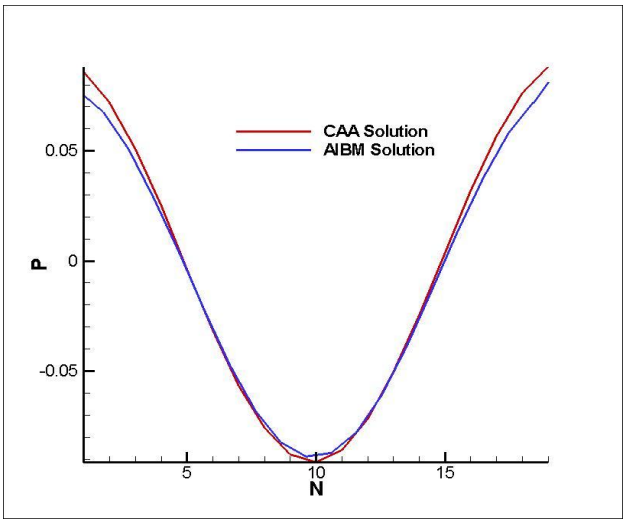

Figure 3.6: Comparison of pressure patterns at the same time.

More precisely for the near flow field, a simple domain was established for the comparison of the near filed sound pressure outside the source area (zone A shown in Fig. 3.4). There are only slight differences between the two figures shown in Figs. 3.7(a) and (b). The overall features are the same. This again verifies that the AIBM solution is suitable for predicting the duct acoustic pressures.

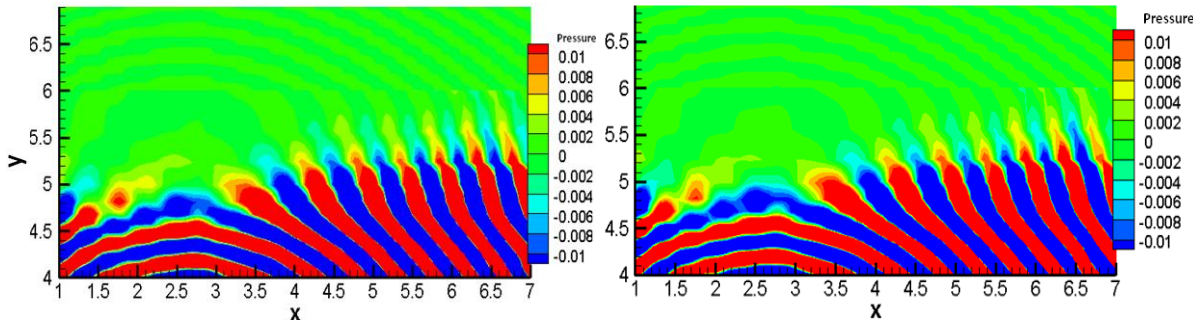

(a) (b)

Figure 3.7: Acoustic pressure comparison in near-field domain. (a) LEE solution (b) AIBM solution.

For the far-field pressure prediction, the SPL directivity comparison between the AIBM and FW-H results is shown in Fig. 3.8. The results are taken at 10 metres from the original axis (2.5, 0). The patterns are similar while the quality, to some extent, is different. For the observation angles below 30°, the difference is mainly because the source terms are contained as input data, which has a negative influence on the results. The SPL reaches its peak value at an observation angle around $\varphi = 56^{\circ}$, and then reduces gradually as the angle increases. In this case, the AIBM saves up to 67% memory expensive compared with FW-H method since it only requires the pressure on the integration surface.

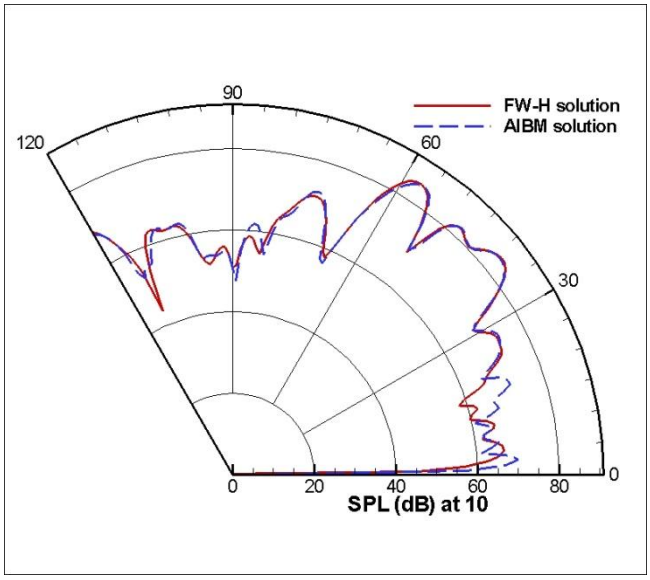

Figure 3.8: Far-field directivity comparison.

In summary, the AIBM method has been verified for a 2D configuration. The predicted acoustic fields by AIBM for the cases agree well with the analytical, LEE, and FW-H solutions. AIBM could be used to predict the far-field pressure and it only depends on the pressure distribution on the integration surface which is calculated by LEE. It is much easier than the FW-H method which requires more components to do the computation for the far-field pressure. Additionally, AIBM could be used on an open integration surface if there is not enough input data. Hence, the AIBM would save on computational effort and storage. However, since the aim of the research is to predict the broadband acoustic pressures, the prediction method requires further studying. For the multi-frequency problem a suitable solver is also required, and will be presented in the next chapter through a detailed study on the effect of bifurcations in a duct.

4 Sound Radiation from a Bypass Duct with Bifurcations

In this section, prediction of the propagation and radiation of spinning modes generated by an axisymmetrical engine fan and fan/stator flow interaction is considered in both two and three dimensions. The LEE method is able to predict the near-field sound wave propagation of small acoustic perturbations compared to the background flow. The far-field sound wave radiation is currently predicted using the FW-H solver using the data provided by SotonCAA on an integration surface as an input for single acoustic modes. Since the current FW-H solver cannot solve the multi-mode problem due to a large memory requirement, the sound radiation is compared within the computational domain. AIBM can be an alternative method to use for far-field prediction of multi-modes once its development is completed.

In this research a newly developed LEE solver is used to explore the bifurcation effects due to multi-mode inputs in a generic engine bypass duct. An axisymmetrical bypass duct is installed with four bifurcations along the circumferential direction with equal spacing. With such a duct configuration we want to explore the effects of the bifurcations with multimode acoustics. Results without bifurcation have been used for comparison.

The duct geometry includes bifurcations, the bypass and exhaust ducts. Four bifurcations are located at angular intervals of 90° along the circumferential direction, connecting the inner and the outer bypass duct walls. Since the bifurcations occur with equal spacing, one quarter model of the engine duct configuration for a generic engine can be used in the study and it is shown in Fig. 4.1.

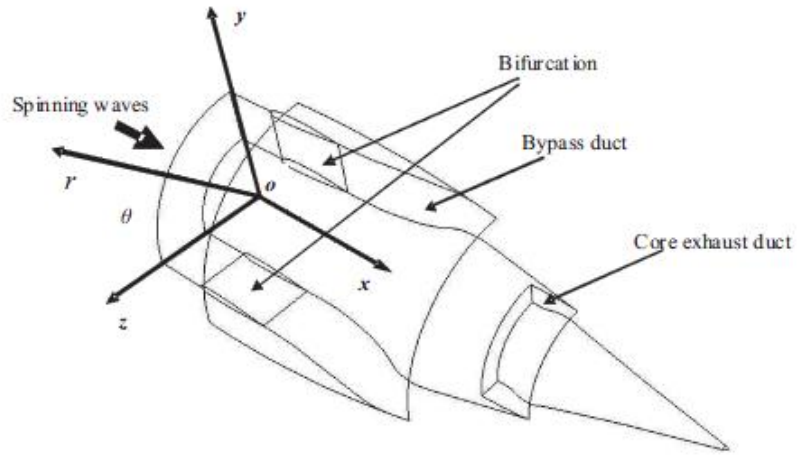

Figure 4.1: Schematic of aft duct of a generic engine with bifurcation [63].

The inner wall radius of the exhaust is 0.57m.The radius of the exhaust cone is 0.23m. The radius of the inner wall of the bypass duct is 0.79m and the inner hub radius is 0.6m. In this computation, the length of the bypass duct from the spinning mode entry area to the duct exit is 4m. The bifurcations have a cross section profile of a NACA 0012 airfoil with a chord of 1m. The starting position of the

bifurcation is 3m away from the bypass duct exit. The installation angles for the four bifurcations in the circumferential (θ) coordinates are at 0°, 90°, 180° and 270° respectively.

The computations were performed on a structured grid according to reference [63] and shown in Fig. 4.2. The grid for computation contains 1.27×10^{6} cells and the grid resolution has a minimum 9 PPW in both circumferential and radial directions.

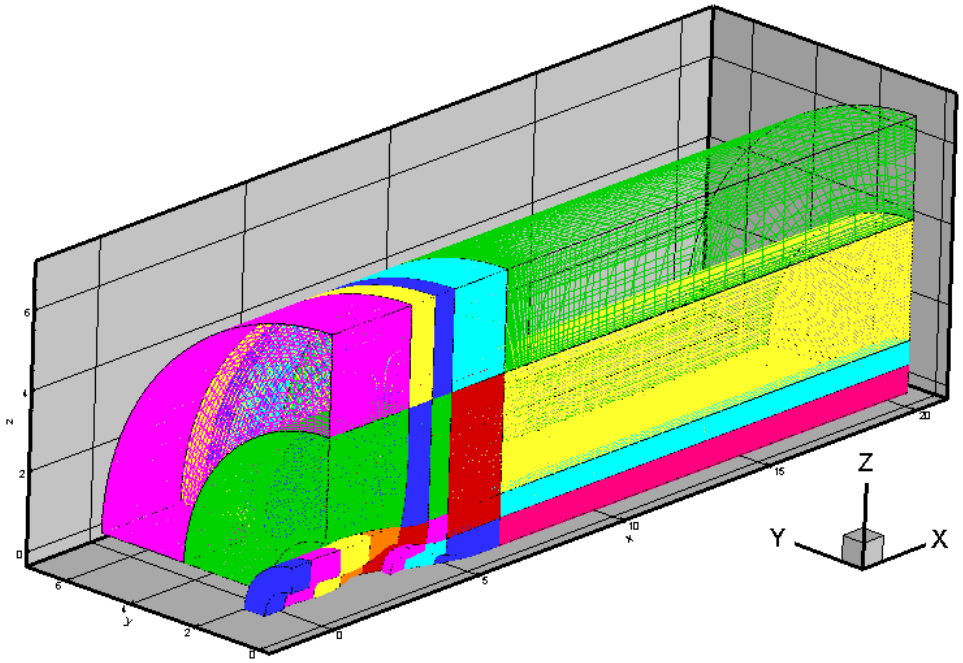

Figure 4.2: The grids of the quarter engine duct with bifurcation.

The problem setup is illustrated in Figs. 4.1 and 4.2, which show the computational domain in near-field propagation. In order to study the effect of bifurcations, an axisymmetric bypass duct case in 2D using a 2.5D LEE model at $\theta = 90^{\circ}$ is also computed.

4.1 Numerical Model Implementation

The newly developed LEE (Eq. (2.50)) in complex form, which can be solved for multi-mode problems, is used as governing equations for the acoustic computations and all variables were non-dimensionalised using a reference length of 1m, a reference density of $1.225\mathrm{kg/m^3}$, and a reference sound speed of 346.76 m/s. If not defined specifically all values shown below are in non-dimensional form.

The temporal scheme used in the computations is a low dissipation and dispersion Runge-Kutta [61] scheme and the spatial scheme is a 6^{th}-order accuracy compact scheme [28], which has been stated previously. An explicit filter of 10^{th}-order accuracy [34] is used at every time step to remove small numerical disturbances. For multi-mode computation the acoustic pressure amplitude of each mode is defined to have an acoustic intensity level of 100dB.

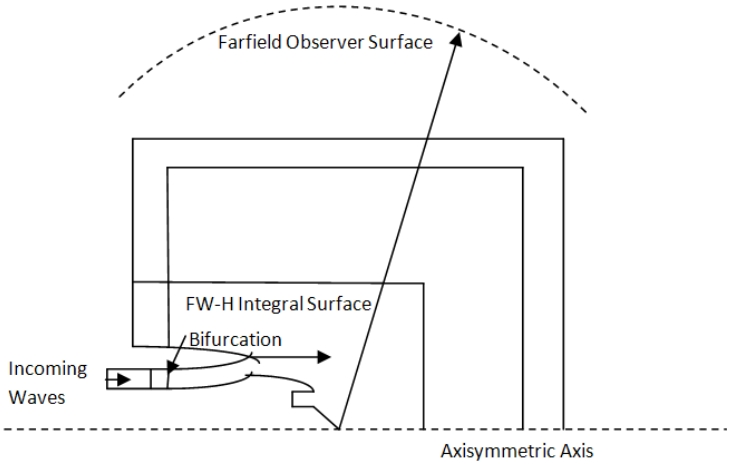

Figure 4.3: Setup including bypass duct and exhaust geometry.

For the boundary treatment, the inflow and outflow buffer zones were introduced to minimize possible spurious wave reflections at the computational boundaries. A periodic boundary condition was applied at the boundaries in the circumferential direction except at the bifurcations. A slip-wall condition was applied to all wall boundaries including the bifurcation boundaries. A symmetric flow condition was applied at the axis. Estimation of far-field acoustic radiation was performed separately based on the near-field computation results through the FW-H equation for single mode. The far-field directivity was calculated at 100m away from the symmetric axis, shown in Fig. 4.3.

The steady background flow was solved by the Reynold Average Navier-Stokes (RANS) with a $k-\omega$ turbulence model. The inflow conditions were as follows; at the bypass duct the pressure was 112058Pa with a Mach number of 0.27. The free stream conditions were set to a pressure of 101325Pa with Mach number of 0. The temperature was set to a constant of 299.2K. The mean flow pressure and velocity in 2D plan are shown in Figs. 4.4 and 4.5.

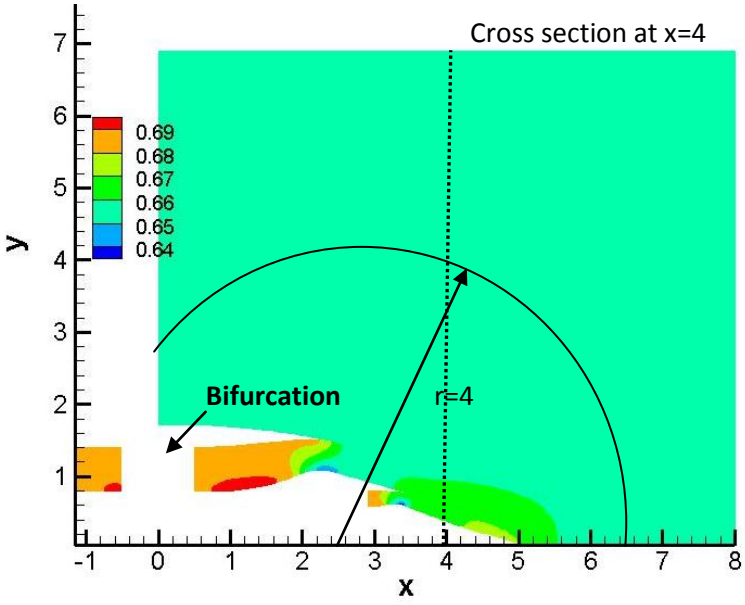

Figure 4.4: Non-dimensional mean pressure distribution.

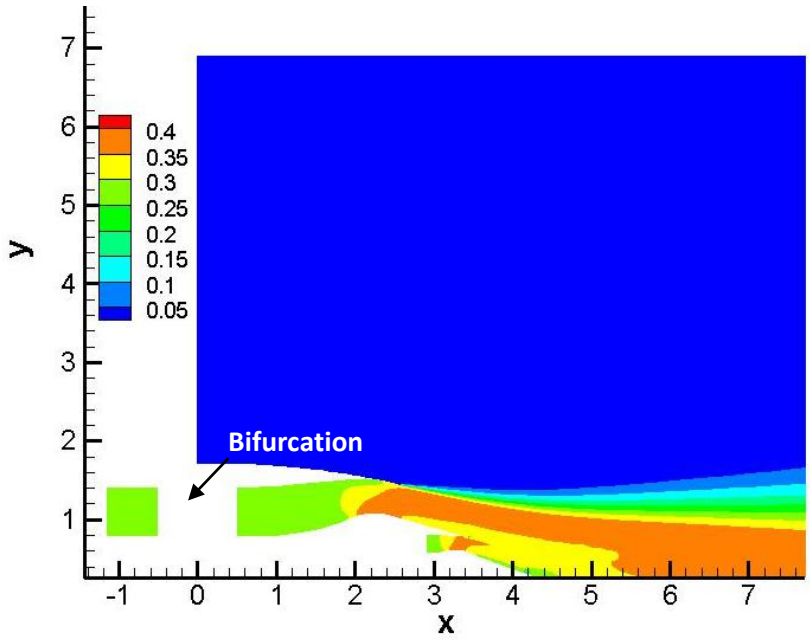

Figure 4.5: Non-dimensional mean axial velocity distribution.

The results were taken after 50 wave periods after which the wave fronts were propagated out of the computational domain and the solution became periodic.

The FW-H equation solver was used to determine the far-field noise level for single frequency cases. The FW-H integration surface was placed outside of the duct to enclose the source region. For the comparison study an elliptic integration surface was used and was generated by substituting values at $x_a = 3.8, y_a = 1.6, x_c = 2.5, y_c = 0.0$ into Eq. (4.1).

$$\frac{(x - x_c)^2}{x_a^2} + \frac{(y - y_c)^2}{y_a^2} = 1 \tag{4.1}$$

where x_c and y_c are the coordinates of the ellipse centre point and x_a and y_a are the ellipse half-widths in the axial and radial directions respectively. The 3D integration surface is generated by extending the surface in the cylindrical azimuthal coordinate.

The observation points are over a 120 degree arc consisting of 121 observer positions at a distance of 100m relative to the coordinate system origin. A zero degree angle corresponds to the downstream direction along the centre line of the duct geometry.

The computing facility is the Iridis3 HPC cluster at the University of Southampton, which consists of 1008 8-core nodes (Intel Nehalem 2.26 GHz) with a minimum 22 GB of memory per node. All nodes are connected to a high speed disk system with 110TB of storage with a fast infiniband network for parallel communication.

The computation time for the 3D simulation was 8 hours on 12 processors while the 2D case consists of many fewer grids and requires only about 3 hours of computing time on a single processor.

4.2 Results and Analysis of Bifurcation Cases

4.2.1 Clean Duct Cases

According to reference [27], previous work has been done on multi-frequency simulated in a single computation for a generic duct case, and compared with the Munt's analytical solution. In this section, a clean duct case has been studied for multi-frequency using the complex LEE method given by Eq. (2.47) and Eq. (2.50). The effect for different radial and circumferential modes is presented.

For general cases, the realistic duct geometry may be non axisymmetric and contain a multitude of spinning acoustic modes. These problems can be solved through solutions of full 3D Euler governing equations, while avoiding numerical instability excited in the downstream shear layer. However, the computational cost is high. For an axisymmetric mean flow problem, the 2.5D LEE/FWH hybrid acoustic method for the computation of acoustic radiation could be used to give an efficient prediction in both the near and the far-field, on the condition that the propagation of the total multi-mode can be generated from the superposition of single mode results. The comparisons with 3D cases have been done as follows.

4.2.1.1 Comparison Multi-frequency SPL and Summed near-field SPL

Figs. 4.6 and 4.7 show the SPL contours for multi-frequency and for the superposition of three different frequencies from 1000Hz to 2000Hz with an interval of 500Hz with the mode kept as (12,1). For the superposition shown in Fig. 4.7, the SPL is calculated separately for the three different frequencies, and then superimposed to account all the pressures for each mode with the mean flow. The SPL directivity plot for the multi-frequency case containing all the three frequencies can be calculated for comparison. The directivity plotted in Fig. 4.8 for shows good agreement between these two cases. It shows that based on the axisymmetric mean flow and geometry, the total multi-frequency acoustic field is the same as the superposition of single frequency mode results.

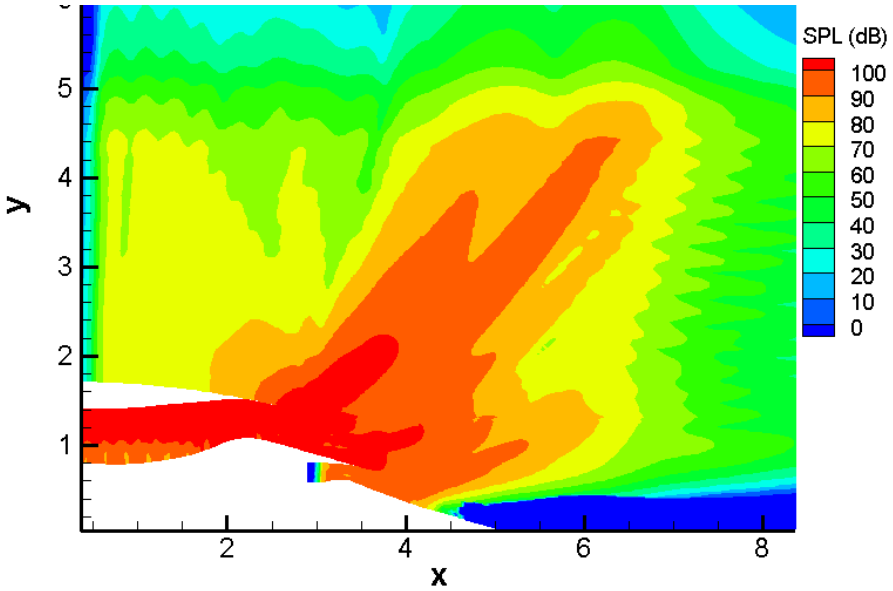

Figure 4.6: Near-field SPL for (12, 1) mode from summed three frequencies (1 kHz, 1.5 kHz, 2 kHz).

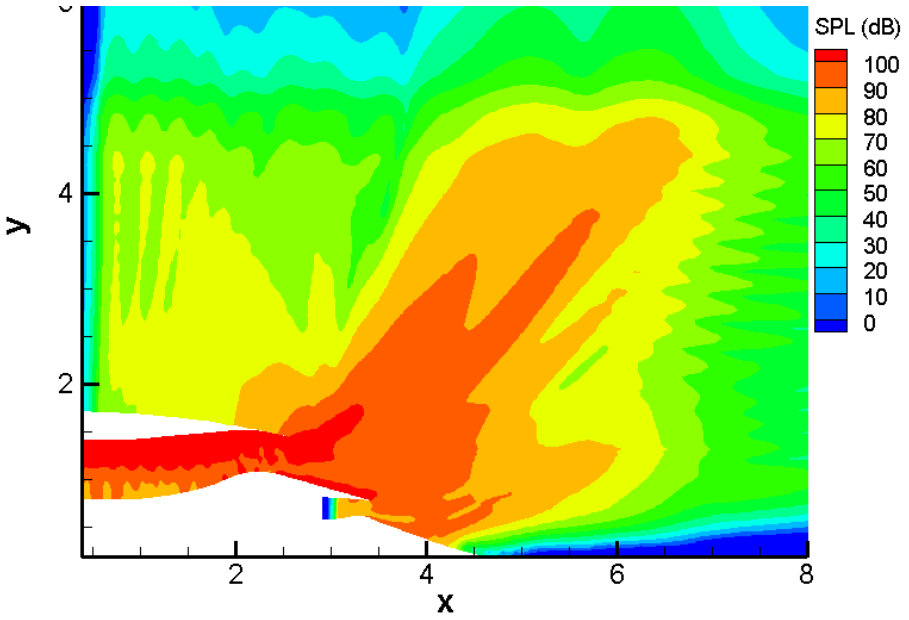

Figure 4.7: Near-field SPL prediction using multi-frequency sources (1 kHz, 1.5 kHz, 2 kHz):

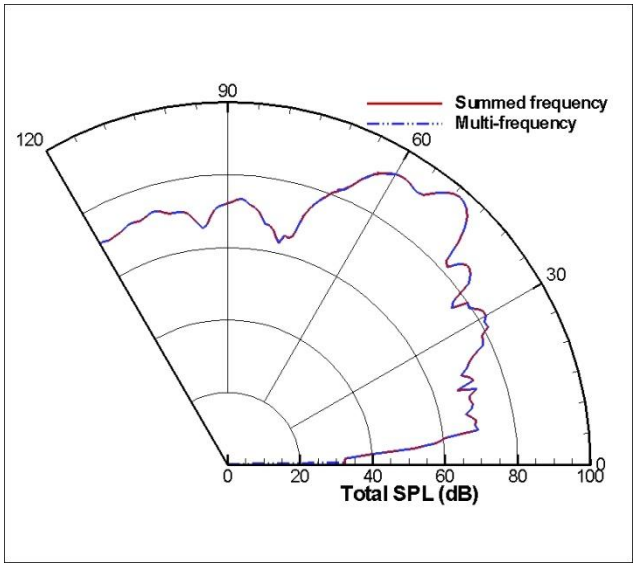

Figure 4.8: The near-field directivities comparisons at r=4.

The directivity pattern ranges along an arc where a polar observation angle is defined to be staring from the axisymmetric axis ($\phi = 0^{\circ}$) and rotating anti-clockwise to $\phi = 120^{\circ}$. In the near-field at $r = 4$, the pressure levels from both results reach the radiation peak at 47° and shows good qualitative and quantitative agreement.

4.2.1.2 Effect of Radial Mode

Fig. 4.9 shows the directivity patterns for the circumferential mode $m = 12$ as the radial mode(n) changes from 1 to 8 at frequencies from 1000Hz to 2000Hz with an interval of 500Hz in near-field (along the arc $r = 4$). It is shown that the lower radial modes contribute more significantly to the overall SPL values than the higher ones.

In Fig. 4.10, a directivity pattern comparison between the summed SPL of full cut-on modes (1 to 8) and the first half of the radial modes (1 to 4) is made. The results show near identical behaviour at observation angles less than $60°$, and a maximum difference of less than 0.3 dB at angles lager than $60°$. Hence, only the first half modes can be used to predict the total SPL more efficiently, saving computing effort (by up to 47% in this case).

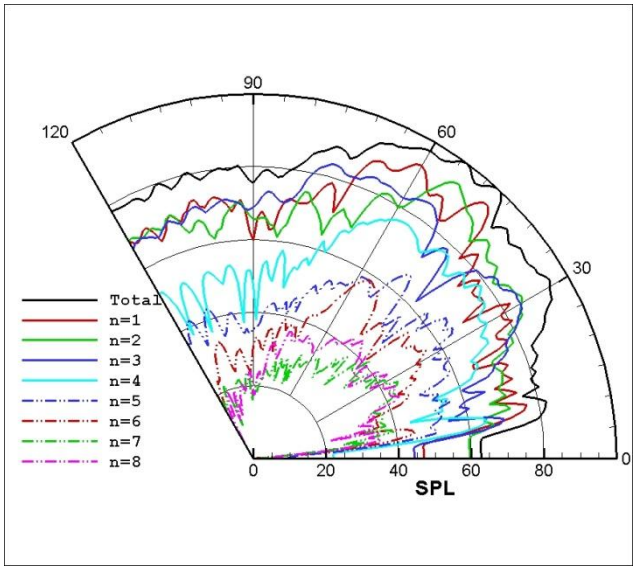

Figure 4.9: Directivity patterns at different radial modes in near-field.

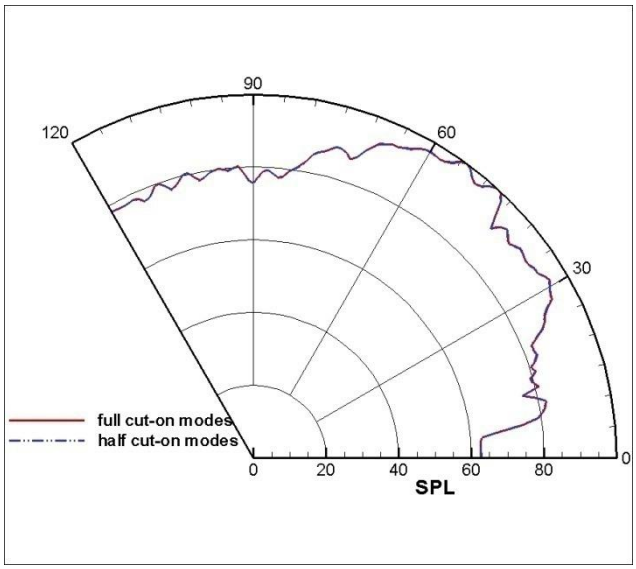

Figure 4.10: Directivity comparison of radial mode contribution for total SPL.

4.2.1.3 Effect of Circumferential Mode

Fig. 4.11 shows the directivity patterns at selected circumferential modes while keeping the radial mode as 1 at multi-frequency for 1000Hz, 1500Hz and 2000Hz along the arc of r=4. It indicates that the mode m=0 has an impact mainly on the first radiation peak. As the circumferential mode goes higher, the acoustic energy radiation peak angle increases. Based on the equal power assumption, one cut-on mode may have more weight than the others if the azimuthal mode appears on more

discrete frequencies. It can be concluded that lower circumferential modes are more likely cut-on to more discrete frequencies, and make more contributions to the total SPL.

Fig. 4.12 compares the superposed SPL directivity with 2/3 m modes (from 0 to 30 with an interval of 6) total SPL. At lower observation angles (under 25°) they are exactly the same; the maximum difference of -0.4dB happens at the observation angle of $30°$. Based on this finding, the computation could save more time if there is a need to calculate the total SPL precisely. The first 2/3 modes can be used to predict the total SPL more efficiently, saving much of the computing efforts (by up to 36% in this case).

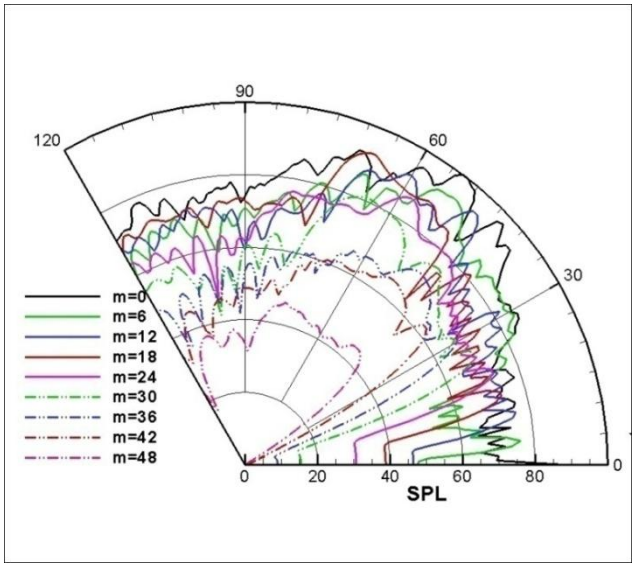

Figure 4.11: Directivity patterns at different circumferential modes in the near-field.

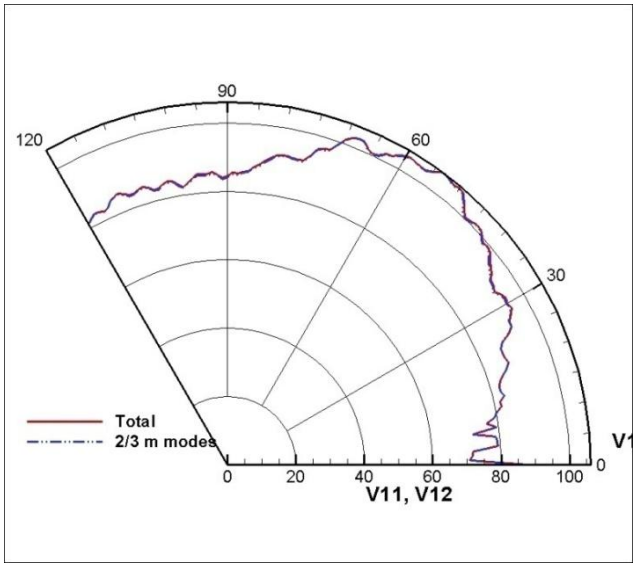

Figure 4.12: Directivity comparison of circumferential mode contribution for total SPL.

4.2.2 Bifurcation Configuration Effect

The 2.5D LEE/FW-H hybrid model has given an accurate and relatively efficient predictions for aeroacoustic spinning mode propagation and radiation from a clean engine bypass. The model is

based on the assumption of an axisymmetric mean flow and bypass geometry, and allows the propagation of single spinning modes, from which the total multi-mode acoustic field can be generated from the superposition of single mode results.

In general, realistic bypass flows and geometries are not axisymmetric and contain a multitude of spinning acoustic modes. For a general case, a prediction of the acoustic flow field can only be achieved from a solution of full 3D governing equations. In this section, a parallel 3D propagation solver that can be extended to arbitrary geometries and flow fields is used for mode propagation in a duct with a bifurcation.

The SotonCAA code verification at a frequency of 1547Hz for a single mode ($m = 12, n = 1$) has been done in comparison to reference [63] and the results outlining the contours of acoustic pressure contours show agreement. For the single mode case ($m = 12, n = 1$), a bifurcation plane at $\theta = 0^{\circ}$ and a middle plane $\theta = 45^{\circ}$ at frequency of 1000Hz along the circumferential direction are compared in Fig. 4.13. It can be seen that in both figures that the wave propagates out of the duct and diffracts around the duct lip. The main propagation direction is backward of the duct at a higher angle around 45° relative to the duct axis. At lower observation angles, acoustic modes are reflected from the edge of the bypass duct. The wave after the bifurcation arrived at the shear layer and then reflected to the computational domain. Due to the propagation of the sound waves, the strength of the acoustic pressures is increased on the downstream side of the bifurcation. The main radiation peak angles are almost the same for both cases. However, the bifurcation weakens the sound intensity.

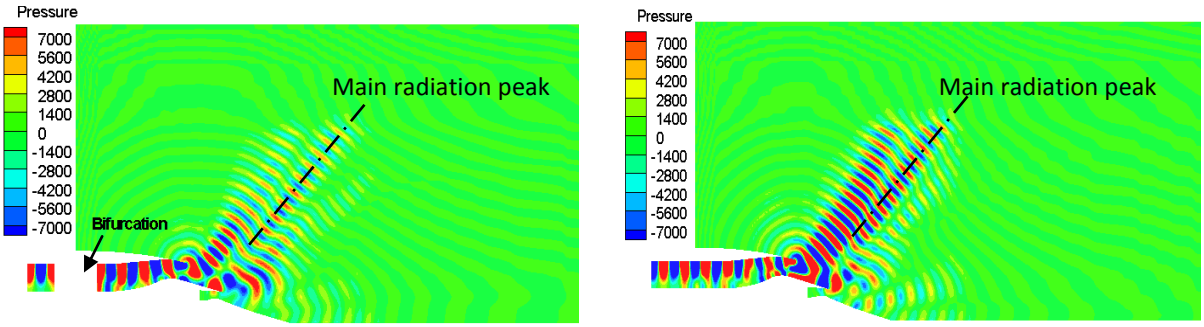

(a) (b)

Figure 4.13: Acoustic pressure patterns on 2D plane at (a) $\theta = 0^{\circ}$ (b) $\theta = 45^{\circ}$ at single mode case.

Figs. 4.14 and 4.15 show the effect of a bifurcation on the acoustic pressure distribution. Fig 4.14 is the acoustic pressure pattern of the nozzle in 3D. Fig. 4.15 shows the outer face of the nozzle. It can be seen clearly that the pressure redirects after the bifurcation section due to the distortion by the bifurcation. The circumferentially moving mode is diffracted by the bifurcation, leading to stronger acoustic pressures when the diffracted modes interfere with each other.

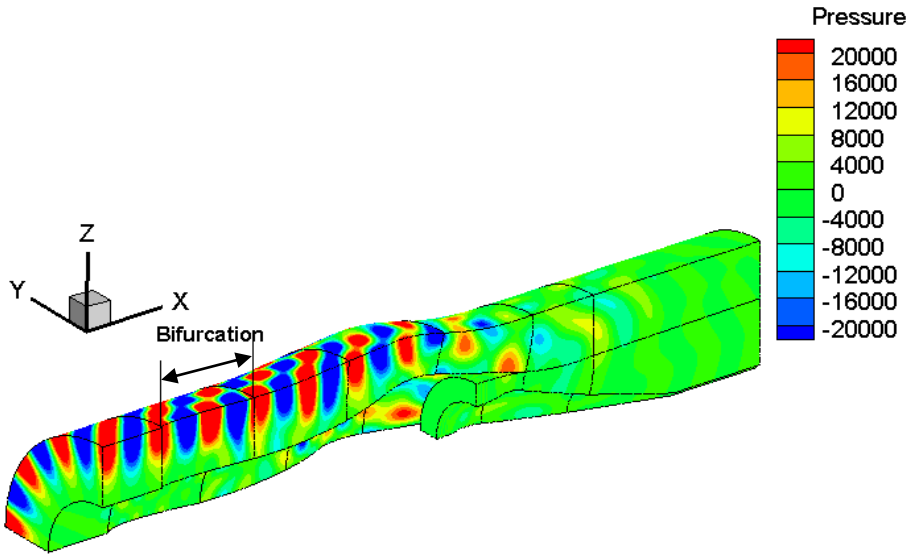

Figure 4.14: Acoustic pressures on a cross-section of the bifurcation case.

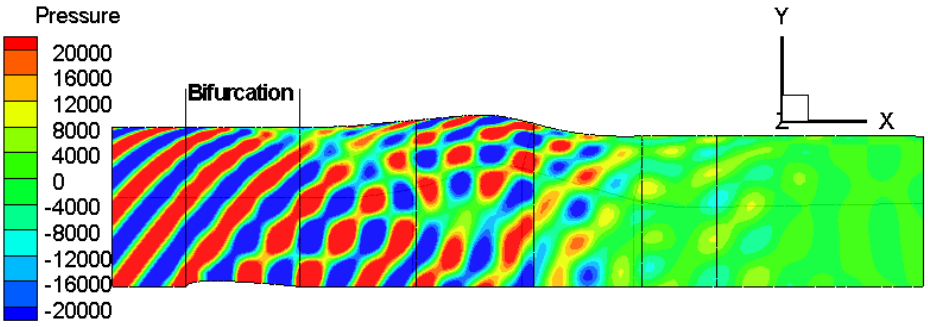

Figure 4.15: Acoustic pressure on a cross –section of outer face.

Fig. 4.16 shows the acoustic pressure patterns on a y-z plane (shown in Fig 4.2) at x=4, which is after the bifurcation. It is shown clearly that the bifurcations distort the acoustic pressure distribution.

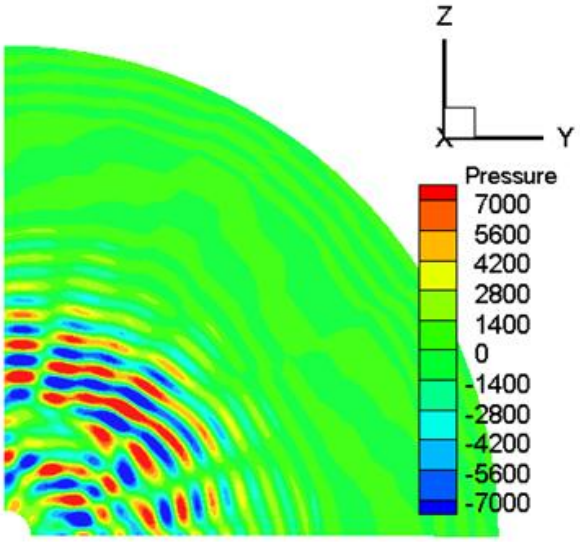

Figure 4.16: Acoustic pressure patterns on y-z plane at x=4 for bifurcation case (single mode).

Fig. 4.17 shows the sound pressure level (SPL) directivity on a 2D plane at bifurcations at $\theta = 0^{\circ}$ and a middle plane $\theta = 45^{\circ}$ respectively and along the integration surface at $r = 4$. The results suggest that the bifurcation could redirect the sound propagation from the duct. Both SPLs reach the peak at the observation angle of 49°. The directivity patterns are slightly different between the two planes. They indicate that the noise is decreased at different azimuthal planes and is increased at other angles. The SPL in the range of $30° < \theta > 75°$ shows lower levels and higher levels towards $\theta = 45°$.

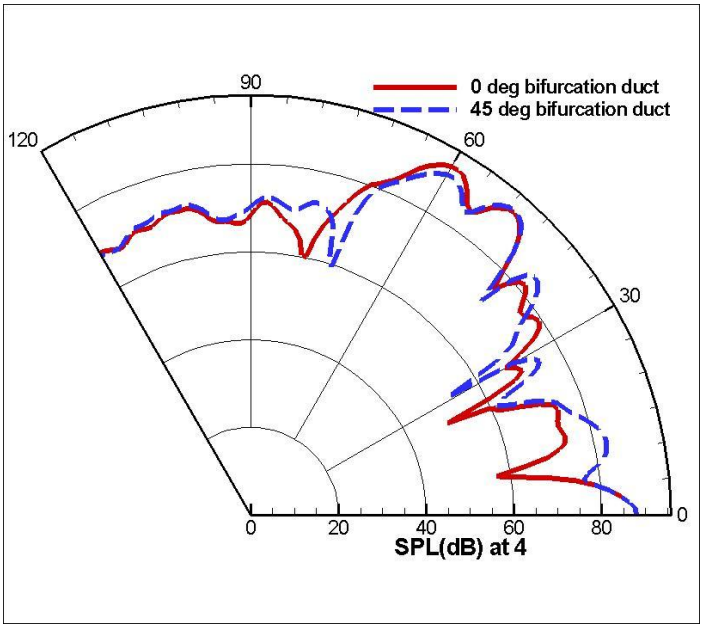

Figure 4.17: The near-field directivity along the arc of $r = 4$ in different φ angel planes.

4.2.3 Comparison of Multi-frequency Computation

Three discrete frequencies ranging from 1000 to 2000 Hz with an interval of 500Hz have been tested separately. The superposition result, shown in Fig. 4.19, is compared with that (see Fig. 4.18) predicted using these three frequencies in a single computation. The directivity pattern comparison is shown in Fig. 4.20. The reflective wave in the azimuthal direction may be discontinuous. It can be seen that the results compare well both qualitatively and quantitatively.

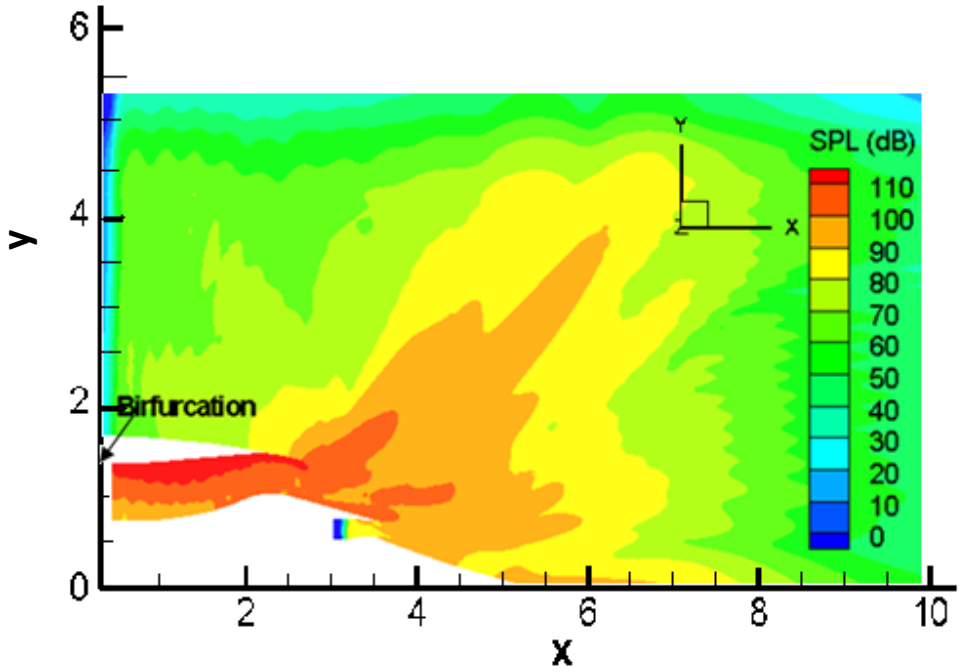

Figure 4.18: 3D near-field SPL prediction by multi-frequency sources on a 2D plane.

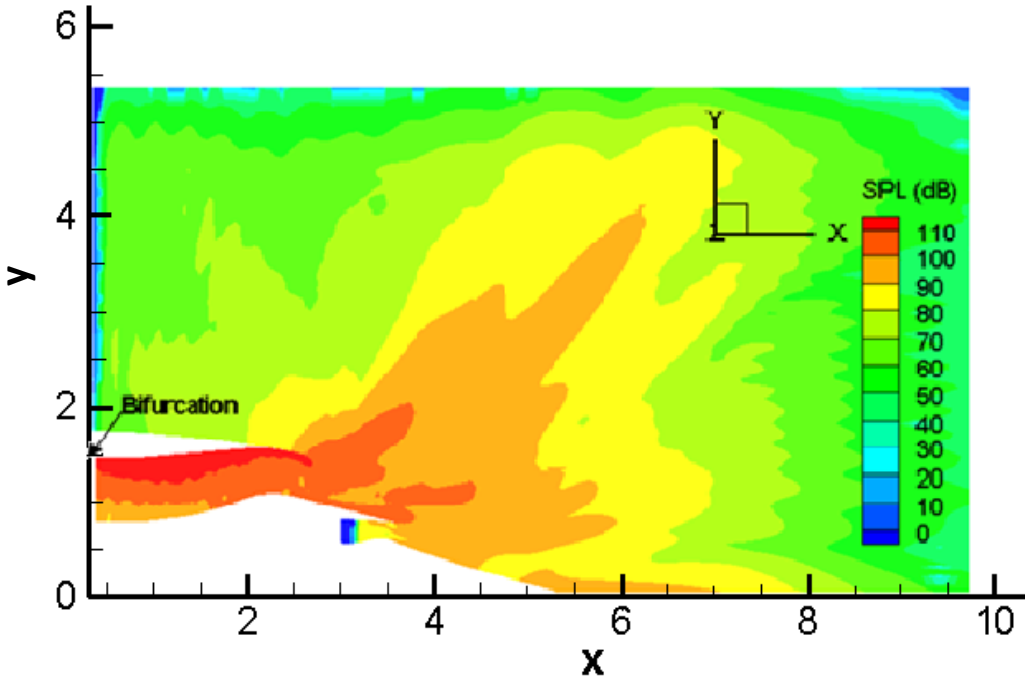

Figure 4.19: 3D near-field SPL prediction by summed single frequency source on a 2D plane.

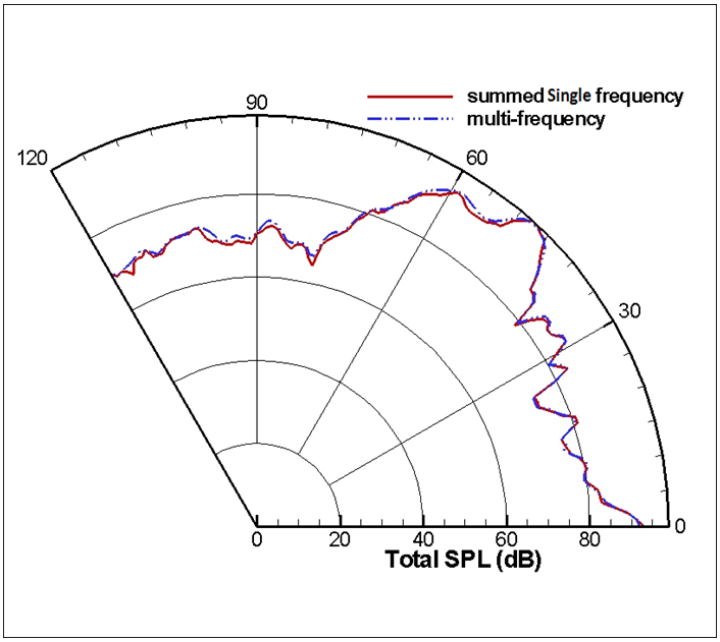

Figure 4.20: Comparison of directivity along the arc of $r = 4$.

Fig. 4.20 shows the comparison of directivity along the arc of $r = 4$, where the centre is taken at (x,y)=(2.5, 0.0). The near-field directivity patterns at the azimuthal planes are similar in terms of the amplitude and predicted angle for the radiation peaks. The SPL reaches its peak at around $47°$, and then drops by 30 dB at the observation angle of 120°.

The existing problem for the FW-H solver to predict the far-field case is that the computing storage limits the prediction of multi-mode source radiation. Developing the AIBM could solve the problem since it only requires the pressure histories along the integration surface for multi-mode sources. The directivity has been done in the near-field for comparison as the AIBM has not been applied to the multi-mode sources.

The results illustrate that the SPL are uncorrelated at different frequencies. The characters are independent of frequency. This allows many calculations to be combined together in a single computation to save a good deal of computing cost. Alternatively the calculations could be isolated if single frequency is needed.

4.2.4 Radial Mode Effect

In this section we want to explore the role of the radial mode by changing the radial (n) mode number. The radial modes change from $n = 1$ to 3 while keeping the circumferential mode as m =12 at a frequency of 1000Hz, by setting the amplitude equal to 1 for comparison against a single mode. The acoustic pressure contours on 2D planes are shown in Fig. 4.21. It can be seen that the strength of the pressure appears stronger after the bifurcation section. The higher order n-modes get more pressure diffraction by the end of the lip of the duct. The pressure also appears stronger after the core nozzle. It is noticed that the strength increases at the lower n modes at the core nozzle area, but the pressure propagates stronger in further field at the higher n modes. It may be that the radial energy has smaller amplitude at lower radial mode orders while it becomes more distinct at higher radial orders as the higher n modes lead the cut-on ratio to one.

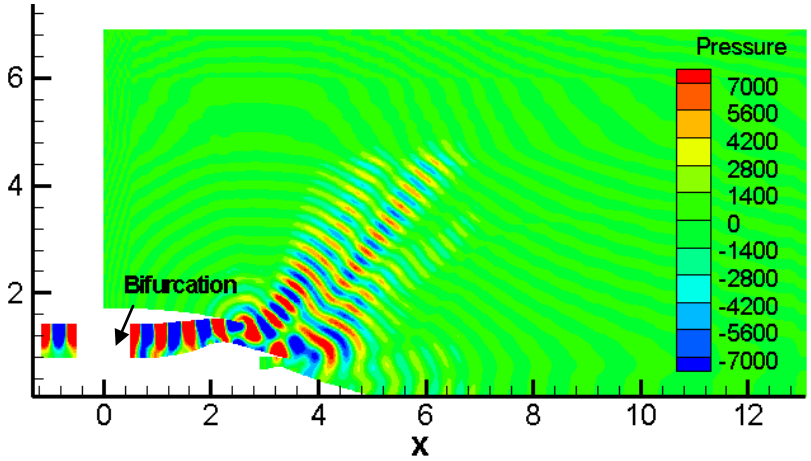

(a)

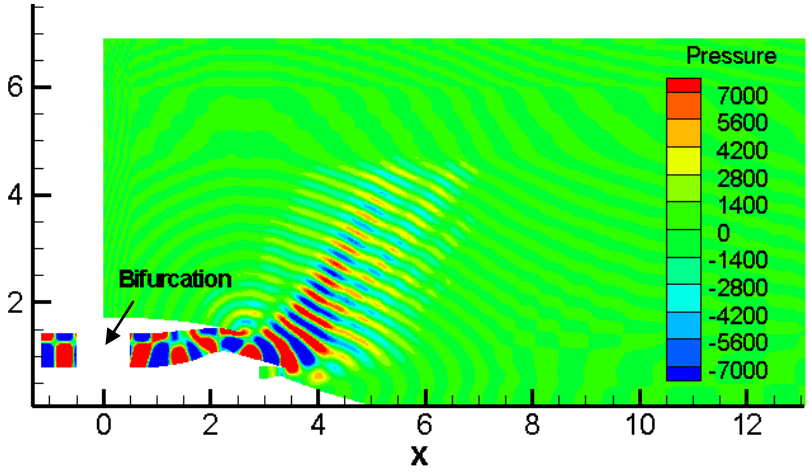

(b)

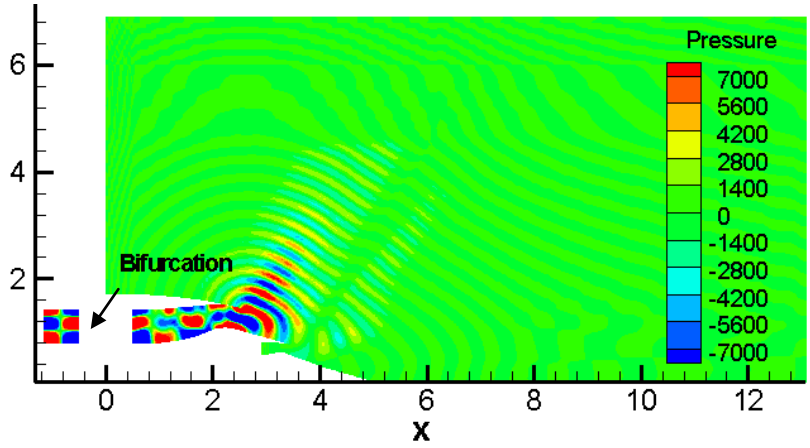

(c)

Figure 4.21: Acoustic pressure contours of 2D plane at $\theta = 0$ for different radial mode.(a) n=1, (b) n=2,(c) n=3.

As for the directivity, different radial mode directivity patterns are shown in Fig. 4.22. It shows that although the amplitudes are different, the main radiation peak angles for the three radial modes are almost the same. The SPL values are higher as the radial mode is lower. It reaches the peak around

the angles of 48° and 55°.

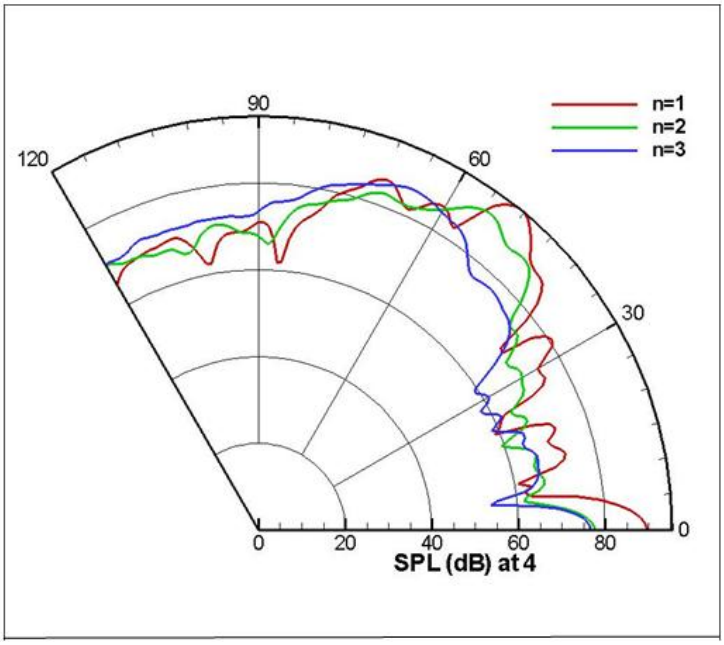

Figure 4.22: Directivities for different radial modes in the near-field.

Fig. 4.23 presents the multi-n mode, combining n from 1 to 3 at the bifurcation plane ($\theta = 0^{\circ}$) and middle plane ($\theta = 45^{\circ}$) while keeping the circumferential mode m= 12. It is noticed that the acoustic pressure is stronger after the bifurcation. The pressure also appears over the lip of the core nozzle in the middle plane. The reflections from the edge after the bifurcation along the duct lead to a stronger radiation pattern at lower radiation angles. It can be seen that a more complex pattern has formed in the nozzle after the bifurcation due to the interference by the bifurcation.

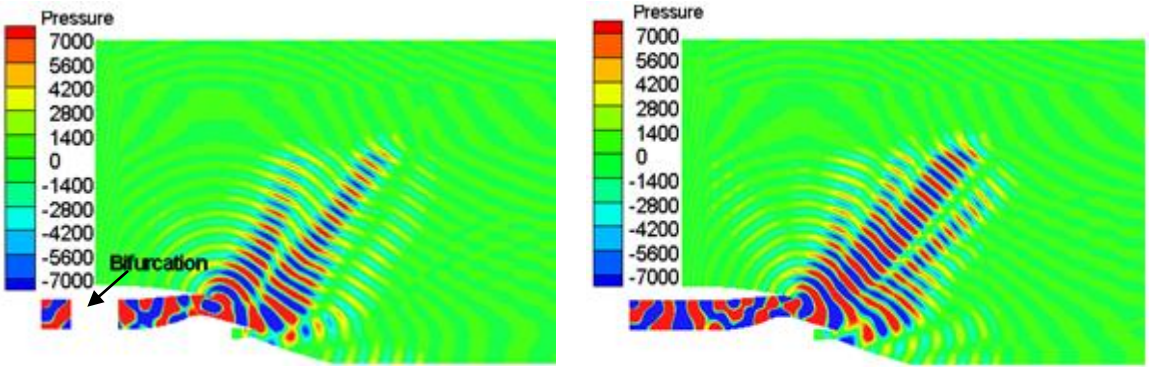

(a) (b)

Figure 4.23: Acoustic pressure contours of 2D planes at (a) $\theta = 0^{\circ}$, (b) $\theta = 45^{\circ}$.

Fig. 4.24 shows the acoustic pressure contours on a cross-section at x=4. It can be seen clearly that the bifurcation distorts the multi-n mode acoustic pattern. Compared with the single mode shown in Fig. 4.15, it can be concluded that the multi-n mode case was more affected by the bifurcation than the single-n mode case.

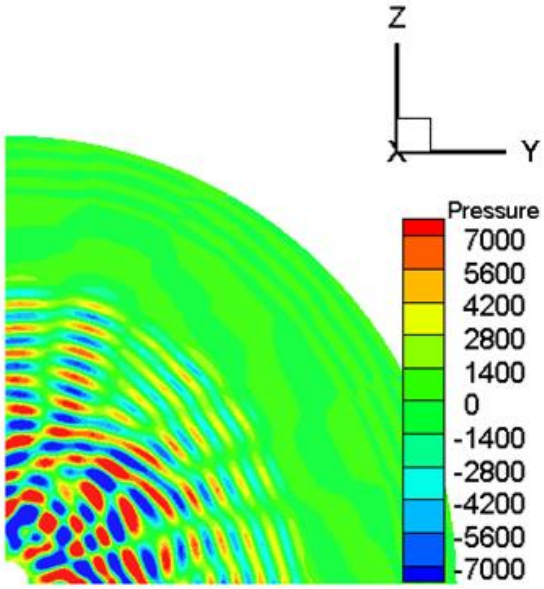

Figure 4.24: Acoustic pressure patterns on a 2D plane at x=4.

4.2.5 Circumferential Mode Case

In this study the effect of circumferential modes is studied for m values from 6 to 15 with an interval of 3 while the radial mode is kept at 1 at a frequency of 1000Hz. Fig. 4.25 that as the circumferential mode goes higher, the strength of the acoustic pressure is weaker. Fig. 4.26 shows the directivity for SPL in near-field along the arc $r = 4$, and indicates more clearly that the circumferential modes have effect on the main radiation peak angle. The radiation peak angle increases as the circumferential mode goes higher along the x axis. The main radiation peak angles are $32°, 47°, 51°$ and $59°$ respectively for circumferential modes (m) of 6,9,12 and 15. This is mainly because as the m modes increase, according to Eq. (2.54) the cut-on ratio is lower. Also, the radiation peak angle increases as the cut-on ratio is lowered to 1.

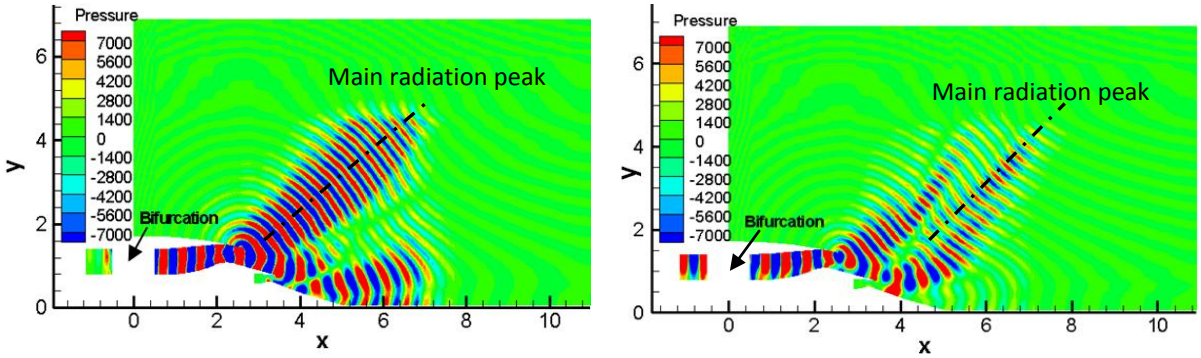

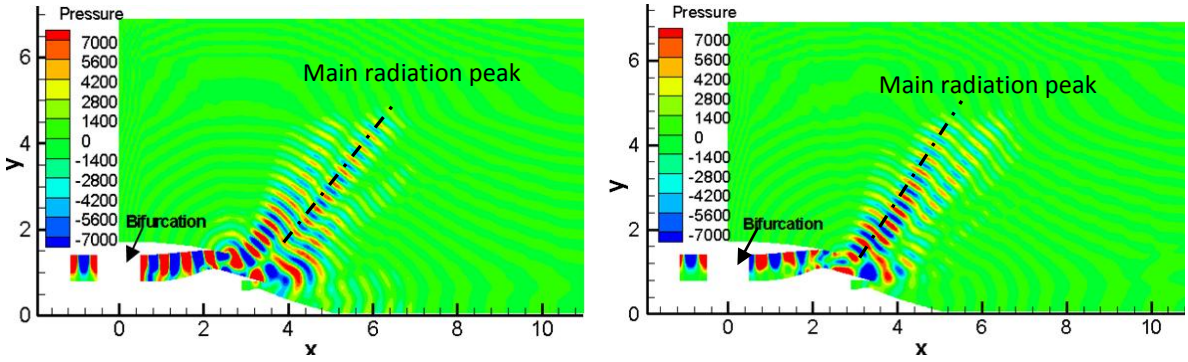

(c) (d)

Figure 4.25: Pressure contours for different circumferential mode on 2D plane. (a) m=6; (b) m=9; (c) m =12; (d) m =15.

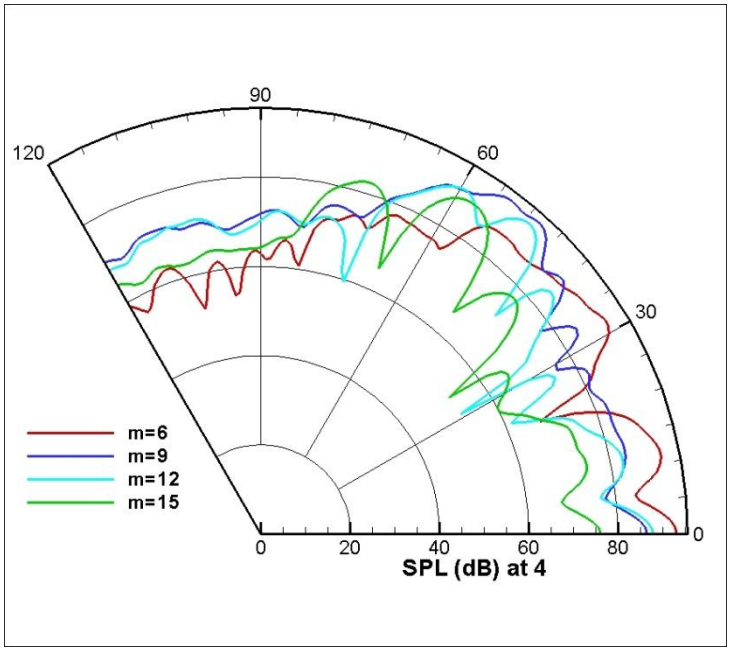

Figure 4.26: SPL for different circumferential modes in the near-field.

5 Conclusion Remarks and Future Work

A summary discussion of the main conclusions of the work and suggestions for future research are presented below.

5.1 Concluding Remarks

The aim of this work was to study the methods for prediction of multi-mode propagation and radiation from an engine bypass duct with and without an installed bifurcation.

In the first part of this work, a set of linearised Euler equations are introduced, which are the main governing equations for the multi-mode acoustic propagation and radiation prediction in the near-field. A 2.5D formulation of the LEE could be used to calculate the efficient propagation of different spiral modes in a 2D computational domain. The 3D equations including complex terms allow acoustic propagation from engine ducts with an arbitrary geometry. The SotonCAA code has been tested against some benchmark cases, such as scattering cases, combining with the FW-H solver to predict the far-field acoustic pressures for non-periodic cases.

In the second part of the thesis, a numerical method called AIBM was studied. Due to its demanding requirement for computational resources, the existing FW-H solver cannot be used for far-field multi-mode acoustic radiation prediction. However AIBM is an efficient tool to predict the far-field acoustic pressures for both the single and multi-mode cases combined with the near-field solution, which only uses a single variable of pressure and does not require a closed surface. A benchmark case of acoustic radiation from multi sound-sources has been validated to prove the reliability of this method and was followed by a bypass duct mode propagation case for verification. Using the pressure values on an integration surface computed by the LEE in the near-field as the input data, the AIBM solver could predict the far-field acoustic pressures. The directivity is compared with the results computed by the FW-H solver for a single mode case and it showed that the main radiation peaks were predicted well. The AIBM method saves up to 67% memory in comparison with FW-H method for the present bypass duct case.

In the third part of the thesis, the validated SotonCAA code using the LEE solver was applied to a generic engine bypass duct case with bifurcations installed for a multi-mode acoustic propagation and radiation problems in the near-field. Firstly, the clean duct cases were used as a baseline using the 2.5D LEE solver to analyse the effects of multi-frequency and different modes in both circumferential and radial directions in a 2D computational domain. Using a mode decomposition and wave-splitting technique, the SPL directivity predictions for the superpositioned of individual frequencies and the multi-frequency cases were shown to be almost identical. The 2D analysis highlighted the effect of multi radial and circumferential modes. The lower radial modes contribute more to the overall SPL value than the higher modes, while the lower circumferential modes are more likely to cut-on to more discrete frequencies, contributing more effect to the overall SPL values. Secondly, the improved 3D LEE solver is employed for more general duct cases with bifurcations associated with mean flow. A multi-processor capability was used in order for 3D simulations to be performed more efficiently. The 3D model allows the acoustic propagation, from engine bypass ducts, of multi-frequency. The acoustic propagation in the near-field was solved using the high-order numerical schemes which can achieve accurate solutions with reduced computational storage

requirement. Comparison of near-field directivities of the spinning and axisymmetric modes predicted by the LEE were in good agreement with multi-frequency and frequencies in superposition. The work confirmed that the bifurcation has influences on the near-field acoustic pressure field compared to the axisymmetric duct cases. The effects of the bifurcations on the spinning mode radiation from a bypass duct in the radial and circumferential directions were studied and analysed. For different radial modes, the lower ones are less centralised at the lip of the duct, and the predicted pressure is weaker after the nozzle area. However, for different radial modes of 1, 2 and 3, the radiation peak is almost same. Due to the bifurcation distortion, a more complex pattern is formed in the nozzle area for the multi radial mode cases. For different circumferential mode cases, the radiation peak angle increases along the duct axis as the circumferential mode goes higher.

5.2 Future Work

The current SotonCAA code, including the newly developed LEE solver which can be used in multi-mode acoustic problems, could be applicable to other configurations/problems with different bifurcations and modes. To make the AIBM code more robust, an area of immediate interest is the broadband noise prediction computation using the AIBM method. Further work could introduce acoustic liners at different positions in the duct with non-uniform mean flows to optimise the sound radiation and propagation performance.

Bibliography

[1] Arguelles, P. et al., 2001. Meeting Society's Needs and Winning Global Leadership. *European Aeroacoustics: A vision for 2020.* January 2001.

[2] Yu. C., Zhou, Z. and Zhuang, M., 2008. 3-D Acoustic Intensity-Based Method and Its CAA Applications. AIAA paper. 2008-3053.

[3] Yu, C., Zhou, Z. and Zhuang, M., 2008. An acoustic Intensity-Based Method for Reconstruction of Radiated Fields. *Acoustical Society of America.* 123, pp.1892-1901.

[4] Yu, C., Zhou, Z. and Zhuang, M., 2007. An Acoustic Intensity-Based Inverse Method for Sound Propagations in Uniform Flows. AIAA paper. 2007-3563.

[5] http://www.hasdeu.bz.edu.ro/softuri/fizica/mariana/

[6] P. di Francescantonio, A new boundary integral formulation for the prediction of sound radiation. *Journal of Sound and Vibration*, 202 4 (1997), pp. 491–509

[7] Lighthill, M.J., 1951. On Sound Generated Aerodynamically. *Proceedings of the Royal Society of London.* 211, pp.564-587.

[8] Curle, N., 1955. The Influence of Solid Boundaries upon Aerodynamic Sound. *Proceedings of the Royal Society*. 231, pp.505-514.

[9] FFowcs Williams, J.E. and Hawkings, D.L., 1969. Sound Generation by Turbulence and Surfaces in Arbitrary Motion. *The Royal Society*. 1969, pp. 321-342.

[10] Farassat, F., 1996. The Kirchhoff Formulas for Moving Surfaces in Aeroacoustics-The Subsonic and Supersonic Cases. *NASA Technical Memorandum 110285*.

[11] Singer, B. and Guo, Y.P., 2004. Development of Computational Aeroacoustics Tool for Airframe Noise Calculation. *International Journal of Computational Fluid Dynamics.* 18 (6), pp.455-469.

[12] Ewert, R. and Schröder, W., 2004. Acoustic Perturbation Equations Based on Flow Decomposition via Source Filtering. *Journal of Sound and Vibration.* 270, pp.590-524.

[13] Brentner, K.S. and Farassat, F., 1998. An Analytical Comparison of the Acoustic Analogy and Kirchhoff Formulation for Moving Surfaces. *AIAA Journal.* 36 (8), pp.1379-1386.

[14] Rizzetta, D.P., Visbal, M.R. and Blaisdell, G.A., 2003. A Time-implicit High-order Compact Differencing and Filtering Scheme for Large-eddy Simulation. *International Journal for Numerical Methods in Fluids*. 42, pp.665–693.

[15] Deck, S., 2005. Zonal-detached-eddy Simulation of The Flow around A High-lift Configuration. *AIAA Journal.* 43 (11), pp.2372-2383.

[16] Wang, M., Freund, J. B. and Lele, S.K., 2006. Computational Prediction of Flow Generated Sound. *Annual Review of Fluid Mechanics.* 38 , pp.483-512.

[17] Hedges, L.S., Travin, A.K. and Spalart, P.R., 2002. Detached-Eddy Simulations over a Simplified Landing Gear. *Fluid Engineering.* 124, pp.413-423.

[18] Spalart, P.R. and Allmaras, S., 1992. A One Equation Turbulence Model for Aerodynamic Flows. AIAA Paper. 92-0439.

[19] Fisher, M.J. and Self, R.H., 2001. Aeroacoustics Research in Europe: The CEAS-ASC Report on 2001 High-Lift. *Journal of Sound and Vibration.* 279, pp.419-459.

[20] Tam, C.K.W. and Webb, J.C., 1993. Dispersion Relation Preserving Finite Difference Schemes for Computational Acoustics. *Journal of Computational Physics.* 107, pp.262-281.

[21] Tam, C.K.W., 1998. Jet Noise: Since 1952. *Theory of Computational Fluid Dynamics.* 10, pp.393-405.

[22] Lele S.K., 1992. Compact Finite Difference Schemes with Spectral-like Resolution. *Journal of Computational Physics.* 103, pp.16-42.

[23] Hixon, R., 1998. A New Class of Compact Schemes. AIAA Paper. 1998-0736.

[24] Hixon, R., 2000. Prefactored Small-stencil Compact Schemes. *Journal of Computational Physics*. 165, pp.522-541.

[25] Ashcroft, G. and Zhang, X., 2003. Optimized Prefactored Compact Schemes. *Journal of Computational Physics.* 190, pp.459-477.

[26] Richards, S.K., Chen, X.X., Huang, X. and Zhang, X., 2007. Computation of Fan Noise through an Engine Exhaust Geometry with Flow. *International Journal of Aeroacoustics.* 6 (3), pp.223–241.

[27] Zhang, X and Chen, X.X., 2010. Time-Domain Computation of Multimode Propagation in an Aero-Engine Duct. *IUTAM Symposium on CAA for Aircraft Noise Prediction.* 6, pp.173-182.

[28] Hu, F.Q., Hussaini, M.Y. and Manthey, J., 1996. "Low Dissipation and Dispersion Runge-Kutta Schemes for Computational Acoustics. *Journal of Computational Physics.* 124, pp.177-191

[29] Visbal, M.R. and Gaitonde, D.V., 1999. High-Order-Accurate Methods for Complex Unsteady Subsonic Flows. *AIAA Journal.* 37 (10), pp.1231-1239.

[30] Pointwise, http://www.pointwise.com.

[31] Myers, M.K., 1980. On the Acoustic Boundary Condition in the Presence of Flow. *Journal of Sound Vibration.* 71, pp.429–434.

[32] Li, X.D., Richter, C. and Thiele, F., 2006. Time-Domain Impedance Boundary Conditions for Subsonic Mean Flow. *Journal of the Acoustical Society of America.* 119 (5), pp.2665– 2676.

[33] Richter, C., et al., 2006. Comparison of Time Domain Impedance Boundary Conditions for Lined Duct Flows. AIAA Paper. 2006-2527.

[34] Özyörük, Y. and Long, L.N., 1997. A Time-Domain Implementation of Surface Acoustic Impedance Conditions With and Without Flow. *Journal of Computational Physics.* 5, pp.277–296.

[35] Fung, K.Y. and Ju, H., 2004. Time Domain Impedance Boundary Conditions for Computational Acoustics and Aero-acoustics. *International Journal of Computational Fluid Dynamics.* 18 (6), pp.503–511.

[36] Rienstra, S.W., 2006. Impedance Models in Time Domain, Including the Extended Helmholtz Resonator Model. AIAA Paper. 2006-2686.

[37] Bin, J., Hussiani, M.Y. and Lee, S., 2009. Broadband Impedance Boundary Conditions for the Simulation of Sound Propagation in the Time Domain. *Journal of the Acoustical Society of America.* 125 (2), pp.664-675.

[38] Rienstra, S.W., 2006. Impedance Models in Time Domain Including the Extended Helmholtz Resonator Model. AIAA paper. 2006–2686.

[39] Tam, C.K.W. and Auriault, L., 1996. Time-Domain Impedance Boundary Conditions for Computational Aeroacoustics. *AIAA Journal.* 34 (5), pp.917–923.

[40] Astley, R.J., Sugimoto, R., Achunche, I.M., Kewin, M.F., Mustafi, P. and Deane, E.P., 2010. A Review of CAA for Fan Duct Propagation and Radiation, With Application to Liner Optimisation. *Procedia Engineering*. 6, pp.143-152.

[41] Farassat, F., 1981. Linear Acoustic Formulas for the Calculation of Rotating Blade Noise. *AIAA Journal*. 19, pp.1122-1130.

[42] Lowson, M. V., Whatmore, A.R. and Whitfield C.E., 1973. Source Mechanisms for Rotor Noise Radiation. *NASA.* CR-2007.

[43] Atassi, O. and Gilson, J.J., 2010. Future Challenges in Computational Aeroacoustics for Fan Broadband and Combustor Noise. *Procedia Engineering.* 6, pp.193-202.

[44] Delnevo, A., Saint, S.L., Sylvand, G. and Terrass, I., 2005. Numerical Methods: Fast Multiple Method for Shielding Effects. AIAA Paper. 2005–2971.

[45] Alleon, G., Champagneux, S., Chevalier, G., Giraud, L. and Sylvand, G., 2005. Parallel Distributed Numerical Simulations in Aeronautic Applications, *Applied Mathematical Modeling.* 30, pp.714–730.

[46] Lan, J.H., 2001. Turbofan Duct Propagation Model. *Technical Report, NASA*. CR-2001-211245.

[47] Nark, D.M. and Farassat, F., 2006. CDUCT-LaRC Status - Shear Layer Refraction and Noise Radiation. AIAA Paper. 2006–2587.

[48] Van Antwerpen, B., Leneveu, R. and Caro, S., 2008. New Advances in The Use of ACTRAN/TM for Nacelle Simulations. AIAA Paper. 2008–2827.

[49] Gabard, G., Astley, R.J. and Ben Tahar, M., 2005. Stability and Accuracy of Finite Element Methods for Flow Acoustics: I. General Theory and Application to One-Dimensional Propagation. *International Journal of Numerical Mathematics and Engineering.* 63, pp.947–973.

[50] Eversman, W. and Obuknor, D., 1998. Aircraft fan Duct Radiation. *Journal of Sound and Vibration.* 213, pp.235–257.

[51] MUMPS: A Multifrontal Massively Parallel Sparse Direct Solver, http://graal.ens-lyon.fr/MUMPS.

[52] Schonwald, N., Panek, L., Richter, C. and Thiele, F., 2007. Investigation of Sound Radiation from a Scarfed Intake by CAA-FWH Simulations Using Overset Grids. AIAA Paper. 2007–3524.

[53] Bassi, F. and Rebay, S., 1997. High Order Accurate Discontinuous Finite Element Solution of the 2d Euler Equations. *Journal of Computational Physics.* 138, pp.251–285.

[54] Atkins, H.L. and Shu, C.W., 1998. Quadrature Free Implementation of Discontinuous Galerkin Method for Hyperbolic Equations. *AIAA Journal.* 36 (5), pp.775–782.

[55] Stanescu, D., Hussaini, M.Y. and Farassat. F., 2002. Aircraft Engine Noise Scattering - A Discontinuous Spectral Element Approach. AIAA Paper. 2002–0800.

[56] Rao, P.P. and Morrist, P.J., 2003. Application of a Generalized Quadrature Free Discontinuous Galerkin Method in Aeroacoustics. AIAA Paper. 2003–3120.

[57] Redonnet, S., Mincu, C. and Manoha, E., 2008. Computational Aeroacoustics of Realistic Co-axial Engines. AIAA Paper. 2008–2826.

[58] Gamallo, P. and Astley, R.J., 2006. The Partition of Unity Finite Element Method for Short Wave Acoustic Propagation on Non-uniform Potential Flows. *International Journal of Numerical Mathematics and Engineering.* 65, pp.425–444.

[59] Dowling, A.P. and Ffowcs Williams, J.E., *Sound and Sources of Sound.* Ellis Horwood, pp.130-131.

[60] Thomas, R.H., Choudhari, M.M. and Joslin, R.D., 2002. Flow and Noise Control: Review and Assessment of Future Directions. *NASA*. TM-2002-211631.

[61] Tam, C.K.W. and Kurbatskii, K.A., 2000. Microfluid Dynamics and Acoustics of Resonant Liners. *AIAA Journal*. 38 (8), pp.1331-1339.

[62] Tam, C, K.W. and Hardin, J.C., 1997. Second Computational Aeroacoustics(CAA) Workshop on Benchmark Problems. *NASA Conference publications.* June 1997.

[63] Chen, X., Huang, X. and Zhang, X., 2009. Sound Radiation from a Bypass Duct with Bifurcations. *AIAA Journal.* 47 (2), pp.429-436.

[64] Kennedy, C.A. and Carpenter, M.H., 1997. Comparison of Several Numerical Methods for Simulation of Compressible Shear Layer. *NASA Technical Paper* 3484.

[65] Huang, X., Chen, X., Ma, Z. and Zhang, X., 2008. Efficient Computation of Spinning Modal Radiation Through An Engine Bypass Duct. *AIAA Journal.* 46 (6), pp.1414-1423.

[66] Zhang, X., Chen, X.X. and Morfey, C.L., 2005. Acoustic Radiation from a Semi-Infinite Duct with a Subsonic Jet. *International Journal of Aeroacoustics.* 4, pp.169–184.

Appendix

A. TDIBC Derivation

1. Single Frequency Formulation

As is assumed in Eq. (2.62), $Z = R_0 + i\omega X_1 - \frac{X_{-1}}{i\omega}$, $\widehat{W}$ has the simple poles:

$$\begin{gathered}\omega_{1,2} = \pm\omega_R + i\omega_I \\ \omega_R = \sqrt{\left(-\frac{X_{-1}}{X_1}\right) - \left[\frac{1+R_0}{2X_1}\right]^2}\,, \\ \omega_I = \frac{1+R_0}{2X_1}.\end{gathered} \tag{A1}$$

If $X_1 > 0$ and $X_{-1} < 0$, this implies that $W(t)$ is causal, so $W(t)$has the form:

$$W(t) = \left[\frac{2H(t)}{X_1}\right]\left[\cos\omega_R t - \left(\frac{\omega_I}{\omega_R}\right)\sin(\omega_R t)\right]e^{-\omega_I t} - \delta(t). \tag{A2}$$

$W(t)$ can be written as:

$$W(t) = \widetilde{W}(t)H(t) - \delta(t) \tag{A3}$$

where

$$\widetilde{W}(t) = \left[\frac{2}{X_1}\right]\left[\cos\omega_R t - \left(\frac{\omega_I}{\omega_R}\right)\sin(\omega_R t)\right]e^{-\omega_I t}. \tag{A4}$$

Then Eq. (2.67) could be written as

$$u^-(t) = -u^+(t) + \int_{-\infty}^{t} H(t-\tau)\widetilde{W}(t-\tau)\,u^+(\tau)d\tau. \tag{A5}$$

Using a trapezoidal integration, Eq. (A5) has following form:

$$u^-(t) = -u^+(t) + \frac{1}{2}\Delta t\widetilde{W}(0)u^+(t) + \Delta t\sum_{k=1}^{N}\widetilde{W}(k\Delta t)u^+(t-k\Delta t). \tag{A6}$$

Another efficient integration method can also be derived. Eq. (A4) can be rewritten as:

$$\widetilde{W}(t) = \frac{1}{X_1\omega_R}\left(\omega_1 e^{i\omega_1 t} - \omega_2 e^{i\omega_2 t}\right) = \mu_1 e^{i\omega_1 t} + \mu_2 e^{i\omega_2 t},$$

$$\omega_1 = \omega_R + i\omega_I,\ \omega_2 = -\omega_R + i\omega_I. \tag{A7}$$

Then Eq. (A5) becomes:

$$
\begin{aligned}
u^-(t) &= -u^+(t) + \int_0^\infty \widetilde{W}(\tau)u^+(t-\tau)d\tau \\
&= -u^+(t) + \int_0^{\Delta t} \widetilde{W}(\tau)u^+(t-\tau)d\tau + \int_{\Delta t}^\infty \widetilde{W}(\tau)u^+(t-\tau)d\tau \\
&= -u^+(t) + \int_0^{\Delta t} \widetilde{W}(\tau)u^+(t-\tau)d\tau + \int_0^\infty \widetilde{W}(\tau+t)u^+(t-\Delta t-\tau)d\tau \\
&\approx -u^+(t) + \frac{1}{2}\Delta t[\widetilde{W}(0)u^+(t) + \widetilde{W}(\Delta t)u^+(t-\Delta t) \\
&\quad + \int_0^\infty \widetilde{W}(\tau+t)u^+(t-\Delta t-\tau)d\tau. \qquad (A8)
\end{aligned}
$$

Let

$$
\int_0^\infty \widetilde{W}(\tau+t)u^+(t-\Delta t-\tau)d\tau = I_1(t) + I_2(t) \qquad (A9)
$$

where

$$
\begin{aligned}
I_1(t) &= \mu_1 \int_0^\infty e^{i\omega_1\tau}u^+(t-\tau)d\tau \\
&= \mu_1 \int_0^{\Delta t} e^{i\omega_1\tau}u^+(t-\tau)d\tau + \mu_1 \int_{\Delta t}^\infty e^{i\omega_1\tau}u^+(t-\tau)d\tau \\
&= \mu_1 \int_0^{\Delta t} e^{i\omega_1\tau}u^+(t-\tau)d\tau + \mu_1 \int_0^\infty e^{i\omega_1(\tau'+\Delta t)}u^+(t-\Delta t-\tau')d\tau' \\
&= \mu_1 \frac{1}{2}\Delta t\left[u^+(t) + e^{i\omega_1\Delta t}u^+(t-\Delta t)\right] + e^{i\omega_1\Delta t}I_1(t-\Delta t). \qquad (A10)
\end{aligned}
$$

The same procedure will also produce:

$$
I_2(t) = \mu_2 \frac{1}{2}\Delta t\left[u^+(t) + e^{i\omega_2\Delta t}u^+(t-\Delta t)\right] + e^{i\omega_2\Delta t}I_2(t-\Delta t). \qquad (A11)
$$

The initial conditions are:

$$
\begin{aligned}
I_1(0) = I_2(0) &= 0 \\
u^+(0) &= u(0) + p(0) \\
u^+(n\times\Delta t) &= u^+((n-1)\times\Delta t)
\end{aligned}
$$

2. Broadband Formulation

Starting from Eq. (4.59):

$$\widehat{W}(\omega) = \widehat{\widehat{W}}(\omega) - 1 \tag{A12}$$

where

$$\widehat{\widehat{W}} = \frac{2}{1+Z} = \frac{2}{1+R(\omega^2)+i\omega X(\omega^2)} = \frac{Q(s)}{D(s)}. \tag{A13}$$

R and X are the resistance and reactance respectively and they are real. $s = i\omega$.

Assume $D(s)$ has the form as: $D(s) = (s-\lambda_1)(s-\lambda_2)(s-\lambda_3)\cdots(s-\lambda_m)$, and thus $\widehat{\widehat{W}}(\omega) = \sum_{k=1}^{m} \widehat{\widehat{W}}_k(\omega)$, with $\widehat{\widehat{W}}_k(\omega) = \frac{C_k}{s-\lambda_k}$. Because $D(s)$ has only real coefficients its zeros λ_k are either real or complex conjugate pairs. When one of the roots λ_k of $D(s)$ is complex, its conjugate λ_{k+1} must exist to form the pair. Thus $\widehat{\widehat{W}}_k(\omega)$ can be written as:

$$\widehat{\widehat{W}}(\omega) = \sum_{j=1}^{2L} \widehat{\widehat{W}}_j(\omega) = \sum_{k=1}^{l} \left[\widehat{\widehat{W}}_{2k-1}(\omega) + \widehat{\widehat{W}}_{2k}(\omega)\right] \tag{A14}$$

where

$$\begin{aligned}\widehat{\widehat{W}}_{2k-1}(\omega) + \widehat{\widehat{W}}_{2k}(\omega) &= \frac{C_{2k-1}}{s-\lambda_{2k-1}} + \frac{C_{2k}}{s-\lambda_{2k}} = \frac{A_{2k-1}s + A_{2k}}{(s+\alpha_k)^2+\beta_k^2} \\ &= \frac{A_{2k-1}s + A_{2k}}{(s+\bar{\alpha}\omega_{0k})^2 + \omega_{0k}^2(1-\bar{\alpha}^2)}\end{aligned} \tag{A15}$$

and

$$\lambda_{2k-1} = \alpha_k + i\beta_k,$$

$$\lambda_{2k} = \alpha_k - i\beta_k,$$

$$\alpha_k = \bar{\alpha}\omega_{0k}, \beta_k = \omega_{0k}\sqrt{(1-\bar{\alpha}^2)}.$$

ω_{0k} is the frequency used in the experiments and the coefficients, A_{2k-1}, A_{2k} and the damping coefficient $\bar{\alpha}$ are fitted to a set of impedance tests. In practice, a set of Z_j are known at discrete frequencies ω_j and so with specified A_{2k-1}, A_{2k} the damping coefficient $\bar{\alpha}$ can be determined.

$\widehat{\widehat{W}}_j(\omega)$ can be written as:

$$\begin{aligned}\widehat{\widehat{W}}_j(\omega) &= \sum_{k=1}^{l} \frac{A_{2k-1}s + A_{2k}}{(s+\alpha_k)^2+\beta_k^2} \\ &= \sum_{k=1}^{l} \frac{iA_{2k-1}\omega_j + A_{2k}}{\alpha_k^2+\beta_k^2-\omega_j^2+i2\omega_j\alpha_k} \\ &= \sum_{k=1}^{l} \frac{\left(iA_{2k-1}\omega_j + A_{2k}\right)\left(\alpha_k^2+\beta_k^2-\omega_j^2-i2\omega_j\alpha_k\right)}{\left(\alpha_k^2+\beta_k^2-\omega_j^2\right)^2 + 4(\omega_j\alpha_k)^2},\end{aligned} \tag{A16}$$

thus,

$$\sum_{k=1}^{l} B_{r,2k-1}A_{2k-1} + B_{r,2k}A_{2k} = \frac{2\left(1+R_j\right)}{\left(1+R_j\right)^2 + X_j^2}$$

$$\sum_{k=1}^{l} B_{i,2k-1}A_{2k-1} + B_{i,2k}A_{2k} = \frac{-2X_j}{\left(1+R_j\right)^2 + X_j^2} \qquad (A17)$$

where coefficients are known as:

$$B_{r,2k-1} = 2\omega_j^2\alpha_k/F_k$$

$$B_{r,2k} = \left(\alpha_k^2 + \beta_k^2 - \omega_j^2\right)/F_k$$

$$B_{i,2k-1} = \left(\alpha_k^2 + \beta_k^2 - \omega_j^2\right)\omega_j/F_k$$

$$B_{r,2k} = -2\omega_j\alpha_k/F_k$$

$$F_k = \left(\alpha_k^2 + \beta_k^2 - \omega_j^2\right)^2 + 4(\omega_j\alpha_k)^2.$$

In practice, the number (L) of discrete functions $\widehat{\widehat{W}}_j$ is known. The 2L coefficients $A_1$to A_{2L} need to be calculated.

The time domain formula can be shown as:

$$W(t) = \begin{cases} i\sum_{k=1}^{L} \text{residue}\left[\widehat{W}(\omega), \omega_{2k-1}\right]e^{i\omega_{2k-1}t} + \text{residue}\left[\widehat{W}(\omega), \omega_{2k}\right]e^{i\omega_{2k}t} & t \geq 0 \\ 0 & t < 0 \end{cases} \qquad (A18)$$

From Eq. (A14), the poles of $\widehat{W}(\omega)$ is the sum of the poles $(A_{2k-1}s + A_{2k})/[(s+\alpha_k)^2 + \beta_k^2]$

That is:

$$\frac{i\omega A_{2k-1} + A_{2k}}{(i\omega + \alpha_k)^2 + \beta_k^2}$$

$$= \frac{1}{i}\frac{\omega A_{2k-1} - iA_{2k}}{(\omega - i\alpha_k)^2 - \beta_k^2}$$

$$= \frac{1}{i}\frac{\omega A_{2k-1} - iA_{2k}}{(\omega - \omega_{2k-1})(\omega - \omega_{2k})} \qquad (A19)$$

where

$$\omega_{2k-1} = i\alpha_k + \beta_k$$

$$\omega_{2k} = i\alpha_k - \beta_k$$

$$\omega_{2k-1} - \omega_{2k} = 2\beta_k.$$

Thus,

$$\text{residue}\left[\widehat{W}(\omega),\omega_{2k-1}\right]e^{i\omega_{2k-1}t}+\text{residue}\left[\widehat{W}(\omega),\omega_{2k}\right]e^{i\omega_{2k}t}$$

$$=H(t)e^{-\alpha_k t}\left[A_{2k-1}\cos(\beta_k t)+\frac{A_{2k}-\alpha_k A_{2k-1}}{\beta_k}\sin(\beta_k t)\right]. \qquad (A20)$$

Using the recursive formula:

$$\widetilde{W}_{(2k-1,2k)}(t)=H(t)\frac{\omega_{2k-1}A_{2k-1}-iA_{2k}}{\omega_{2k-1}-\omega_{2k}}e^{i\omega_{2k-1}t}+H(t)\frac{\omega_{2k}A_{2k-1}-iA_{2k}}{\omega_{2k}-\omega_{2k}}e^{i\omega_{2k}t}, \qquad (A21)$$

Eq. (A5) could be written as:

$$u^{-}(t)=-u^{+}(t)+\int_0^\infty \widetilde{W}(\tau)\,u^{+}(t-\tau)d\tau$$

$$=-u^{+}(t)+\sum_{k=1}^{L} I_{2k-1}(t)+I_{2k}(t) \qquad (A22)$$

where

$$I_{2k-1}=\mu_{2k-1}\frac{1}{2}\Delta t\left[u^{+}(t)+e^{i\omega_{2k-1}\Delta t}u^{+}(t-\Delta t)\right]+e^{i\omega_{2k-1}\Delta t}I_{2k-1}(t-\Delta t) \qquad (A23)$$

$$I_{2k}=\mu_{2k}\frac{1}{2}\Delta t\left[u^{+}(t)+e^{i\omega_{2k}\Delta t}u^{+}(t-\Delta t)\right]+e^{i\omega_{2k}\Delta t}I_{2k}(t-\Delta t) \qquad (A24)$$

$$\mu_{2k-1}=\frac{\omega_{2k-1}A_{2k-1}-iA_{2k}}{2\beta_k}=\frac{\beta_k A_{2k-1}+i(\alpha_k A_{2k-1}-A_{2k})}{2\beta_k} \qquad (A25)$$

$$\mu_{2k-1}=\frac{\omega_{2k}A_{2k-1}-iA_{2k}}{2\beta_k}=\frac{-\beta_k A_{2k-1}+i(\alpha_k A_{2k-1}-A_{2k})}{2\beta_k} \qquad (A26)$$

B. Extended Helmholtz Resonator Model (EHR) and Frequency Response Function (FRF) Impedance Boundary Condition

Rienstra [38] proposed a model, based on a Helmholtz-resonator and the z transform, which satisfies all conditions and can be exactly tuned to the impedance at a design frequency using five parameters. The implementation of the Extended Helmholtz Resonator Model (EHR) requires the storage of a long time history.

The EHR model of Rienstra is defined in the frequency domain by:

$$Z(i\omega) = R + i\omega m - i\beta \cot(\frac{1}{2}\omega T_1 - i\frac{1}{2}\varepsilon)$$
$$= \frac{(R + i\omega m)(1 - e^{-\alpha}) + \beta(1 + e^{-\alpha})}{1 - e^{-\alpha}} \qquad (B1)$$

where $\alpha = i\omega T_l + \varepsilon$. The five parameters in this model, R, m, ε, β and T_l have to be positive, and $Z(i\omega)$ is a real, passive and causal impedance [38]. $Z(i\omega)$ is a rational function that describes a periodic frequency response of the impedance given by the term $e^{-i\omega T_l}$.

The time-domain representation of the preceding model requires the application of a generalized δ function to obtain the inverse Fourier transform of a periodic function $e^{-i\omega T_l}$:

$$\delta(t - T_l) = \frac{1}{2\pi}\int_{-\infty}^{\infty} e^{-i\omega T_l} e^{i\omega t} d\omega \qquad (B2)$$

Applying Eq. (B2) to both sides of Eq. (B1), and using the properties of the inverse Fourier transformation, one can obtain:

$$p(t) - e^{-\varepsilon} p(t - T_l) = (R + \beta + i\omega m) v_n(t) - (R - \beta + i\omega m) e^{-\varepsilon} v_n(t - T_l) \qquad (B3)$$

The $i\omega m$ term is transformed directly to a time derivative. The implemented form of the boundary condition to the time derivative of the normal velocity is given as:

$$\frac{\partial v_n}{\partial t}(t) = \frac{1}{m}[\mu(t) - e^{-\varepsilon}\mu(t - T_l) - (R + \beta) v_n(t) + (R - \beta) e^{-\varepsilon} v_n(t - T_l)]$$
$$+ e^{-\varepsilon}\frac{\partial v_n}{\partial t}(t - T_l) \qquad (B4)$$

where $\mu(t)$ is defined as:

$$\mu(t) = p' + \mathbf{v_0} \cdot \nabla p - \mathbf{n} \cdot (\mathbf{n} \cdot \nabla v_0) p \qquad (B5)$$

EHR requires the data at previous times $t - T_l$. As the coefficients are constant, the whole expression including previous time levels can be stored in one variable. To avoid interpolation, T_l could be chosen to be a multiple of the time step of the time domain simulation [38].

Bin and Hussaini [68] proposed to represent the impedance as a linear sum of the second-order frequency response function (FRF) as follows

$$Z(\omega) = \sum_{j=1}^{N} \frac{a_0^j (i\omega) + a_1^j}{b_0^j (i\omega)^2 + b_1^j (i\omega) + b_2^j} \tag{B6}$$

where N is the number of FRFs and a^j and b^j are the constants parameters that are so determined as to yield the best approximation to the empirical data. This model requires all the parameters to be positive for the stability analysis.

Substituting Eq. (B6) into Eq. (B3) with some algebra and manipulation using inverse Fourier transforms, one can obtain:

$$\frac{\partial p}{\partial t} + \mathbf{u_0} \cdot \nabla p = \sum_{j}^{N} \frac{\partial p_j}{\partial t} \tag{B7}$$

where

$$\hat{p}_j(\omega) = -\hat{v}(\omega) \frac{a_0^j (i\omega) + a_1^j}{b_0^j (i\omega)^2 + b_1^j (i\omega) + b_2^j}, \qquad j = 1,2,\dots,N \tag{B8}$$

$\hat{p}_j$and $\hat{v}$ are the complex amplitudes of pressure perturbation and velocity perturbation respectively. After applying the inverse transform to Eq. (B8), the $\hat{p}_j(\omega)$ could be rearranged as:

$$\left(b_0^j \frac{\partial^2 p_j}{\partial t^2} + b_1^j \frac{\partial p_j}{\partial t} + b_2^j \right) = -\left(a_0^j \frac{\partial v}{\partial t} + a_1^j v \right) \tag{B9}$$

where v is the normal velocity perturbation on the wall, and p_j is the pressure of jth subcomponent in Eq. (B7).

C. Analytical Solution to Scattering Benchmark Case

According to reference [59], the boundary conditions around the cylinder are:

$$\mathbf{v} \cdot \mathbf{n} = 0 \; at \; x^2 + y^2 = (0.5)^2 \tag{C1}$$

and when $x, y \to \infty$ the solution represents outgoing waves. One can find the solution in terms of velocity potential $\phi(x, y, t)$ given as:

$$u = \frac{\partial \phi}{\partial x}, v = \frac{\partial \phi}{\partial y}, p = -\frac{\partial \phi}{\partial t}. \tag{C2}$$

Using polar coordinates (r, θ), the wave equation could be written as:

$$\frac{\partial^2 \phi}{\partial t^2} - \left(\frac{\partial^2 \phi}{\partial r^2} + \frac{1}{r}\frac{\partial \phi}{\partial r} + \frac{1}{r^2}\frac{\partial^2 \phi}{\partial \theta^2} \right) = 0. \tag{C3}$$

The initial condition of C1 becomes:

$$t = 0: \qquad \phi = 0, \qquad \frac{\partial \phi}{\partial t} = -e^{-b\left(r^2 + x_s^2 - 2r x_s \cos\theta\right)} \tag{C4}$$

where $x_s = 4, b = \frac{ln2}{w^2}, w = 0.2$.

The boundary condition of C1 becomes:

$$\frac{\partial \phi}{\partial r} = 0 \; at \; r = 0.5. \tag{C5}$$

The problem (C3)-(C5) could be solved by the method of superposition.

$$\phi(r, \theta, t) = \phi_i(r, \theta, t) + \phi_r(r, \theta, t) \tag{C6}$$

where ϕ_i is the incident wave generated by the initial pressure pulse, and ϕ_r is the wave reflected off the cylinder. $\phi_i(r, \theta, t)$ satisfies the equation:

$$\frac{\partial^2 \phi_i}{\partial t^2} - \left(\frac{\partial^2 \phi_i}{\partial {r_s}^2} + \frac{1}{r}\frac{\partial \phi_i}{\partial r_s} \right) = 0 \tag{C7}$$

with the initial conditions,

$$t = 0: \qquad \phi_i = 0, \qquad \frac{\partial \phi_i}{\partial t} = -e^{-b{r_s}^2} \tag{C8}$$

where (r_s, θ_s) are the polar coordinates with the origin at $x = x_s, y = 0$.

The initial solution to ϕ_i could be solved by the order-zero Hankel transform [60]:

$$\phi_i(r_s, t) = -\frac{1}{2b}\int_0^\infty e^{-\frac{w^2}{4b}} J_0(\omega r_s) \sin(\omega t)\, d\omega \tag{C9}$$

or in terms of (r, θ) coordinates,

$$\phi_i(r, \theta, t) = \int_0^\infty A_i\,(r, \theta, \omega) \sin(\omega t)\, d\omega \tag{C10}$$

where

$$A_i(r,\theta,\omega) = -\frac{1}{2b} e^{-\frac{w^2}{4b}} J_0\left(\omega\sqrt{r^2 + x_s^2 - 2rx_s\cos\theta}\right). \quad \text{(C11)}$$

The problem for ϕ_r is:

$$\frac{\partial^2\phi_r}{\partial t^2} - \left(\frac{\partial^2\phi_r}{\partial r^2} + \frac{1}{r}\frac{\partial\phi_r}{\partial r} + \frac{1}{r^2}\frac{\partial^2\phi_r}{\partial\theta^2}\right) = 0 \quad (C12)$$

$$\frac{\partial\phi_r}{\partial r} = -\frac{\partial\phi_i}{\partial r} \; at \; r = 0.5. \quad (C13)$$

Assuming

$$\phi_r(r,\theta,\omega) = \int_0^\infty A_r(r,\theta,\omega)\sin(\omega t)\, d\omega, \quad \text{(C14)}$$

we could use a Fourier sine transformation. Substituting Eq. (C14) into Eq. (C12) and Eq. (C13), we then obtain:

$$\frac{\partial^2 A_r}{\partial r^2} + \frac{1}{r}\frac{\partial A_r}{\partial r} + \frac{1}{r^2}\frac{\partial^2 A_r}{\partial\theta^2} + \omega^2 A_r = 0 \quad (C15)$$

$$\frac{\partial A_r}{\partial r} = B(\theta,\omega) \; at \; r = 0.5 \quad (C16)$$

where $B(\theta,\omega) = -\frac{\partial A_i}{\partial r}\Big|_{r=0.5}$.

Eq. (C15) can be solved using a summation of the Hankel function and the Fourier function

$$A_r(r,\theta,\omega) = \sum_{k=0}^{\infty} C_k(\omega) H_k^{(1)}(r\omega)\cos(k\theta). \quad \text{(C17)}$$

The coefficients C_k of Eq. (C17) are given by using boundary condition (C16), where

$$C_k = \frac{\epsilon_k}{\pi\left[\frac{2k}{\omega}H_k^{(1)}\left(\frac{\omega}{2}\right) - H_{k+1}^{(1)}\left(\frac{\omega}{2}\right)\right]}\int_0^\pi B(\theta,\omega)\cos(k\theta)\, d\theta \quad \text{(C18)}$$

where

$$A(r,\theta,\omega) = -\frac{e^{-\frac{\omega^2}{4b}}}{2b}\left\{J_0\left(\omega\sqrt{r^2 + x_s^2 - 2rx_s\cos\theta}\right) + \sum_{k=0}^{\infty} Re\left[\frac{2\epsilon_k H_k^{(1)}(r\omega)\cos(k\theta)}{\pi\left[\frac{2k}{\omega}H_k^{(1)}\left(\frac{\omega}{2}\right) - H_{k+1}^{(1)}\left(\frac{\omega}{2}\right)\right]}\right]\right.$$

$$\left.\cdot\int_0^\pi \frac{(0.5 - x_s\cos\eta)J_1\left(\omega\sqrt{0.25 + x_s^2 - x_s\cos\eta}\right)}{\sqrt{0.25 + x_s^2 - x_s\cos\eta}}\cos(k\eta)\, d\eta\right\} \quad \text{(C19)}$$

The pressure field may be calculated by

$$p(r,\theta,t) = -\frac{\partial \phi}{\partial t} = -\int_0^\infty A(r,\theta,\omega)\omega \cos(\omega t)\, d\omega. \tag{C20}$$